OPTICAL METASURFACES FOR POLARIZATION GENERATION, DETECTION AND IMAGING

Yuttana Intaravanne

Submitted for the degree of Doctor of Philosophy

Heriot-Watt University

School of Engineering and Physical Sciences

June 2022

ABSTRACT

Like phase and amplitude, polarization is a fundamental property of light, which can reveal hidden information and has been used in many research fields, including material science, medicine, target detection and biomedical diagnosis. Polarization generation, detection and imaging are of importance for fundamental research and practical applications. Although conventional optics can perform these tasks, it suffers from a complex system, large volume and high cost, which cannot meet the continuing trend of miniaturization and integration. Optical metasurfaces, the two-dimensional counterparts of metamaterials, are planar nanostructured interfaces, which have recently attracted tremendous interest in realizing ultrathin and lightweight planar optical devices. Optical metasurfaces can manipulate light's amplitude, phase and polarization in a desirable manner, providing a new and compact platform to generate, detect and manipulate light's polarization. This thesis utilises optical metasurfaces to realise and experimentally demonstrate novel optical devices for polarization generation, detection and imaging. Due to the simplicity of the design and fabrication, this thesis is mainly focused on geometric optical metasurfaces, which are superior to other types of metasurfaces.

2D and 3D polarization structures are generated based on a metalens approach. A ring focal curve, an Archimedean spiral focal curve, and seven-segment-based decimal numbers are experimentally demonstrated in 2D space, while a 3-foil knot, a 4-foil knot, and a 5-foil are realized in 3D space. The geometric metasurfaces are designed based on colour and phase multiplexing and polarization rotation, creating various 3D polarization knots. Various 3D polarization knots in the same observation region can be achieved by controlling the incident wavelengths, providing unprecedented polarization control with colour information in 3D space. Novel polarization detection is experimentally demonstrated through optical holography, light's orbital angular momentum, and optical ring vortex beams. The measured polarization parameters such as major axis, ellipticity, and handedness are in good agreement with the theoretical prediction. A multifunctional microscope is proposed and developed to image different objects, including biological samples such as cheek cells and beef tendons. For the same sample, five images with different optical properties are obtained on the same imaging plane, which can simultaneously perform edge imaging, polarimetric imaging, and conventional microscope imaging. Benefiting from the ultrathin nature, compactness and multifunctionality of the optical metasurface devices, the integration does not excessively

increase the volume of the optical system. With its promising capabilities and potential for expandability, we believe our microscope will herald an exciting new era in biomedical research.

The ultrathin nature of optical metasurfaces and their unprecedented capability in light control have provided a compact platform to develop ultrathin optical devices with novel functionalities that are very difficult or impossible to achieve with conventional optics. The metasurface platform for polarization detection and manipulation is very attractive for diverse applications, including polarization sensing and imaging, optical communications, optical tweezers, quantum sciences, display technologies, and biomedical research as well as wearable and portable consumer electronics and optics where miniaturized systems are in high demand.

DEDICATION

To my beloved family

ACKNOWLEDGEMENTS

Throughout an extremely difficult task of my academic years to pursue a PhD degree, it would not be possible to achieve without the gracious advice and support from a lot of people.

Firstly, I would like to honourably thank my special supervisor, Dr Xianzhong Chen, who has handled many things for me on both academic and living issues. My knowledge in metasurfaces has started from zero, but it has been gradually improved under his supervision until I could make big contributions to our high-impact journal papers. I am also grateful to my second supervisor, Professor Alessandro Fedrizzi, for his support throughout the academic years. I would also like to thank my former supervisors, Professor Ajoy Kar and Dr Bruce Sinclair, who welcomed me to the world of optics and photonics when I was a master's student as well as opened the door for me to meet Dr Chen.

I really appreciate Mr Neil Ross and Dr Hyeonjun Baek for their training on nanofabrication facilities in the clean room. Many thanks to Dr Dandan Wen, Dr Fuyong Yue, and Dr Chunmei Zhang, who provided me with valuable resources from their works that make me work easily in this area. I also would like to thank Dr Jin Han, Dr Aning Ma, Dr Ruoxing Wang, Dr Songtao Li, Dr Yang Ming, Dr Muhammad Afnan Ansari, Mr Hammad Ahmed, and my collaborators in China.

I am grateful to my advisor in Thailand, Dr Sarun Sumriddetchkajorn, who gave me an opportunity to study oversea and provided me a lot of academic training that I can directly apply to my PhD research. I also would like to thank the Royal Thai Government Scholarship programme that fully supports me for studying and living in the UK.

Last but not least, I have deeply indebted to my cosy family members who are always beside me and always strongly encourage me to follow my dreams. I also gratefully acknowledge my teachers who educated me when I was young and my lovely friends for their support along my way.

Research Thesis Submission

Please note this form should be bound into the submitted thesis.

Name:	**YUTTANA INTARAVANNE**		
School:	**SCHOOL OF ENGINEERING AND PHYSICAL SCIENCES**		
Version: *(i.e. First, Resubmission, Final)*	**Final**	Degree Sought:	**PHD**

Declaration

In accordance with the appropriate regulations I hereby submit my thesis and I declare that:

1. The thesis embodies the results of my own work and has been composed by myself
2. Where appropriate, I have made acknowledgement of the work of others
3. The thesis is the correct version for submission and is the same version as any electronic versions submitted*.
4. My thesis for the award referred to, deposited in the Heriot-Watt University Library, should be made available for loan or photocopying and be available via the Institutional Repository, subject to such conditions as the Librarian may require
5. I understand that as a student of the University I am required to abide by the Regulations of the University and to conform to its discipline.
6. I confirm that the thesis has been verified against plagiarism via an approved plagiarism detection application e.g. Turnitin.

ONLY for submissions including published works

Please note you are only required to complete the Inclusion of Published Works Form (page 2) if your thesis contains published works)

7. Where the thesis contains published outputs under Regulation 6 (9.1.2) or Regulation 43 (9) these are accompanied by a critical review which accurately describes my contribution to the research and, for multi-author outputs, a signed declaration indicating the contribution of each author (complete)
8. Inclusion of published outputs under Regulation 6 (9.1.2) or Regulation 43 (9) shall not constitute plagiarism.

* *Please note that it is the responsibility of the candidate to ensure that the correct version of the thesis is submitted.*

Signature of Candidate:	Yuttana Intaravanne	Date:	25/06/2022

Submission

Submitted By *(name in capitals)*:	**YUTTANA INTARAVANNE**
Signature of Individual Submitting:	Yuttana Intaravanne
Date Submitted:	25/06/2022

For Completion in the Student Service Centre (SSC)

Limited Access	Requested	Yes		No		Approved	Yes		No	
E-thesis Submitted ***(mandatory for final theses)***										
Received in the SSC by *(name in capitals)*:						Date:				

Inclusion of Published Works

Please note you are only required to complete the Inclusion of Published Works Form if your thesis contains published works under Regulation 6 (9.1.2)

Declaration

This thesis contains one or more multi-author published works. In accordance with Regulation 6 (9.1.2) I hereby declare that the contributions of each author to these publications is as follows:

Citation details	e. g. Author 1 and Author 2, Title of paper, Title of Journal, X, XX-XX (20XX)
Author 1	Contribution….
Author 2	Contribution….
Signature:	
Date:	

Citation details	e. g. Author 1 and Author 2, Title of paper, Title of Journal, X, XX-XX (20XX)
Author 1	Contribution….
Author 2	Contribution….
Signature:	
Date:	

Citation details	e. g. Author 1 and Author 2, Title of paper, Title of Journal, X, XX-XX (20XX)
Author 1	Contribution….
Author 2	Contribution….
Signature:	
Date:	

Please included additional citations as required.

TABLE OF CONTENTS

LIST OF FIGURES

LIST OF ABBREVIATIONS

1D…..……One-Dimensional

2D……Two Dimensional

3D……. Three-Dimensional

CCD…….. Charge-Coupled Device

CP……...…….Circularly Polarized

CST……Computer Simulation Technology

EBL……Electron-Beam Lithography

FW…… Fundamental Wave

HW…… Harmonic Wave

HWP……..Half-Wave Plate

IPA……..Isopropanol Alcohol

ITO……..Indium Tin Oxide

LCP……..Left-Circularly Polarized

LEP…… Left-Elliptically Polarized

LP……...Linearly Polarized

OAM……...Orbital Angular Momentum

ORV…….Optical Ring Vortex

PMMA…….Polymethyl Methacrylate

QWP……Quarter-Wave Plate

RCP……... Right-Circularly Polarized

REP...…...…… Right-Elliptically Polarized

SAM……Spin Angular Momentum

SEM……Scanning Electron Microscope

SiO_2…… Silicon Dioxide

TC…… Topological Charge

TiO_2…… Titanium Dioxide

LIST OF PUBLICATIONS

Journal Articles

1. **Y. Intaravanne**, J. Han, R. Wang, A. Ma, S. Li, S. Chen, and X. Chen, "Phase manipulation-based polarization profile realization and hybrid holograms using geometric metasurface," *Adv. Photonics Res. 2*, 2000046 (2021).
2. **Y. Intaravanne**, and X. Chen, "Recent advances in optical metasurfaces for polarization detection and engineered polarization profiles," *Nanophotonics 9*, 1003 (2020).
3. **Y. Intaravanne**, R. Wang, H. Ahmed, Y. Ming, Y. Zheng, Z. K. Zhou, Z. Li, S. Chen, S. Zhang, and X. Chen, "Color selective three-dimensional polarization structures," *Light Sci. Appl.* (Revised version submitted).
4. **Y. Intaravanne**, and X. Chen, "Metasurface enabled multifunctional microscopy," In preparation.
5. **Y. Intaravanne**, and X. Chen, "Learning-assisted wavelength-selective digital numbers with metasurfaces," In preparation.
6. H. Ahmed[†], **Y. Intaravanne**[†], Y. Ming, M. A. Ansari, G. Buller, T. Zentgraf, and X. Chen, "Multichannel superposition of grafted perfect vortex beams," *Adv. Mater. 2022 (Accepted).*
7. Y. Ming[†], **Y. Intaravanne**[†], Hammad Ahmed, Mitchell Kenny, Yan-qing Lu, and Xianzhong Chen, "Creating composite vortex beams with a single geometric metasurface," *Adv. Mater. 34*, 2109714 (2022).
8. R. Wang[†], **Y. Intaravanne**[†], S. Li, J. Han, S. Chen, J. Liu, S. Zhang, L. Li, and X. Chen, "Metalens for generating a customized vectorial focal curve," *Nano Lett. 21*, 2081 (2021).
9. J. Han[†], **Y. Intaravanne**[†], A. Ma, R. Wang, S. Li, Z. Li, S. Chen, J. Li, and X. Chen, "Optical metasurfaces for generation and superposition of optical ring vortex beams," *Laser Photonics Rev. 14***,** 2000146 (2020).
10. A. Ma[†], **Y. Intaravanne**[†], J. Han, R. Wang, and X. Chen, "Polarization detection using light's orbital angular momentum**,"** *Adv. Opt. Mater. 8***,** 2000484 (2020).
11. Y. Tang[†], **Y. Intaravanne**[†], J. Deng, K. F. Li, X. Chen, and G. Li, "Nonlinear vectorial metasurface for optical encryption," *Phys. Rev. Appl. 12*, 024028 (2019).

[†]*These authors contributed equally to this work.*

12. H. Ahmed, H. Kim, Y. Zhang, **Y. Intaravanne**, J. Jang, J. Rho, S. Chen, and X. Chen, "Optical metasurfaces for generating and manipulating optical vortex beams," *Nanophotonics 11*, 941 (2022).
13. X. Zang, H. Ding, **Y. Intaravanne**, L. Chen, Y. Peng, J. Xie, Q. Ke, A. V. Balakin, A. P. Shkurinov, X. Chen, Y. Zhu, and S. Zhuang, "Multi-foci metalens with polarization-rotated focal points," *Laser Photonics Rev. 13*, 1900182 (2019).
14. X. Zang, H. Ding, **Y. Intaravanne**, L. Chen, Y. Peng, J. Xie, Q. Ke, A. V. Balakin, A. P. Shkurinov, X. Chen, Y. Zhu, and S. Zhuang, "Multi-foci metalenses: a multi-foci metalens with polarization-rotated focal points," *Laser Photonics Rev. 13*, 1970051 (2019).
15. C. Zhang, F. Dong, **Y. Intaravanne**, X. Zang, L. Xu, Z. Song, G. Zheng, W. Wang, W. Chu, and X. Chen, "Multichannel metasurfaces for anticounterfeiting," *Phys. Rev. Appl. 12*, 034028 (2019).
16. S. Hermon, A. Ma, F. Yue, F. Kubrom, **Y. Intaravanne**, J. Han, Y. Ma, and X. Chen, "Metasurface hologram for polarization measurement," *Opt. Lett. 44*, 4436 (2019).
17. C. Zhang, D. Wen, F. Yue, **Y. Intaravanne**, W. Wang, and X. Chen, "Optical metasurface generated vector beam for anticounterfeiting," *Phys. Rev. Appl. 10*, 034028 (2018).

Conference Presentations

1. X. Chen, **Y. Intaravanne**, Optical metasurfaces for generating customized polarization profiles, MRS Fall Meeting, USA (2021).
2. **Y. Intaravanne**, and X. Chen, Simultaneous Generation of Image Concealment and Hybrid Hologram with Geometric Metasurfaces, PIERS, Hangzhou, China (2021).
3. X. Chen, and **Y. Intaravanne**, Optical metasurfaces for polarization detection and generation, PIERS, Hangzhou, China (2021).
4. **Y. Intaravanne**, Utilization of geometric metasurfaces for developing ultra-thin optical devices with unusual functionalities, SACC 2021, Mathematics and Physical Science, UK (2021).
5. X. Chen, and **Y. Intaravanne**, Optical metasurface for engineered polarization profile, META 2020, Warsaw, Poland (2020).
6. X. Chen, and **Y. Intaravanne**, Optical metasurface for customized polarization control, The 6th International Conference on Frontiers of nano-Photonics, Kunming, China (2020).

7. **Y. Intaravanne**, and X. Chen, "Dielectric metasurfaces for ultrathin half waveplates," *Proc. META 2019*, Lisbon, Portugal (2019).
8. X. Chen, C. Zhang, and **Y. Intaravanne**, "Metasurface based arbitrary polarization control and its applications," *Proc. META 2019*, Lisbon, Portugal (2019).
9. C. Zhang, **Y. Intaravanne**, W. Wang, and X. Chen, "Hiding a QR code in a vector light beam," *Proc. META 2019*, Lisbon, Portugal (2019).

CHAPTER 1 – INTRODUCTION

Although traditional optical elements can manipulate the properties of light such as amplitude, phase, and polarization, they cannot meet the requirement of device miniaturization and system integration due to the bulky size. Thus, there is an urgent need for ultrathin and flat optical elements. Metamaterials are artificial media, whose properties are determined by their geometric structures instead of constituent components [1]. Optical metamaterials have opened new avenues in the field of optics by introducing unprecedented optical phenomena such as optical cloaks [2], thermal-IR resonators [3], negative refractive index elements for terahertz frequencies [4], low loss microwave lenses [5], and wireless strain sensors [6]. However, metamaterials operating at much shorter wavelengths especially in the visible range are still far from reaching their full potential, chiefly because of the limitation in 3D fabrication at nanometre resolution. Optical metasurfaces, the emerging field of 2D metamaterials, have captured the attention of the scientific community over the last ten years. The optical metasurfaces do not require complicated three-dimensional nano-fabrication techniques but can control light propagation in equally dramatic ways. In comparison with spatial light modulators whose functionalities can be dynamically changed by either microelectromechanical [7] or liquid crystal (LC) technology [8], optical metasurfaces are ultrathin and ultraflat, and have sub-wavelength pixel sizes. Benefiting from the unique properties, optical metasurface devices can perform the extremely challenging optical tasks that are impossible with commercial spatial light modulators. Furthermore, the optical metasurfaces can also be integrated with LCs in order to tune their functionalities, which can function as tuneable spatial light modulators, but the dimension is dramatically decreased [9]. In this chapter, the current progress of optical metasurfaces and their applications will be reviewed.

1.1. Optical Metasurfaces

Since the advent of the generalised law of reflection and refraction in 2011, the directions of reflected and refracted beams can now be controlled at the interface between two optical media in a desirable manner [10]. The desired control can be realized by introducing a digitised phase shift at the interface ($d\Phi/dx$) as explained in Equation 1.1.

$$n_t \sin\theta_t - n_i \sin\theta_i = \frac{\lambda_0}{2\pi}\frac{d\Phi}{dx} \tag{1.1}$$

where n_t and n_i are the refractive indices of the two media. θ_i and θ_t are the incident and transmitted angles of a light beam at a wavelength of λ_0, respectively. With a phase gradient shown in Figure 1.1, the anomalous reflection and refraction can be generated, and their θ_t can be arbitrarily designed. These phenomena are unusual and difficult to obtain with conventional optical devices. An optical metasurface can produce a digitised phase profile generated with an abrupt phase change which can control the wavefront of light during its propagation. In the last several years, various types of optical metasurfaces have been proposed and experimentally demonstrated for developing novel devices with unusual functionalities.

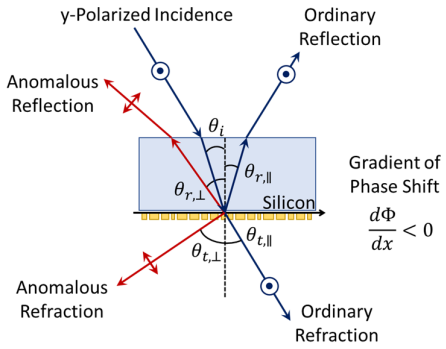

Figure 1.1 Anomalous reflection and refraction with phase discontinuity at the interface between two media proposed by Yu et al in 2011 [10].

1.2. Various Types of Metasurfaces

The evolution of optical metasurfaces with a sub-wavelength resolution is shown in Figure 1.2. The first version of metasurfaces consists of plasmonic resonators with V-shaped gold nanostructures, which have been introduced to generate an abrupt phase shift at the interface between two optical media [10]. Upon the illumination of incident linearly polarized (LP) light at a specific wavelength, the phase shifts can be tuned from 0 to 2π by using an appropriate orientation and opening angle between two arms as shown in Figure 1.2a. The V-shape nanostructure is a wavelength-dependent phase shifter. Hence, a dipole gold nanostructure has been proposed to perform a broadband operation under the illumination of circularly polarized (CP) light [11]. In this design, all nanostructures are identical, but spatially varying orientation angles to provide the abrupt phase shift ranging from 0 to 2π as shown in Figure 1.2b. The phase shift is twice the orientation angle and can be + or – depending on the helicity of the CP light. This additional phase shift is known as a Pancharatnam–Berry (PB) phase, which is also called a geometric metasurface (the details are discussed in Chapter 2). Since a metallic material like gold is

a lossy material in the visible domain, only a small fraction of the CP light can be converted into the PB phase. In the subsequent investigations, the conversion efficiency has increased up to 80% by using a multilayer design, including a dielectric spacer sandwiched between a gold ground film and a gold nanostructure [12]. The multilayer design is also based on a PB phase shifter as shown in Figure 1.2c. This design is suitable for developing reflective optical devices, whereas a high efficiency for transmissive operation is still needed. A silicon-based nanopillar has been proposed to realise an efficient phase shifter for transmissive devices upon the illumination of LP light [13]. This metasurface utilises dielectric nanopillars with different dimensions to provide a propagation phase upon the illumination of LP light as shown in Figure 1.2d. Afterward, a TiO_2 nanopillar has been reported to generate a PB phase shift (Figure 1.2e). The dimension of the nanopillars has been optimised to operate as a half-waveplate for maximum conversion efficiency [14]. Geometric metasurfaces can provide multichannel functionality depending on the helicity of incident CP light (left-circularly polarized (LCP) or right-circularly polarized (RCP)). However, the generated phase shifts for both LCP and RCP light are relative to each other. To independently obtain a phase shift from LCP and RCP, the combination of the propagation phase and the PB phase has been proposed [15]. The nanopillars used in this design are comprised of spatially varying orientation angles and dimensions as shown in Figure 1.2f. In the last few years, many novel optical devices and their attractive applications have been proposed and experimentally demonstrated by utilising the aforementioned optical metasurfaces.

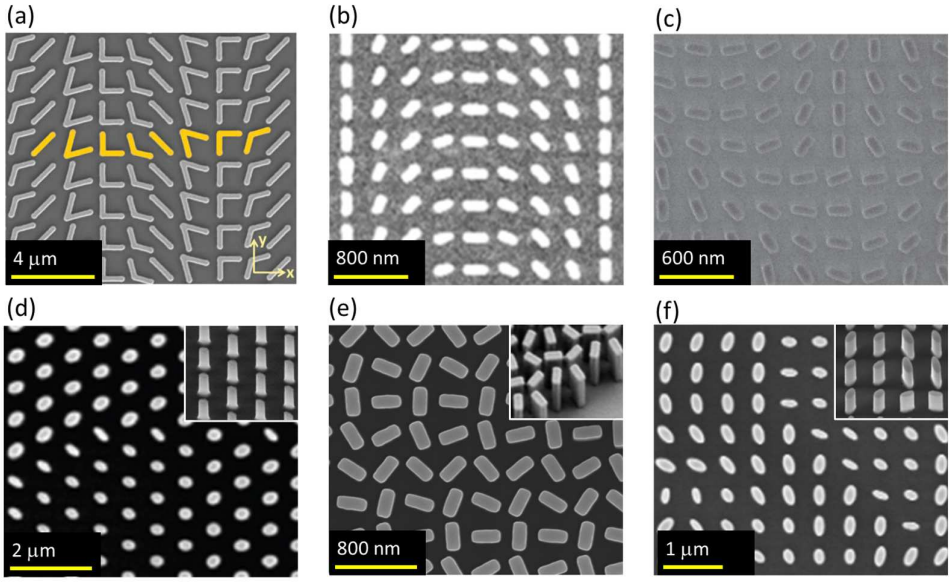

Figure 1.2 Evolution of optical metasurfaces. (a) Plasmonic resonators with V-shape nanostructures [10]. (b) A geometric metasurface with gold nanorods [11]. (c) A multilayer geometric metasurface with gold

nanorods [12]. (d) A propagation phase-based metasurface with silicon nanoposts [13]. (e) A geometric metasurface with TiO_2 nanopillars functioning as half-waveplates [14]. (f) A combination of a propagation phase and a geometric phase with TiO_2 nanopillars [15].

1.3. Applications of Metasurfaces

1.3.1. Phase Gradient and Beam Steering

A phase gradient metasurface is a simple design for steering a light beam by utilizing the generalised law of reflection and refraction as shown in Equation 1.1. The incident light can be steered in an arbitrary direction by imparting the constant value of $d\Phi/dx$. More than bending the light beam, the benefit from the phase gradient based on the PB phase is polarization detection. As the PB phase provides the same phase shift for both CP lights but with different signs, the LCP and RCP components of the incident light can be separated [16].

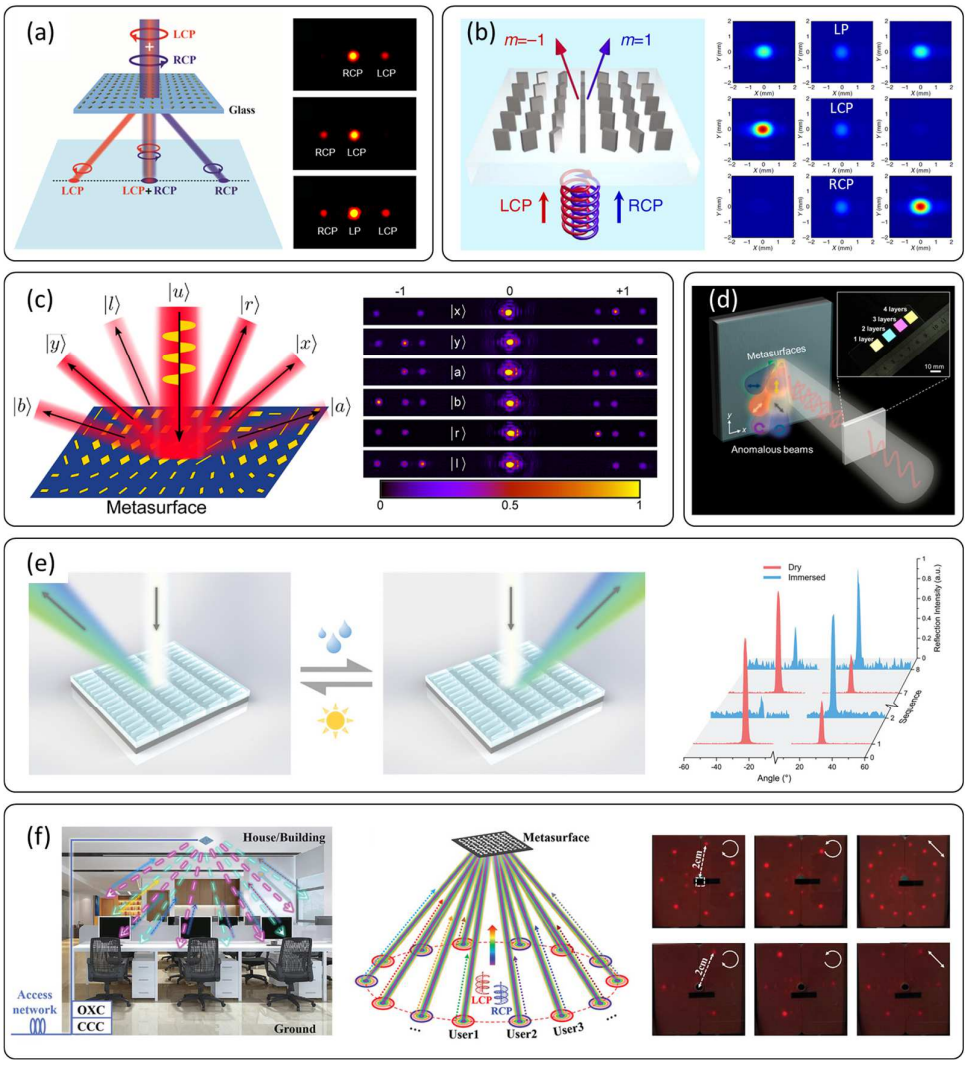

Figure 1.3 Beam steering metasurfaces and their applications. (a) A plasmonic [16] and (b) dielectric-based [17] phase gradient metasurfaces for detection of circularly polarized light. (c)-(d) Integrated metasurfaces for on-chip polarimetry [18, 19]. (e) A phase gradient metasurface for weather sensing [20]. (f) Phase gradient metasurfaces for wireless communication [21].

For a plasmonic metasurface, the conversion efficiency is relatively low. Thus, the non-converted part in the middle is strong compared to the converted part as shown in Figure 1.3a. With a dielectric metasurface, it is shown that the converted part is higher as illustrated in Figure 1.3b [17]. The early demonstrations of phase gradient metasurfaces can only detect CP light. Therefore, three metasurfaces constituting the metagratings have been used for the infrared region to completely characterise the polarization state of light [18]. The metagratings consist of three types of beam-steering metasurfaces for steering LCP and RCP, LP light beams along the vertical and horizontal directions, and LP along 45° and -45° as shown in Figure 1.3c. The metasurfaces working in the visible region have also been demonstrated as shown in Figure 1.3d [19]. Those metasurfaces can be

used to perform full polarization measurement, which tell the information of polarization states of light, i.e., orientation angle of the major axis, ellipticity, and handedness. In Figure 1.3e, the nanostructures have been designed to switch the steered direction when the device is immersed in water [20]. This idea has been used to detect dry and wet weather with a repeatable routine. Similarly, a large scale of phase gradient metasurfaces has been introduced for an optical wireless broadcast as shown in Figure 1.3f [21]. Approximately 14 broadcasting channels have been experimentally demonstrated with up to 100 and 10 Gbps for upstream and downstream, respectively.

1.3.2. Metalenses

Unlike traditional lenses, optical metasurface-based lenses or metalenses provide abrupt phase shifts using an array of nanostructures rather than a curved-surface medium. In 2012, the metalens has been demonstrated with an array of V-shape nanoantennae for operation in a telecom domain as shown in Figure 1.4a [22]. A PB phase-based metalens was also proposed in the same year. Beyond its usual functionality, the PB phase-based metalens provides dual-polarity, which can disperse or focus a light beam [23]. The focusing mode can be obtained by using RCP as the incident beam, creating a focusing line on a real focal plane. On the other hand, the focusing line can be seen on a virtual focal plane if the incident light is LCP as illustrated in Figure 1.4b.

General metalenses provide an aberration-free property for monochromatic light, however, they demonstrate high dispersion for broadband wavelength, leading to chromatic aberration. Therefore, an achromatic metalens has attracted considerable attention from the research community. Based on the optimization between required and implemented phase change, a metalens with chromatic dispersionless operation over 60-nm bandwidth has been achieved [24]. The additional phase shift has been carefully designed for the compensation of the chromatic aberration covering the desired bandwidth to achieve a broadband achromatic metalens. This compensated phase shift is independent of the geometric phase. This provides an extra degree of freedom to control a phase profile for the development of achromatic metalenses over the near-infrared region (Figure 1.4c) [25], visible region (Figure 1.4d) [26], and visible region with group delay nearly to be zero (Figure 1.4e) [27].

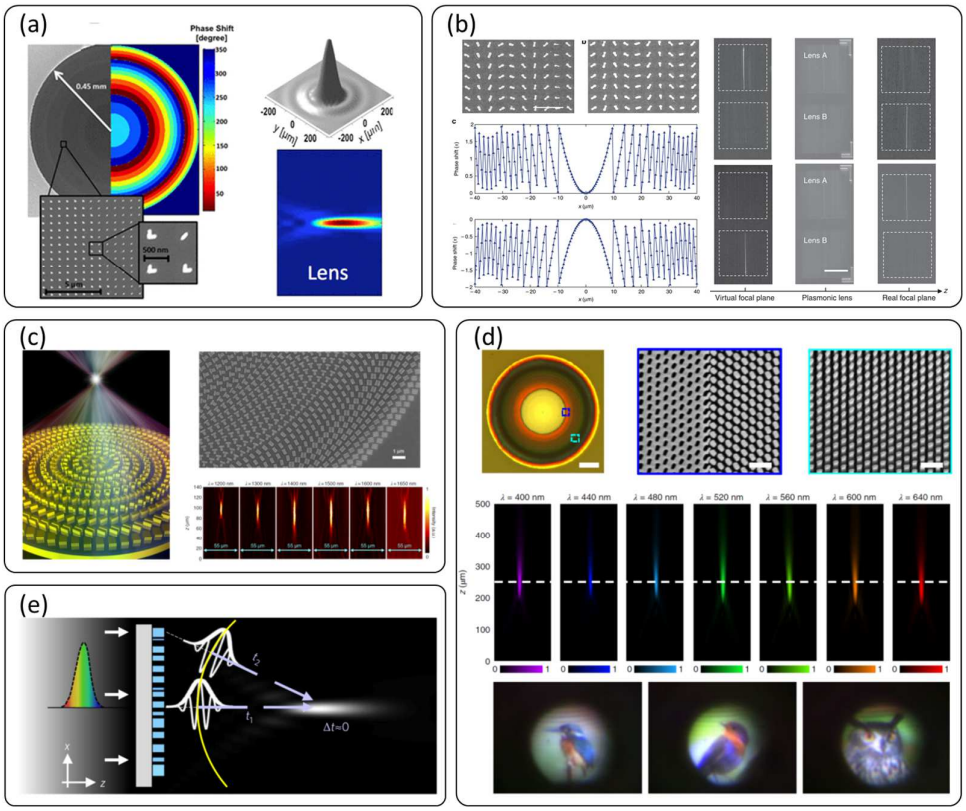

Figure 1.4 (a) Aberration-free ultrathin metalens [22]. (b) Dual polarity metalens [23]. Broadband achromatic metalenses for (c) infrared [25], (d) visible [26], and (e) visible with group delay nearly to be zero [27].

The unique properties of metalenses, including ultra-thin elements, high dispersion, and polarization-sensitive devices have played an important role in many crucial optical systems. A dual focusing metalens with different helicity of CP light has been used for multispectral chiral imaging (Figure 1.5a) [28]. High dispersion of metalens has been designed to focus at an off-axis point for an ultra-compact spectrometer (Figure 1.5b) [29, 30]. A polarization-sensitive lens has been used for polarimetry to detect full polarization states of light (Figure 1.5c) [31, 32]. An ultra-thin platform of metalens has allowed us to develop a near-eye display for augmented reality (Figure 1.5d) [33, 34]. A metalens with high dispersion has been integrated into an optical endoscope for optical coherence tomography, where the focusing points have been controlled by scanning the operation wavelength (Figure 1.5e) [35]. Inspired by a jumping spider, two different focal lengths have been integrated into a single lens to form two different images on a detection plane for depth sensing with the measured distance in a range of 10 cm (Figure 1.5f) [36].

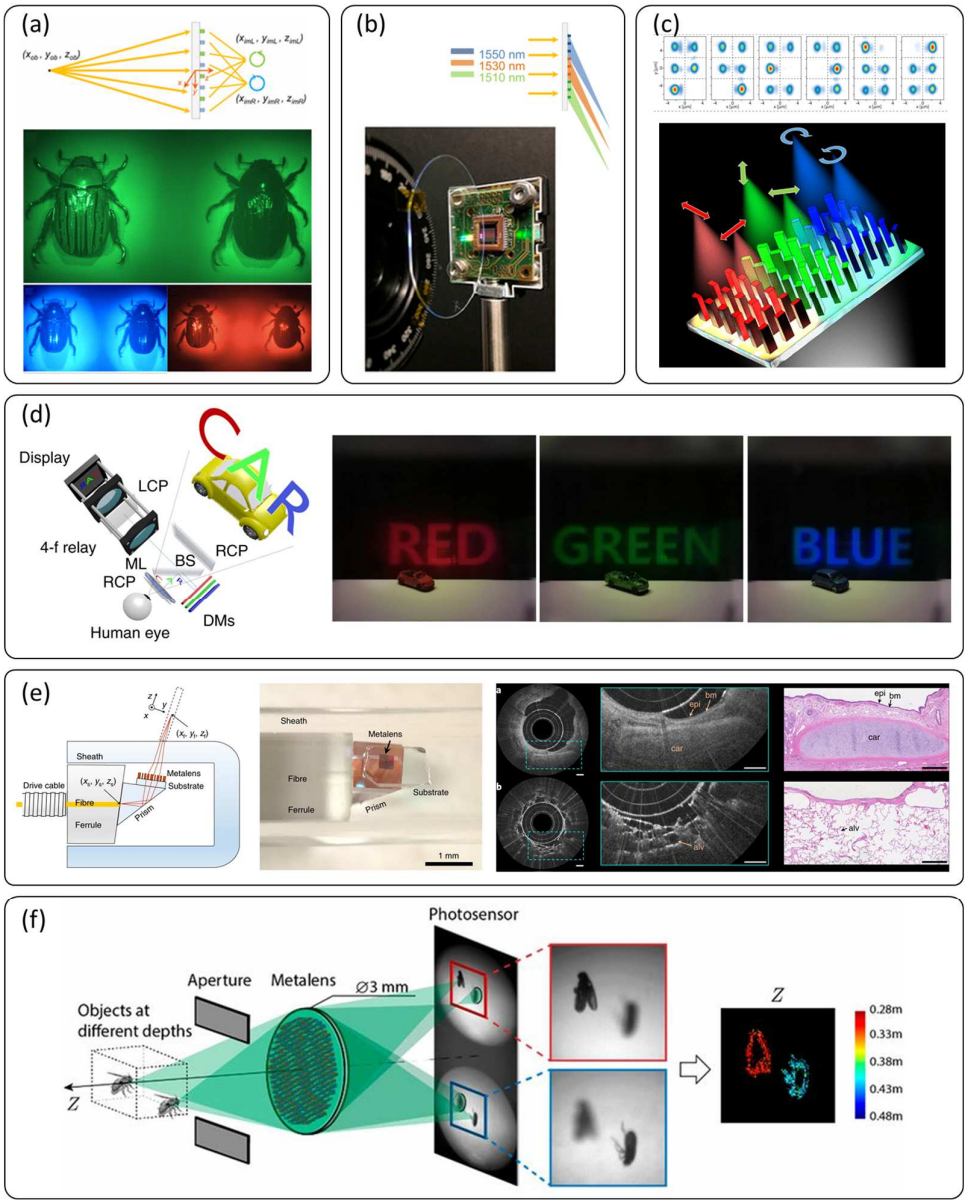

Figure 1.5 Applications of metalenses. (a) Multispectral imaging [28]. (b) An ultra-compact spectrometer [29, 30]. (c) Optical polarimetry [32]. (d) a near-eye display for augmented reality [33]. (e) an optical endoscope for optical coherence tomography [35]. (f) A depth sensor [36].

1.3.3. Holograms

A classical hologram is a recoded pattern that includes a spatially varying phase and amplitude of an object using interference between the object and reference beams. The next generation of the hologram uses the computer generation approach to calculate the phase distribution of an interesting object and transform it into controllable spatial light modulators for the generation of dynamic holograms. However, the bulky size and low resolution of pixel number have been considered. Therefore, optical metasurface-based holography has been breaking through these limitations [37]. After the generation of

phase distributions by numerical calculation, a choice of phase generator has been selected, e.g., a propagation phase [13], a geometric phase [38], or a combined phase [15]. Many reports show that all phase generators can be potentially used to generate a holographic image. Figure 1.6a, the three-dimensional holographic image has been reconstructed by geometric phase-based metasurface under the incident CP light [38]. Similarly, Figure 1.6b illustrates a unique functionality of a PB phase-based metahologram. In this design, the reconstructed images for these two polarizations can be switchable by changing the helicity of incident CP light [39]. With a propagation phase (Figure 1.6c), the holographic images can be independently obtained with two orthogonal linear polarizations [13].

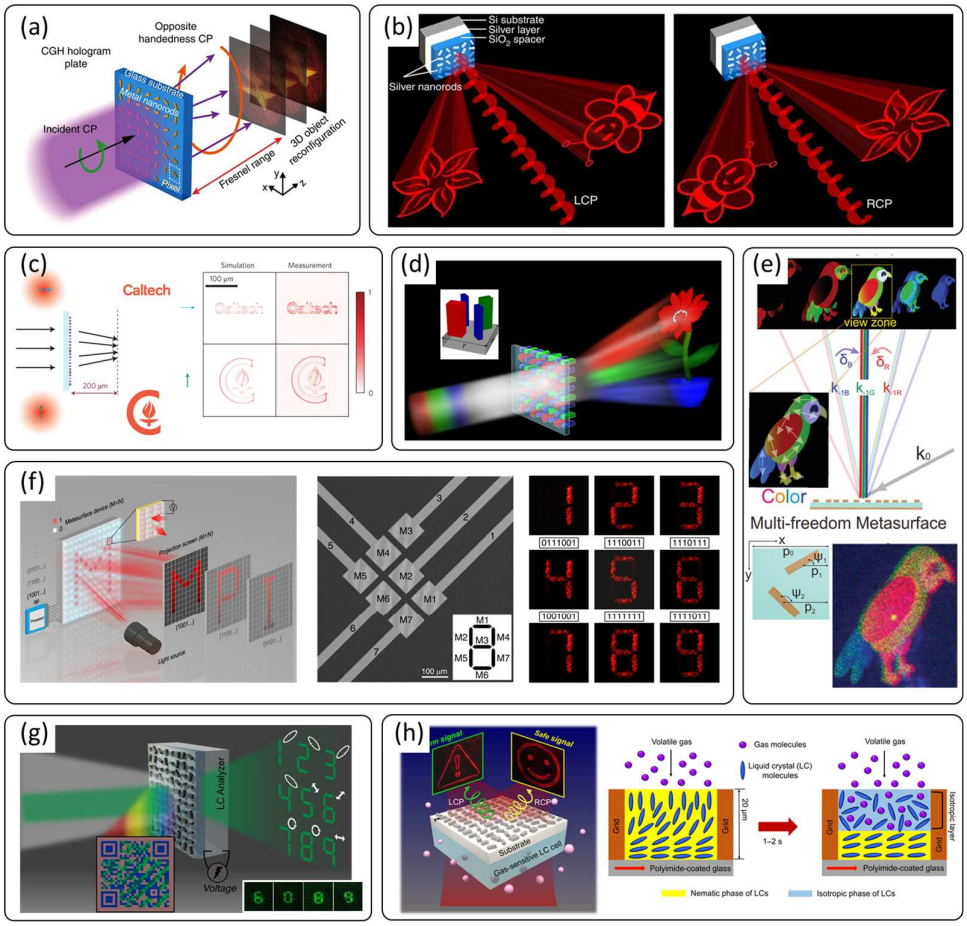

Figure 1.6 Metaholograms and their applications. (a) An optical 3D holography [38]. (b) A helicity dependent hologram [39]. (c) A polarization-switchable hologram [13]. (d) A colourful hologram [40]. (e) A colourful vectorial hologram [41]. (f) A controllable digital hologram [42]. (g) A hologram for security platform [43]. (h) A hologram for gas sensing [44].

A hologram is considered a better candidate for display-related technology due to the appearance of holographic images which can be seen easily by the naked eye. To design

a spectacular holographic image, a generation of a full-colour hologram has become a research interest. One approach is the use of a geometric phase based on dielectric nanopillars as shown in Figure 1.6d. Three sets of nanopillars have been designed to be a wavelength-selective pixel to respond to the incident CP light for only three common wavelengths, i.e., red (R), green (G), and blue (B). Thus, the RGB holographic image can be created [40]. In Figure 1.6e, the complex amplitude produced by a pair of aluminium nanostructures has been introduced to generate a full-colour hologram. In this design, all three wavelengths associated with the designed colours have provided the same holographic images. Only in a view zone, the combination of three colours can be observed [41]. In contrast, incident and deflected angles of three colours have played a key role in the reconstructed colour images. With the aid of a liquid crystal (LC) cell, the reconstructed images can be dynamically changed by electrical signals. In Figure 1.6f, the device consists of seven metaholograms, which have been individually switched on/off to create seven-segment digital numbers on a projected plane [42]. The LC cell can also be used to sort the out-coming information from the metahologram (Figure 1.6g), promising an application for the security platform [43]. In Figure 1.6h, a gas-sensitive LC cell has been integrated with a metahologram to instantaneously show an alarm signal when the gas leak is detected [44].

Unusual functionalities of metaholograms can be obtained with a composite unit cell or a super cell (more than one nanostructure in the cell). In Figure 1.7a, the metahologram has displayed different holographic images when a surrounding medium has been changed from the air to oil. This is due to the resonance mode of two gold nanostructures that provide a different reflection efficiency for different surrounding media at a specific wavelength [45]. Four identical c-silicon nanostructures have provided up to six degrees of freedom (three arbitrary amplitudes and another three for arbitrary phases) to design three sets of a printing-holographic image as shown in Figure 1.7b [46]. With two pairs of identical poly-silicon nanostructure, a full-colour vectorial hologram can be developed [47]. The reconstructed holographic images can be selectable by different polarization angles of the incident LP light as shown in Figure 1.7c.

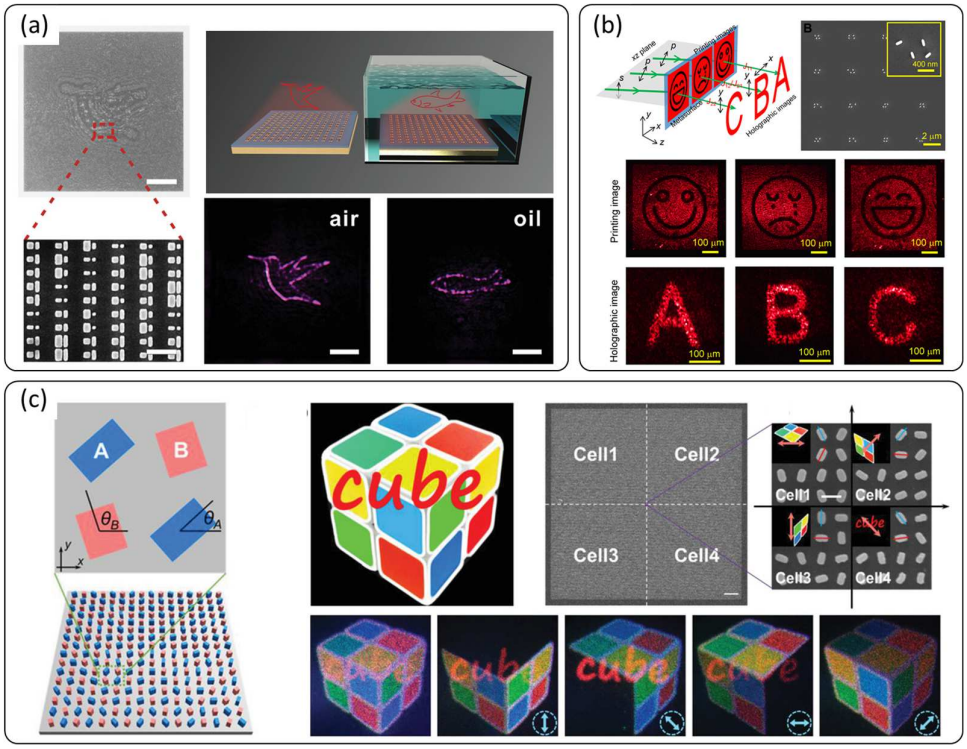

Figure 1.7 Metaholograms with composite unit cells. (a) Surrounded-medium-dependent holography [45]. (b) Six degrees of freedom holography [46]. (c) Full-polarization degree of freedom holography [47].

1.3.4. Optical Vortex Beams

Light traveling through a free space can rotate around a propagation axis. This rotation is a behaviour of angular momentum of light, which can be spin angular momentum (SAM) and orbital angular momentum (OAM). SAM refers to circular polarization, and OAM refers to the twisting of a wavefront. OAM can be generated by using a spiral phase plate, resulting in an azimuthal distribution of the phase profile of a light beam. The azimuthal phase distribution can be described as $\exp(i\ell\theta)$, where ℓ $(\pm 1, \pm 2, \pm 3, \dots)$ is the topological charge and θ is the azimuthal angle. A higher value of the topological charge corresponds to a faster twisting of the wavefront around the propagation axis. The capability of optical metasurfaces that can generate a spatial phase change opens a new opportunity to generate OAM beams as shown in Figure 1.8 [48]. The fundamental OAM beams have been experimentally demonstrated with a V-shape plasmonic resonator [10] (Figure 1.8a), a PB-phase-based gold nanorod (Figure 1.8b) [11], a PB-Phase-based silicon nanopillar (Figure 1.8c) [49], and a combination-phase-based TiO_2 nanopillar (Figure 1.8d) [50]. Furthermore, a multichannel superposition of OAM beams with different ℓ has also been reported [51].

The metadevices involving the OAM generation and detection have brought fascinating applications in a real scenario. As shown in Figure 1.9a, a metadevice can be used to perform the Fourier transform for edge enhancement [52]. Figure 1.9b, the OAM of light has increased the optical bandwidth for communication with ℓ dependent output information [53]. In Figure 1.9c, the metadevice up to 200 channels (using $\ell = \pm 50$) has been experimentally demonstrated to display holographic videos at two different image planes [54].

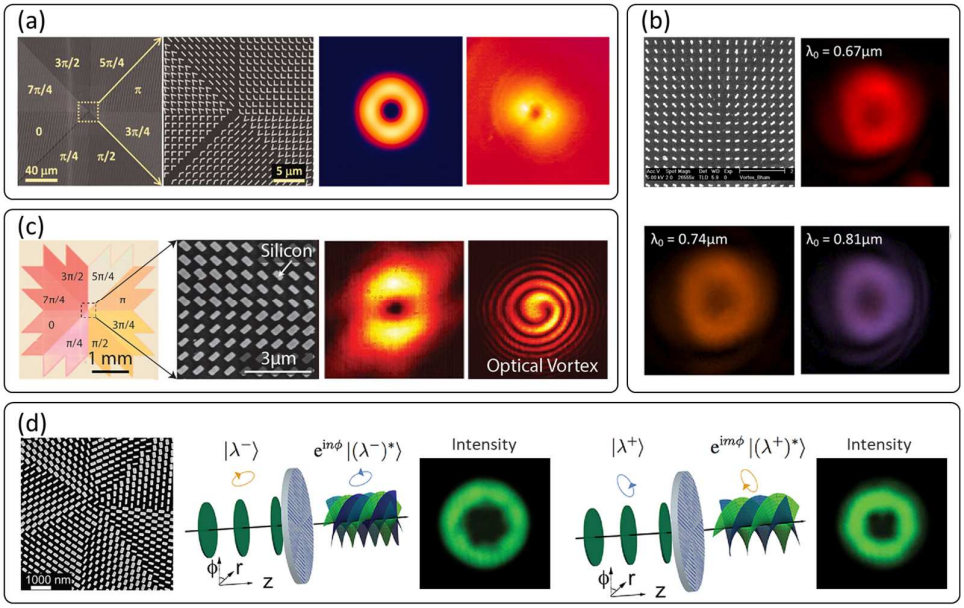

Figure 1.8 The evolution of OAM beams generated by optical metasurfaces [48]. Generation of a fundamental OAM beam with (a) V-shape-based metasurface [10], (b) PB-phase-based gold nanorods [11], (c) PB-phase-based silicon nanopillars [49], and (d) combined phase-based metasurface [50].

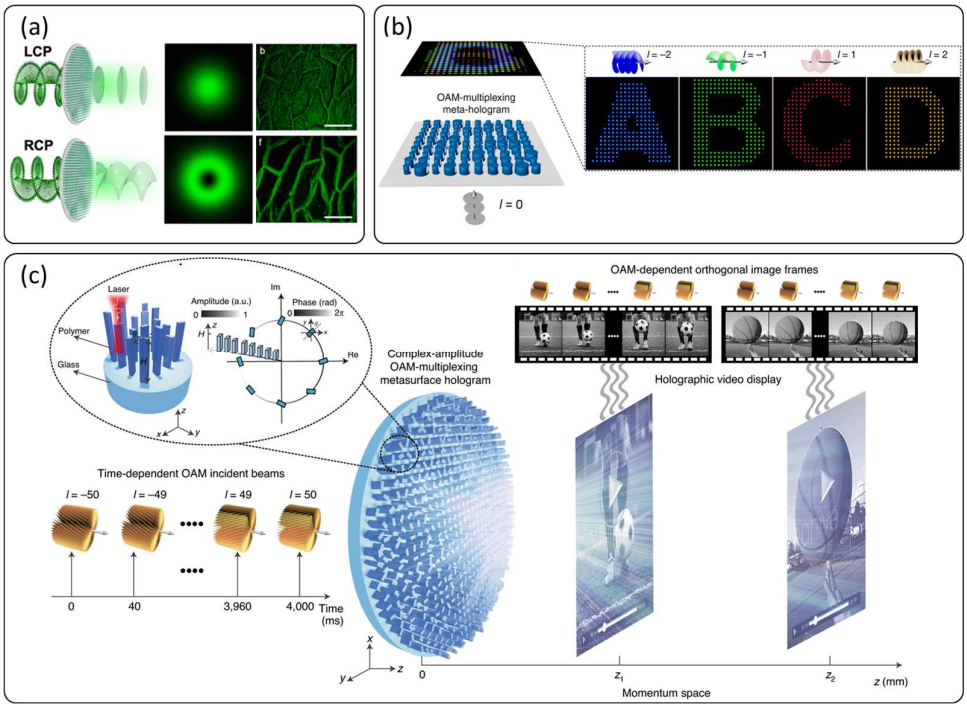

Figure 1.9 Applications of metasurfaces involving in OAM beams. (a) Edge enhancement [52]. (b) Optical communication [53]. (c) Video display [54].

1.3.5. Polarization Manipulation

As we know, traditional wave retarders such as half-waveplates (HWP) and quarter-waveplates (QWP) can be used to manipulate the polarization of light. However, they have a bulky size and are unable to spatially control the polarization states with a sub-wavelength resolution. Optical metasurfaces provide an ability to spatially manipulate a polarization state of light with a pixel size less than an operation wavelength. By utilising geometric metasurfaces, spatially linear polarization profiles can be realised. With the PB phase, the rotation angle of each polarization direction is two times the orientation angle of a corresponding nanostructure. Due to a uniform intensity, the polarization profile cannot be seen by direct observation. Thus, the aid of an analyser is required for modulation to see the intensity distribution. The intensity distribution is proportional to the square of the cosine of angle θ between the transmission axes of the analyser and the polarizer, i.e., $I = I_0 \cos^2 \theta$. It is worth mentioning that the intensity distribution can be seen on a surface of a metadevice. As shown in Figure 1.10a, a polarization profile encoded with a grayscale image has been hidden in a uniform intensity of a light beam. When an analyser is used, the grayscale image is revealed [55]. By utilising the dielectric-based colour filter, colour image concealment can be realised as shown in Figure 1.10b [56]. A dual-channel metasurface has been designed to provide two different images when

the transmission axis of an analyser is 90° or 45° with respect to (w.r.t.) the x-axis as shown in Figure 1.10c. In this design, each nanostructure is associated with both modulated intensity for 90° and 45° of the transmission axes of the analyser [57]. The combination of the PB phase and propagation phase has been utilised to demonstrate multifunctionality by encoding vectorial holograms into polarization profiles [58]. The information can be revealed by using an analyser as illustrated in Figure 1.10d. Lensing can also be encoded into a polarization profile as depicted in Figure 1.10e [59]. So far, the intensity distribution can be revealed by assisting crossed, parallel, 45° polarizers. Recently, arbitrary angles of a polarizer and analyser can be designed by utilising a composite unit cell of two nanostructures [60]. As an example in Figure 1.10f, the transmission axes of an analyser can be 17° and 73°. The potential applications of such metasurfaces are optical anti-counterfeiting and image encryption.

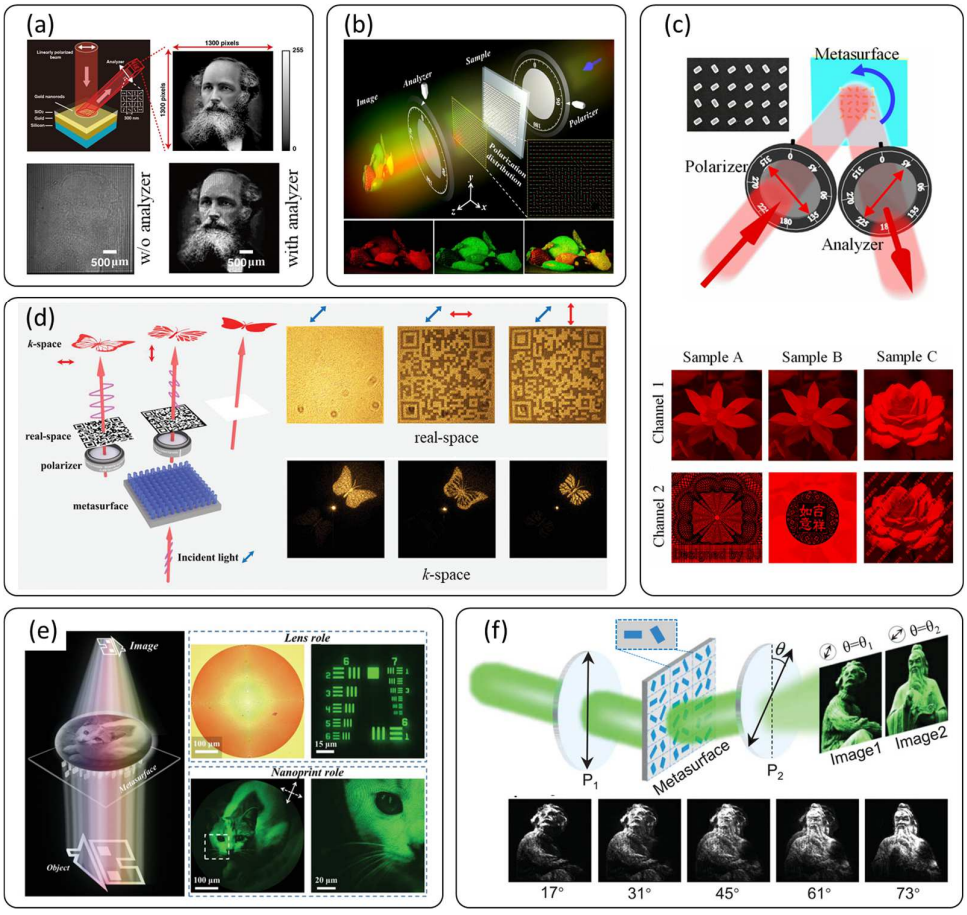

Figure 1.10 Metasurfaces for spatial polarization manipulation. (a) Grayscale image hidden in the light beam [55]. (b) Colour image encoded into a metasurface [56]. (c) Two-channel grayscale images [57]. (d) Polarization holography encoded into grayscale images [58]. (e) Nanoprinting-based metalens [59]. (f) Nonorthogonal grayscale mages [60].

1.3.6. Nonlinear Metasurfaces

As mentioned in the previous sections, light manipulation by optical metasurface-based devices is based on a linear regime. In other words, the frequencies of input and output light beams remain the same. In this section, optical metasurfaces for nonlinear devices will be discussed. There are many geometries of nanostructures that respond to the exciting electric field (namely fundamental wave: FW) and provide *n*th harmonic radiation. The harmonic order *n* can be selected based on the rule of $n = lm \pm 1$, where *l* is an integer, *m* refers to the m-fold of a nanostructure, and the "+" and "–" signs express the spin states of FW and harmonic radiation with same and opposite spins, respectively [61]. Such *m*-fold rotational symmetry can be used to generate harmonic waves (HW) with a geometric phase of $(n-1)\theta\sigma$ or $(n+1)\theta\sigma$ for the n^{th} HW as shown in Figure 1.11a, where σ represents the LCP (+) and RCP (–) light [61, 62].

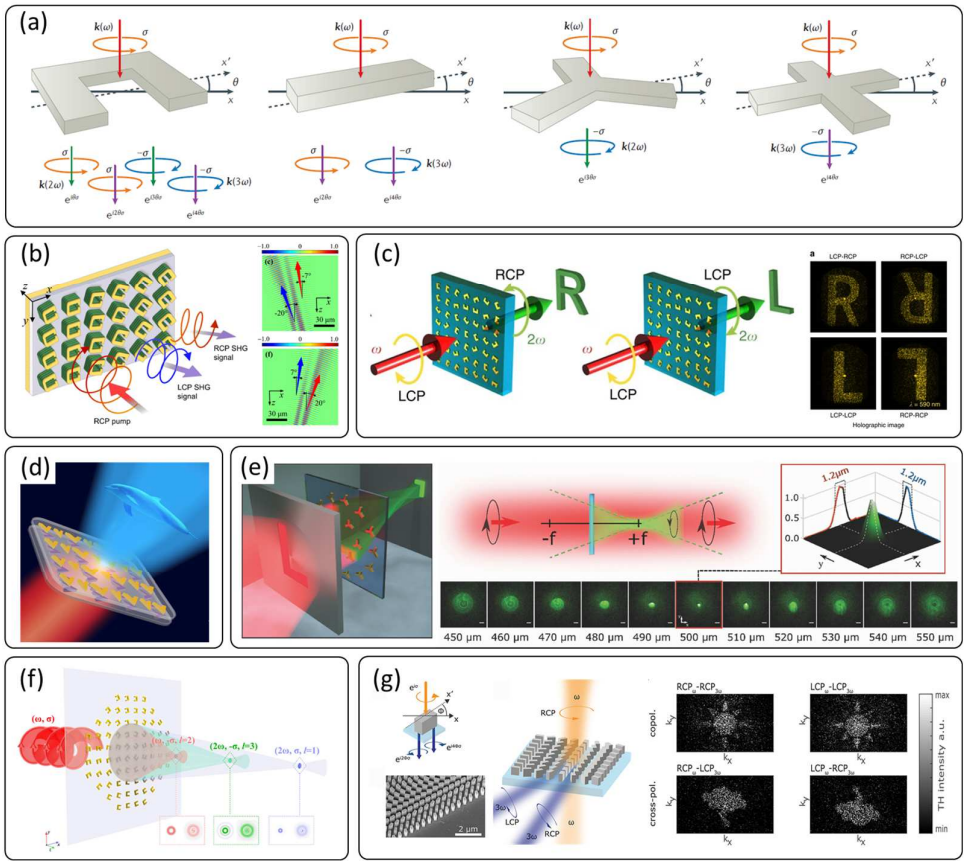

Figure 1.11 (a) Configuration of nonlinear elements for harmonic generation [62]. (b) Nonlinear phase gradient [63]. (c) Nonlinear hologram [64]. (d) Multilayer nonlinear holography [65]. (e) C3 for nonlinear metalens [66]. (f) OAM manipulation [67]. (g) Dielectric-based nonlinear metasurface [68].

Regarding the several output signals from a onefold element in Figure 1.11a(left), dual beam steering [63] and optical holography [64] for the second harmonic frequency can be generated. One has the same polarization state as the incident and another has the opposite state as shown in Figure 1.11b-c. In Figure 1.11d, the nonlinear metasurface has paved the creation of volumetric information by reconstructing different holographic images along the z-direction [65]. The imaging through the nonlinear metalens has also been demonstrated subsequently [66] (Figure 1.11e). Three focused OAM beams with different topological charges can be simultaneously generated, one from linear ($2\theta\sigma$) and two ($\theta\sigma \; and \; 3\theta\sigma$) from nonlinear phenomenon [67] (Figure 1.11f). Not only plasmonic-based metasurfaces providing nonlinearity, but a dielectric-based metasurface with silicon nanostructures can also produce the third harmonic generation [68]. As shown in Figure 1.11g, high fidelity of polarization-dependent holographic images can be obtained.

1.4. Aim and Objectives

Optical metasurfaces have revolutionized the optical design in both linear and nonlinear optics. In addition, device miniaturization and system integration are two continuing trends. The ultrathin nature of optical metasurfaces and their unprecedented capability in light control have provided a compact platform to develop ultrathin optical metasurface devices with novel functionalities that are very difficult or impossible to achieve with conventional optics. Due to the simplicity of the design and fabrication, this thesis is mainly focused on geometric optical metasurfaces, which are superior to other types of metasurfaces. Polarization is one of the fundamental properties of light, which has been used in many research fields. The work in this thesis includes nanostructure design, engineered functionality design, sample fabrication, device characterisation, and applications of developed metadevices. The metadevices were developed for polarization generation, detection and imaging as illustrated in Figure 1.12 and can be enumerated as follows.

1. Polarization generation in two and three-dimensional spaces, including
    1.1. Two-dimensional polarization structures
    1.2. Three-dimensional polarization structures
    1.3. Wavelength-selective digital numbers
    1.4. Nonlinear polarization profile
2. Polarization detection with novel methods, including
    2.1. Hybrid hologram

2.2. Light's orbital angular momentum

2.3. Optical ring vortex beams

3. Polarization Imaging for a multifunctional microscope, including

3.1. Polarization and edge imaging

3.2. Investigation of biological samples

3.3. Large-area imaging

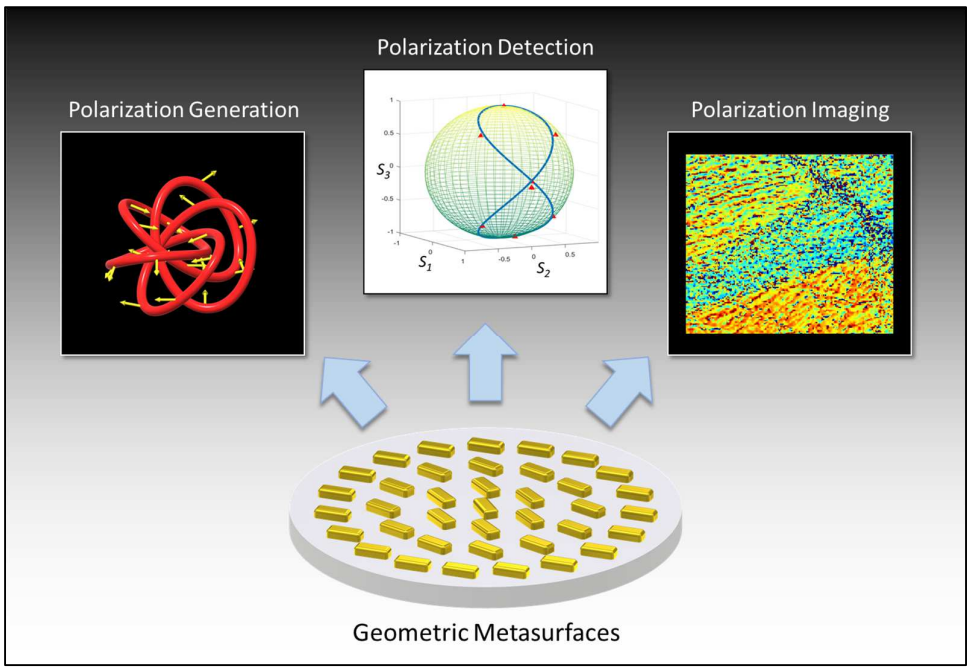

Figure 1.12 Schematic diagram of the aims of this thesis.

1.5. Thesis Outline

This thesis starts with an introduction part in Chapter 1 to introduce and give relevant backgrounds of metasurfaces and their applications. Chapter 2 includes the methods and relevant theoretical backgrounds used to design, develop, and also characterise the optical metadevices. From Chapters 3 to 5, this thesis is involved in the experimental details about our developed optical metadevices. In other words, Chapter 3 is focused on the utilisation of metalenses to generate polarization structures in 2D and 3D spaces. Chapter 4 includes the demonstration of the metadevices to detect a polarization state of an incident light beam using hybrid holography, optical vortices, and light's orbital angular momentum. Chapter 5 consists of a practical application of the metasurfaces to simultaneously perform circular polarization detection and edge detection in a single optical system. Finally, the main conclusions to the developed metadevices and a personal outlook for future applications of metasurfaces are given in Chapter 6.

CHAPTER 2 – FUNDAMENTALS OF GEOMETRIC METASURFACES AND DEVICE FABRICATION

In the first chapter, the state-of-the-art in metasurfaces and their emerging applications have been reviewed. In this chapter, the methods and relevant theoretical backgrounds used to design, develop, and characterise the optical metadevices reported in this thesis will be presented. We give details on polarization states of light, the generation of geometric phases with metasurfaces, and the design and fabrication procedure of our developed metadevices. The details of our experimental setup to test the metadevices and dynamically control the polarization state of the incident light beam as well as compress the strong intensity of the unwanted light beam are also given.

2.1. Polarization States of Light

Geometric metasurfaces are polarization-sensitive devices, whose functionalities can be obtained by controlling the helicity of the circularly polarized (CP) light. CP light is referred to the electromagnetic field that has a constant magnitude and rotates at the same rate in a plane perpendicular to the propagating direction. CP light can be either left-circularly polarized (LCP) light when the rotation direction is anticlockwise (Figure 2.1a) or right-circularly polarized (RCP) light when the rotation direction is clockwise (Figure 2.2a). Linearly polarized (LP) light is the electromagnetic field that has a magnitude changing with time on a single plane that is perpendicular to the propagating direction. LP light is composed of LCP and RCP light with equal amplitude as shown in Figure 2.1c. In case the amplitudes of LCP and RCP light are inequality, the superposition of these two CP components becomes elliptically polarized (EP) light as shown in Figure 2.1d. Left-elliptically polarized (LEP) light is generated when the amplitude of the LCP light is higher than the RCP light. Right-elliptically polarized (REP) light is generated when the RCP light is higher than the LCP light. Thus, the geometric metasurfaces can also be operated under the illumination of both LP light and EP light.

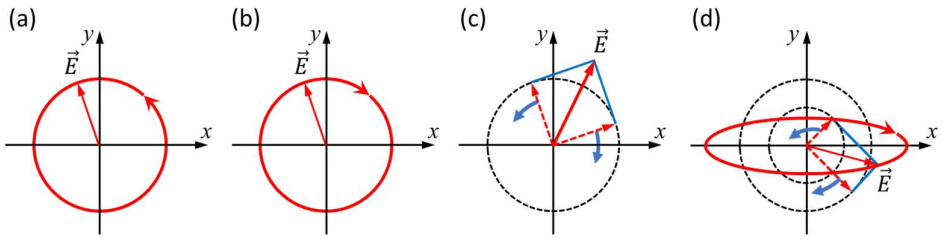

Figure 2.1 Polarization states of light. (a) Left-circularly polarized (LCP) light. (b) Right-circularly polarized (RCP) light. (c) Linearly polarized (LP) light decomposed into LCP and RCP. (d) The same for elliptical polarized (EP) light.

Fully polarized light beams can be represented by Jones vectors as shown in Table 1, and Jones matrices are used to represent optical elements as shown in Table 2. In an optical system, the output polarization of light after travelling through an optical element can be described by using the product of the Jones matrix of the optical element and the Jones vector of the incident light.

Table 1 Jones vectors for various polarization states.

Polarization	Jones Vector
LP light in the direction of angle θ w.r.t. the x-axis	$\begin{pmatrix} \cos\theta \\ \sin\theta \end{pmatrix}$
LP light in the direction of angle 0° w.r.t. the x-axis	$\begin{pmatrix} 1 \\ 0 \end{pmatrix}$
LP light in the direction of angle 90° w.r.t. the x-axis	$\begin{pmatrix} 0 \\ 1 \end{pmatrix}$
LP light in the direction of angle +45° w.r.t. the x-axis	$\frac{1}{\sqrt{2}}\begin{pmatrix} 1 \\ 1 \end{pmatrix}$
LP light in the direction of angle −45° w.r.t. the x-axis	$\frac{1}{\sqrt{2}}\begin{pmatrix} 1 \\ -1 \end{pmatrix}$
RCP light	$\frac{1}{\sqrt{2}}\begin{pmatrix} 1 \\ -i \end{pmatrix}$
LCP light	$\frac{1}{\sqrt{2}}\begin{pmatrix} 1 \\ i \end{pmatrix}$

Table 2 Jones matrices for optical elements.

Optical Element	Jones Matrix
Linear polarizer with transmission axis at θ w.r.t. the x-axis	$\begin{pmatrix} \cos^2\theta & \sin\theta\cos\theta \\ \sin\theta\cos\theta & \sin^2\theta \end{pmatrix}$
Arbitrary phase retarder with phase difference of ϕ and fast axis at θ w.r.t. the x-axis	$e^{-\frac{i\phi}{2}}\begin{pmatrix} \cos^2\theta + e^{i\phi}\sin^2\theta & (1-e^{i\phi})\sin\theta\cos\theta \\ (1-e^{i\phi})\sin\theta\cos\theta & \sin^2\theta + e^{i\phi}\cos^2\theta \end{pmatrix}$
Quarter-wave plate with fast axis at θ w.r.t. the x-axis	$e^{-\frac{i\pi}{4}}\begin{pmatrix} \cos^2\theta + i\sin^2\theta & (1-i)\sin\theta\cos\theta \\ (1-i)\sin\theta\cos\theta & \sin^2\theta + i\cos^2\theta \end{pmatrix}$
Half-wave plate with fast axis at θ w.r.t. the x-axis	$e^{-\frac{i\pi}{2}}\begin{pmatrix} \cos 2\theta & \sin 2\theta \\ \sin 2\theta & -\cos 2\theta \end{pmatrix}$

2.2. Geometric Phase

Several optical devices have been reported with metasurfaces based on optical scatters [10], but the feature size of the antennae has to be carefully designed to obtain the desired phase changes ranging from 0 to 2π with a fixed wavelength. To simplify the nanofabrication and broadband response, this thesis will focus on a geometric metasurface that can produce an abrupt phase shift by using an identical nanoantenna, but spatially varying an orientation angle (δ). In general, the space-variant birefringence property of a nanoantenna can be written as,

$$T(\delta) = R(-\delta)\begin{bmatrix} T_x & 0 \\ 0 & T_y \end{bmatrix}R(\delta) \tag{2.1}$$

where $T_x = t_x e^{i\varphi_x}$ and $T_y = t_y e^{i\varphi_y}$ are the transmission along x and y-direction. The rotation matrix here is given by

$$R(\delta) = \begin{bmatrix} \cos\delta & \sin\delta \\ -\sin\delta & \cos\delta \end{bmatrix} \tag{2.2}$$

With the incident LCP light beam, $\frac{1}{\sqrt{2}}\begin{pmatrix} 1 \\ i \end{pmatrix}$, the transmitted light can be written as,

$$T(\delta)\cdot LCP = \frac{T_x+T_y}{2}\cdot LCP + \frac{T_x-T_y}{2}\cdot e^{i2\delta}\cdot RCP \tag{2.3}$$

Here, there are two components generated by the nanoantenna in a unit cell. The first component is the light beam with the same helicity as the incident beam (also called the non-converted part). The second component is the light beam with the opposite helicity

and additional PB phase shift of 2δ (converted part). The terms $\frac{T_x+T_y}{2}$ and $\frac{T_x-T_y}{2}$ are the propagation phases which are relative to the width, length, and thickness of the nanoantenna. With the incident RCP light beam, $\frac{1}{\sqrt{2}}\begin{pmatrix}1\\-i\end{pmatrix}$, the transmitted light can be written as,

$$T(\theta)\cdot RCP = \frac{T_x+T_y}{2}\cdot RCP + \frac{T_x-T_y}{2}\cdot e^{-i2\delta}\cdot LCP \tag{2.4}$$

The transmitted light in Equation 2.4 is also similar to Equation 2.3, but the additional PB phase shift is -2δ. As obviously shown in Equations 2.3 and 2.4, the non-converted parts can be eliminated by using the nanoantenna providing $t_x \cong t_y$ and $\varphi_y - \varphi_x = \pm\pi$ to obtain a maximum conversion efficiency. Then only the strongly converted part with an abrupt PB phase shift $\pm 2\delta$ can transmit through the designed unit cell.

2.3. Geometric Phase with a Gold Nanorod

The reported metadevices in this thesis have been mostly exploited by transmissive metasurfaces with a single layer of rectangular gold nanostructures. We can use silver instead of gold to obtain a higher conversion efficiency [57], but the disadvantage is that silver samples are much easier to get oxidized. This can affect the performance of the developed metadevices. With a gold nanostructure, it is difficult for optimisation to obtain $\varphi_y - \varphi_x = \pm\pi$. Here, we consider a gold nanostructure (or a gold nanorod) as a polarizer with poor quality [11, 23]. In this scenario, a poor polarizer is a combination of a perfect polarizer and a piece of normal flat glass slab that can only add a uniform phase profile (not a spatially variant phase profile). In this thesis, the metadevices and other optical elements are treated with the Jones vectors and Jones matrices to represent the polarization state of the light beam and the functionality of an optical element. Thus, the Jones matrix of each nanorod (J_{rod}) can be written as

$$J_{rod} = A\begin{bmatrix}1 & 0\\ 0 & 1\end{bmatrix} + B\begin{bmatrix}\cos^2\delta & \sin\delta\cos\delta\\ \sin\delta\cos\delta & \sin^2\delta\end{bmatrix}, \tag{2.5}$$

where δ is an orientation angle of each nanorod w.r.t. the x-axis. The unit matrix $\begin{bmatrix}1 & 0\\ 0 & 1\end{bmatrix}$ represents the flat glass slab. A and B are the coefficients of the conversion efficiency of that glass slab and nanorods, respectively. When the polarization state of the incident light beam is circular polarization (CP), the output beam can be expressed as

$$J_{rod}\,|L(R)\rangle = \frac{2A+B}{2}|L(R)\rangle + \frac{B}{2}e^{\pm i2\delta}|R(L)\rangle, \quad (2.6)$$

where $|L\rangle$ and $|R\rangle$ represent LCP and RCP, respectively. The transmitted light includes two main parts: non-converted $\left[\frac{2A+B}{2}|L(R)\rangle\right]$ and converted parts $\left[\frac{B}{2}e^{\pm i2\delta}|R(L)\rangle\right]$. The non-converted part has the same property as that of the incident beam, while the converted part has an additional phase shift $\pm 2\delta$ generated by the geometric metasurface, where '+' and '–' represent the sign of the phase shift for incident LCP and RCP light, respectively. The phase shift is known as Pancharatnam–Berry (PB) phase or the geometric phase [69-71]. By changing the orientation angle δ of the nanorod in each unit cell, the phase shift can be tuned, ranging from 0 to 2π. The relation between the desired phase profile (φ) for x and y coordinates and the corresponding orientation angles of the nanorods are given by $\delta_{(x,y)} = \varphi_{(x,y)}/2$.

2.4. Transmissive Metasurfaces

2.4.1. Design

The transmissive metadevices reported in this thesis are realized based on plasmonic metasurfaces, which consist of identical gold nanorods with spatially variant orientations sitting on a glass substrate to produce the PB phase shifts. Each nanorod is 200 nm long, 80 nm wide, and 40 nm high, which is the same as our previous works [11, 23]. The pixel size of a unit cell is 300×300 nm^2 as depicted in Figure 2.2a. Its simulated conversion efficiency is shown in Figure 2.2b, which is realized by using the frequency domain solver of the Computer Simulation Technology (CST) Microwave Studio software. In the simulation, the permittivity of a gold nanorod is calculated by the Drude model with the plasma frequency ω_p = 1.37 × 10^{16} rad/s, and the collision frequency γ_c = 1.215 × 10^{14} rad/s. The refractive index of the glass substrate is 1.46. The unit cell boundary is used along the x- and y-directions, and an open boundary condition is used along the z-direction. After the simulation process is done with CST, scattering parameters or S-parameters are exported to calculate the conversion efficiency. The exported data is included the wavelengths and their corresponding amplitudes of the converted and non-converted parts. By taking a square of those amplitudes, the conversion efficiency can be obtained as shown in Figure 2.2b. Although the non-converted part is extremely high, it can be filtered out by using the experimental setup explained in Section 2.4.3.

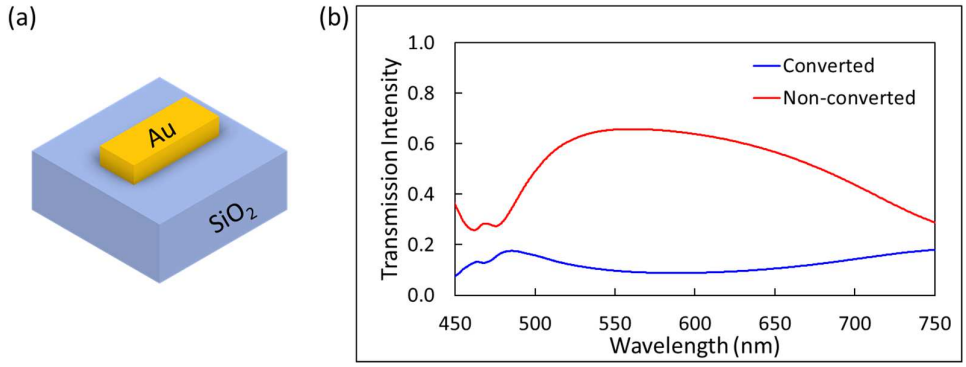

Figure 2.2 (a) A designed unit cell and (b) its simulated conversion efficiency versus wavelengths.

2.4.2. Nanofabrication

Once an optical metadevice with novel functionalities has been designed as shown in Figure 2.3a and its phase profile has been generated as shown in Figure 2.3b, the pattern for nanofabrication is then created (Figure 2.3c). The pattern is created by using a MATLAB code, which consists of an array of nanorods with different orientation angles. In the MATLAB code, the coordinates of each nanorod are exported to a text file (*.txt), which is transferred to the electron beam lithography (EBL) by loading the file as the ASC format (*.asc). Then, the pattern for fabrication is generated on the EBL and ready for the next step. After that, the standard EBL is used to fabricate the designed metadevices, followed by film deposition and the lift-off process as illustrated in Figure 2.3d.

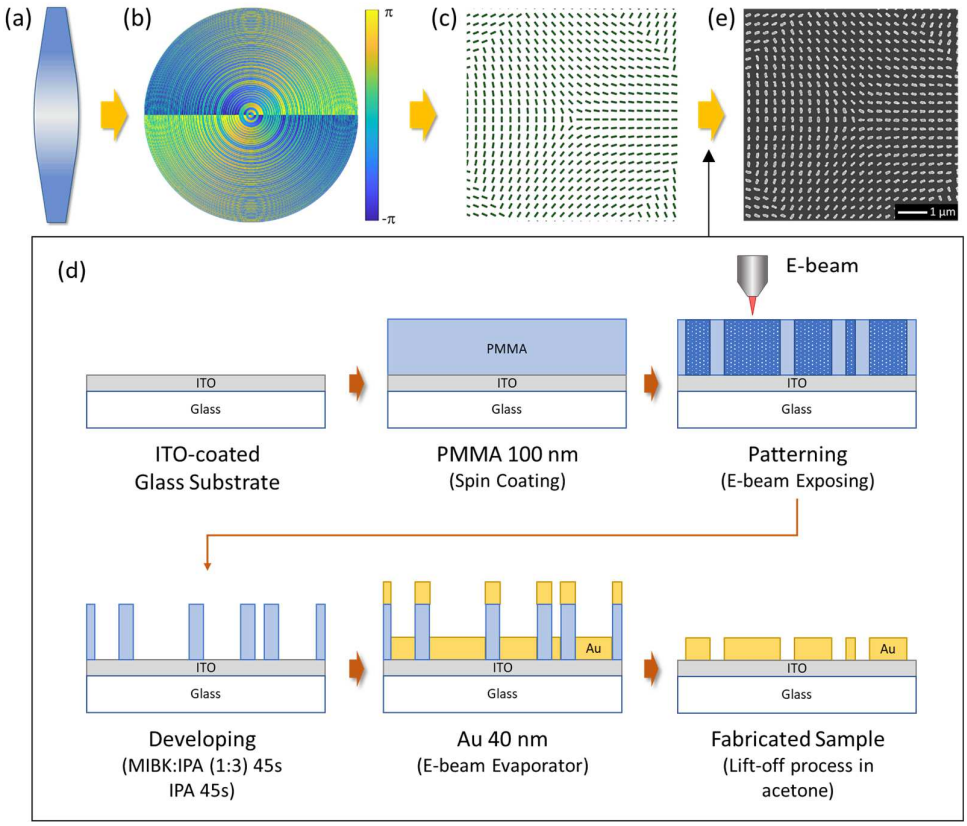

Figure 2.3 Procedure for development of transmissive metadevices. (a) Desired functionality. (b) Generated phase profile. (c) Generated patterns for fabrication. (d) Fabrication procedure of transmissive metadevices. (e) SEM image.

First, the ITO-coated glass substrate is cleaned with acetone for 10 mins and isopropyl alcohol (IPA) for 10 mins in an ultrasonic bath. Then, the substrate is rinsed in deionized water and dried with a nitrogen gun. The positive polymethyl methacrylate (PMMA) 950 A2 resist is spin-coated on the SiO_2 layer at 1000 rpm for 60 s followed by 1500 rpm for 15 s, producing a 100-nm-thick PMMA. After that, the sample is baked on a hotplate at 180 °C for 5 mins. The EBL (Raith PIONEER, 30 kV) with an aperture size of 20 μm and a working distance of 10 mm is used to define nanopatterns in the PMMA film. The sample is developed in MIBK:IPA (1:3) for 45 s followed by the stopper (IPA) for 45 s. A gold film (40 nm) is deposited on the sample using an electron beam evaporator. Finally, the metadevices are fabricated after the lift-off process in acetone and the fabricated patterns can be seen by using a scanning electron microscope (SEM) as a result in Figure 2.3e, for example. At this moment, the metadevice is ready for characterisation.

Time for each step is very important and has to be precisely controlled. Otherwise, there will be no gold nanorods sitting on the substrate. For the sample size of 300 × 300 μm^2, the overall fabrication time is around 9 hours, including sample preparation (30 minutes),

a patterning process by the e-beam machine (2 hours), e-beam deposition (30 minutes), and a lift-off process in acetone (6 hours).

As shown in Figure 2.3, there are several steps in the fabrication procedure. Each step can affect the feature size of the nanorods, which can be smaller or larger than the design. In terms of functionalities, the difference in size between the fabricated and the designed nanorods does not affect the designed functionalities as long as the nanorods still have rectangular shapes and do not overlap with the neighbouring unit cells. This is the robustness of geometric metasurfaces against fabrication errors. In terms of conversion efficiency, the fabrication error plays an important role [72]. The level of imperfection that can be tolerated depends on the functionality of devices. For examples, the metasurface holograms have better fabrication tolerances (e.g., 5% of missing nanostructures) than metalenses for imaging.

2.4.3. Experimental Setup

The diagram of an experimental setup to characterize the fabricated metadevices that provide the functionalities along an optical axis is shown in Figure 2.4. A light beam with tuneable wavelengths is generated by a supercontinuum laser source (NKT Photonics SuperK EXTREME). Polarization states of the generated beam can be controlled by using a linear polarizer (P1) and a quarter-waveplate (QWP1) in front of the metadevice (see details in Section 2.6). A convex lens (L1) is used to weakly focus the light beam onto the metadevice. An objective lens (Obj.) with a magnification of 20×, a convex lens (L2), and a charge-coupled device (CCD) camera are used to collect the output light and image the results for visualization. Another pair of a quarter-waveplate (QWP2) and a linear polarizer (P2) behind the objective lens is used to filter out the unconverted part of the transmitted light. To characterize the metadevice with an incident LP light beam, both QWP1 and QWP2 are removed, and the transmission axes of the P1 and P2 are kept perpendicular to each other.

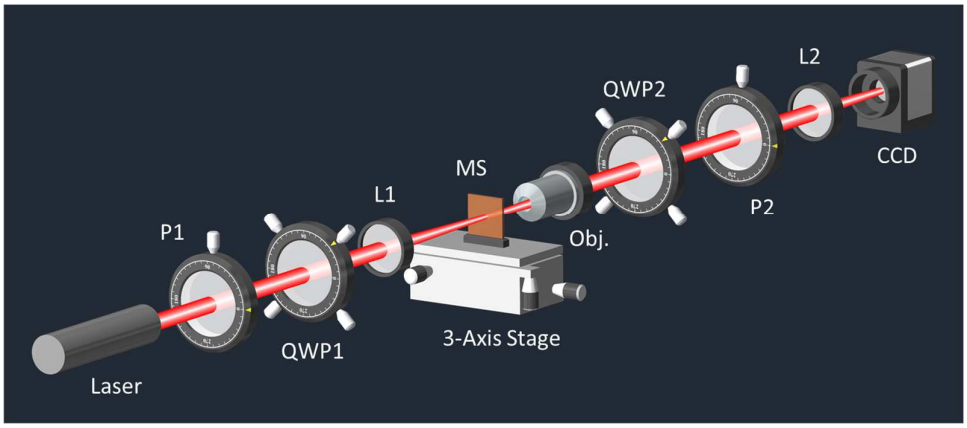

Figure 2.4 Schematic diagram of the experimental setup to characterise the transmissive metadevices providing the functionalities along an optical axis. P1 and P2: Polarizers, QWP1 and QWP2: Quarter-waveplates, L1: Convex lens (f=15 cm), MS: Metasurface device, Obj.: 20× Objective lens, L2: Convex lens (f=10 cm), and CCD: Charge-coupled device.

Generation of CP light (LCP and RCP): LP light beam (E_{in}) is generated by the polarizer P1 with the transmission axis along the x-direction. Thus, its Jones vector is given by $E_{in} = \begin{bmatrix} 1 \\ 0 \end{bmatrix}$. The polarization state of the E_{in} can be changed by using the quarter-waveplate, QWP1, whose Jones matrix is given by

$$J_{QWP1} = e^{-\frac{i\pi}{4}} \begin{bmatrix} \cos^2\beta_1 + i\sin^2\beta_1 & (1-i)\sin\beta_1\cos\beta_1 \\ (1-i)\sin\beta_1\cos\beta_1 & \sin^2\beta_1 + i\cos^2\beta_1 \end{bmatrix} \quad (2.7)$$

where β_1 is the orientation angle of the fast axis w.r.t. the x-direction. When the E_{in} passes through the QWP1 with the angle β_1 of $\frac{\pi}{4}$, the output vector can be calculated by

$$J_{QWP1}E_{in} = e^{-\frac{i\pi}{4}} \begin{bmatrix} \cos^2\frac{\pi}{4} + i\sin^2\frac{\pi}{4} & (1-i)\sin\frac{\pi}{4}\cos\frac{\pi}{4} \\ (1-i)\sin\frac{\pi}{4}\cos\frac{\pi}{4} & \sin^2\frac{\pi}{4} + i\cos^2\frac{\pi}{4} \end{bmatrix} \begin{bmatrix} 1 \\ 0 \end{bmatrix} = \frac{1}{\sqrt{2}} \begin{bmatrix} 1 \\ -i \end{bmatrix} \quad (2.8)$$

Here, an RCP light beam is generated. When the angle β_1 is $-\frac{\pi}{4}$, an LCP is then generated. After the RCP and LCP light pass through a nanorod, the result can be expressed as in Equation 2.6, where the geometric phase can be produced.

Filtering out the non-converted part from the incident CP light beam: As mentioned above, the non-converted part from a plasmonic metasurface used in this thesis is extremely high. To filter out the non-converted part, a pair of a quarter-waveplate (QWP2) and a linear polarizer (P2) is used. The Jones matrix of the QWP2 is the same as whose QWP1, but the fast axis is defined as β_2. The Jones matrix of the P2 (J_{P2}) is given as

$$J_{P2} = \begin{bmatrix} \cos^2\vartheta & \sin\vartheta\cos\vartheta \\ \sin\vartheta\cos\vartheta & \sin^2\vartheta \end{bmatrix} \tag{2.9}$$

where ϑ is an angle of the transmission axis of the P2 w.r.t. the *x*-axis. In this case, the angle β_2 is set parallel to β_1, which is $\frac{\pi}{4}$. The angle ϑ is set to 0 which is parallel to whose P1. After the non-converted part (E_{nc}) passing through the P2, it can be filtered out as follows

$$J_{P2}J_{QWP2}\frac{2A+B}{2}RCP = \begin{bmatrix} 0 \\ 0 \end{bmatrix} \tag{2.10}$$

After the converted part (E_c) passing through the P2, the output vector can be written as

$$J_{P2}J_{QWP2}\frac{B}{2}e^{-i2\delta}LCP = \frac{B}{2}e^{-i2\delta}\begin{bmatrix} 1 \\ 0 \end{bmatrix} \tag{2.11}$$

Here, the non-converted part is filtered out and the output vector is solely relative to the geometric phase, -2δ, for the incident RCP light. For the incident LCP light, the angles are $\beta_1 = \beta_2 = -\frac{\pi}{4}$ and $\vartheta = 0$. Then, the output vector is solely relative to 2δ.

Incident linearly polarized (LP) light beam: For the incident LP light, the QWP1 and QWP2 are removed. The Jones matrix of the LP light beam is given by $\begin{bmatrix} \cos\alpha \\ \sin\alpha \end{bmatrix}$, where α is the polarized direction. When the LP beam generated by a linear polarizer P1 passes through a nanorod, the Jones vector can be written as

$$J_{rod}\ LP = \frac{2A+B}{2}\cdot\begin{bmatrix} \cos\alpha \\ \sin\alpha \end{bmatrix} + \frac{B}{2}\begin{bmatrix} \cos\ (2\delta-\alpha) \\ \sin\ (2\delta-\alpha) \end{bmatrix} \tag{2.12}$$

There are two components coming out from the nanorod, a non-converted part: $E_{nclp} = \frac{2A+B}{2}\cdot\begin{bmatrix} \cos\alpha \\ \sin\alpha \end{bmatrix}$ and a converted part: $E_{clp} = \frac{B}{2}\begin{bmatrix} \cos\ (2\delta-\alpha) \\ \sin\ (2\delta-\alpha) \end{bmatrix}$.

Filtering out the non-converted part from the incident LP light beam: After the non-converted part (E_{nclp}) passing through the polarizer P2, the output vector can be written as

$$E_{nclp}^{out} = J_{P2}E_{nclp} = \begin{bmatrix} cos^2\vartheta & sin\vartheta\,cos\vartheta \\ sin\vartheta\,cos\vartheta & sin^2\vartheta \end{bmatrix}\frac{2A+B}{2}\cdot\begin{bmatrix} \cos\alpha \\ \sin\alpha \end{bmatrix} \tag{2.13}$$

To filter out the E_{nclp}, the angle ϑ has to be perpendicular to the angle α. Thus, the ϑ can be $\alpha \pm \frac{\pi}{2}$. Therefore, the non-converted part can be filtered out as follows

$$E_{nclp}^{out} = \frac{2A+B}{4}\left\{\begin{bmatrix}\cos\alpha\\ \sin\alpha\end{bmatrix} + \begin{bmatrix}\cos\ (\alpha \pm \pi)\\ \sin\ (\alpha \pm \pi)\end{bmatrix}\right\} = \begin{bmatrix}0\\0\end{bmatrix} \tag{2.14}$$

At this moment, the output vector of the converted part passing through the analyser can be written as

$$E_{clp}^{out} = J_{P2}E_{clp} = \frac{B}{4}\left\{\begin{bmatrix}\cos\ (2\delta-\alpha)\\ \sin\ (2\delta-\alpha)\end{bmatrix} - \begin{bmatrix}\cos\ (3\alpha-2\delta)\\ \sin\ (3\alpha-2\delta)\end{bmatrix}\right\} \tag{2.15}$$

Here, the non-converted part is filtered out and the output vector is relative to the polarization direction α of the incident LP and the spatial orientation angle δ of the nanorods. Equation 2.15 can be used to spatially manipulate a polarization profile with a sub-wavelength resolution and the intensity distribution can be revealed by an analyser.

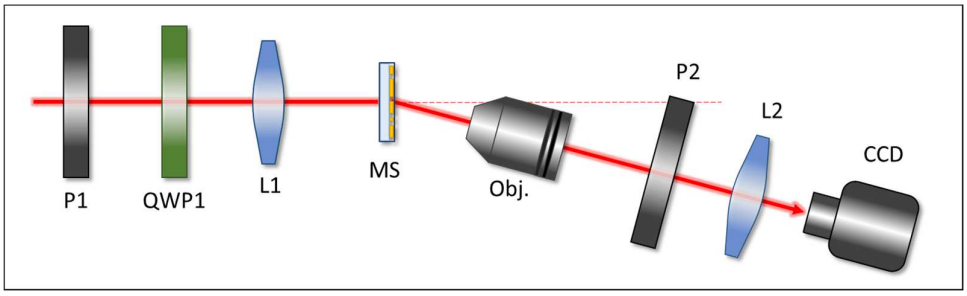

Figure 2.5 Schematic diagram of the experimental setup to characterise the transmissive metadevices with off-axis design. P1: polarizer; P2: analyser; QWP1: quarter-wave plate; L1 and L2: lenses (f = 100 mm); MS: metasurface; Obj.: 10× objective lens; CCD: charge-coupled device.

Figure 2.5 is used for characterisation of the transmissive metadevices with an off-axis design. The polarizer P1 and the QWP1 are used for controlling the polarization state of the input light. Arbitrary polarization states such as linear, circular and elliptical polarization states can be generated. The lens L1 (f = 100 mm) is used to weakly focus the input light onto the metasurfaces. The transmitted light is collected by an objective with a magnification of 10× and a lens L2 (f = 100 mm). For the case of superposition of OAM beams with the same circular polarization, the analyser P2 is not needed. The superposition of OAM beams with different circular polarizations can result in vector beams, which can be revealed with aid of the analyser P2.

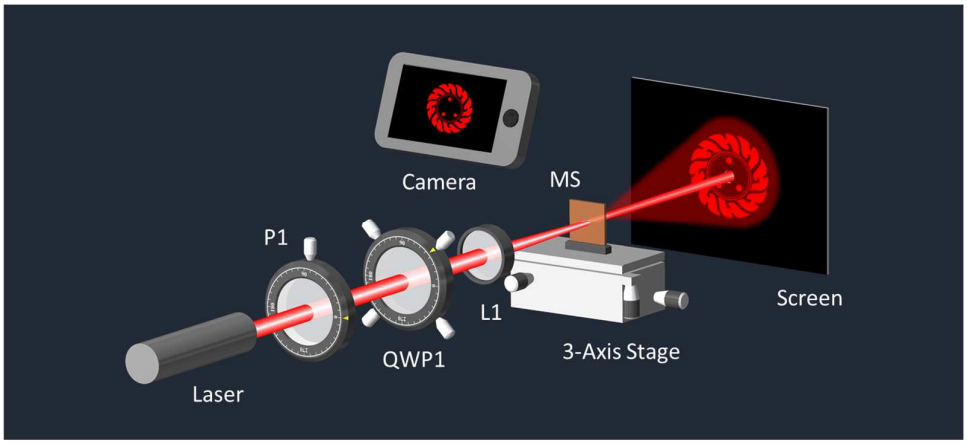

Figure 2.6 Schematic diagram of the experimental setup to characterise the transmissive metadevices providing the functionalities along an optical axis. P1: Polarizer, QWP1: Quarter-waveplate, L1: Convex lens (f=15 cm), MS: Metasurface device.

The experimental setup in Figure 2.6 is used to obtain the functionalities that cannot be directly captured using a CCD camera, i.e., holographic images. In the experiment, a white screen is placed behind a test sample. A digital camera is then situated in front of the incident plane to capture the reconstructed image on the screen.

2.5. Reflective Metasurfaces

2.5.1. Design

The reflective metadevices reported in this thesis consist of identical gold nanorods (length 200 nm, width 80 nm, and height 30 nm) with spatially varying orientations sitting on the SiO_2 layer (85 nm) and gold ground layer (150 nm) which is similar to our previous works [39, 51]. The pixel size of a unit cell is 300×300 nm^2 as depicted in Figure 2.7a. The triple-layer structure functions like a Fabry-Perot-like cavity, where the SiO_2 spacer in the middle corresponds to the cavity length. The incident light (E_{in}) is decomposed to E_l along a long part and E_s along a short part of the nanorod. E_l carries a phase shift by π after reflection by the nanorod. E_s experiences a multiple reflection inside the cavity, leading to the round tripe phase by π and the additional reflection phase by π from the gold ground layer. Thus, the nanorods along with the spacer and the background layer function as a reflective-type half-waveplate ($\varphi_s - \varphi_l = \pi$). In addition, the designed thickness of 85 nm for SiO_2 provides a broad response over the visible region [12]. When the incident light is circularly polarized, the reflectivity for the co-polarized and cross-polarized light is calculated as shown in Figure 2.7b, which is realized by using the frequency domain solver of the CST Microwave Studio software. In the simulation, the permittivity of a gold nanorod is calculated by the Drude model with the plasma

frequency $\omega_p = 1.37 \times 10^{16}$ rad/s, and the collision frequency $\gamma_c = 1.215 \times 10^{14}$ rad/s. The refractive index of SiO_2 and silicon are 1.45 and 3.45, respectively. The unit cell boundary is used along the x- and y-directions, and the open boundary condition is used along the z-direction. Figure 2.7b shows that most of the incident light is converted by the metadevice within a broad range of wavelengths. The red and blue curves represent the cross-polarized and co-polarized light, respectively.

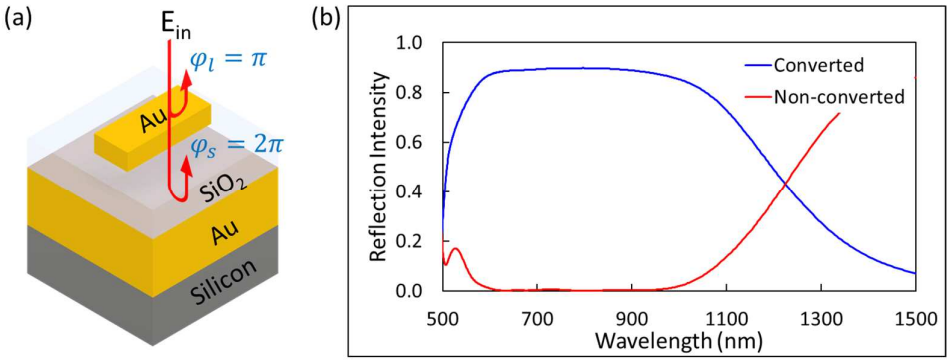

Figure 2.7 (a) A designed unit cell and (b) its simulated conversion efficiency versus wavelengths.

2.5.2. Nanofabrication

Similar to the transmissive metadevices, after novel functionalities have been designed (Figure 2.8a), its phase profile has been generated (Figure 2.8b), and the pattern has been created (Figure 2.8c), the standard nanofabrication process in Figure 2.8d is then carried on. The standard EBL is used to fabricate the designed metadevices, followed by film deposition and the lift-off process. First, silicon substrates are cleaned with acetone in an ultrasonic bath for 10 min followed by IPA for 10 min. Then the substrates are rinsed in deionized water and dried with compressed air. After that, the gold layer (150 nm) is deposited onto the silicon substrate by using the electron beam evaporator followed by the deposition of the SiO_2 layer (85 nm). The film thickness is controlled by using a calibrated film thickness monitor. The positive PMMA 950 A2 resist is spin-coated on the SiO_2 layer at 1000 rpm for 60 s followed by 1500 rpm for 15s, producing a PMMA film with a thickness of 100 nm. Then the sample is baked on a hotplate at 180 ^oC for 5 mins. The nanopatterns are defined in the PMMA film using EBL (Raith PIONEER, 30 kV) with an aperture size of 20 μm and a working distance of 10 mm. The sample is developed in MIBK:IPA (1:3) for 45 s followed by a stopper (IPA) for 45 s. A thin gold layer (30 nm) is deposited on the developed sample using an electron beam evaporator.

For the adhesion purpose, a thin titanium layer (3 nm) is deposited on the SiO_2 layer before the gold layer. Finally, the metadevices are ready for characterization after the lift-off process in acetone as shown in Figure 2.8e, for example.

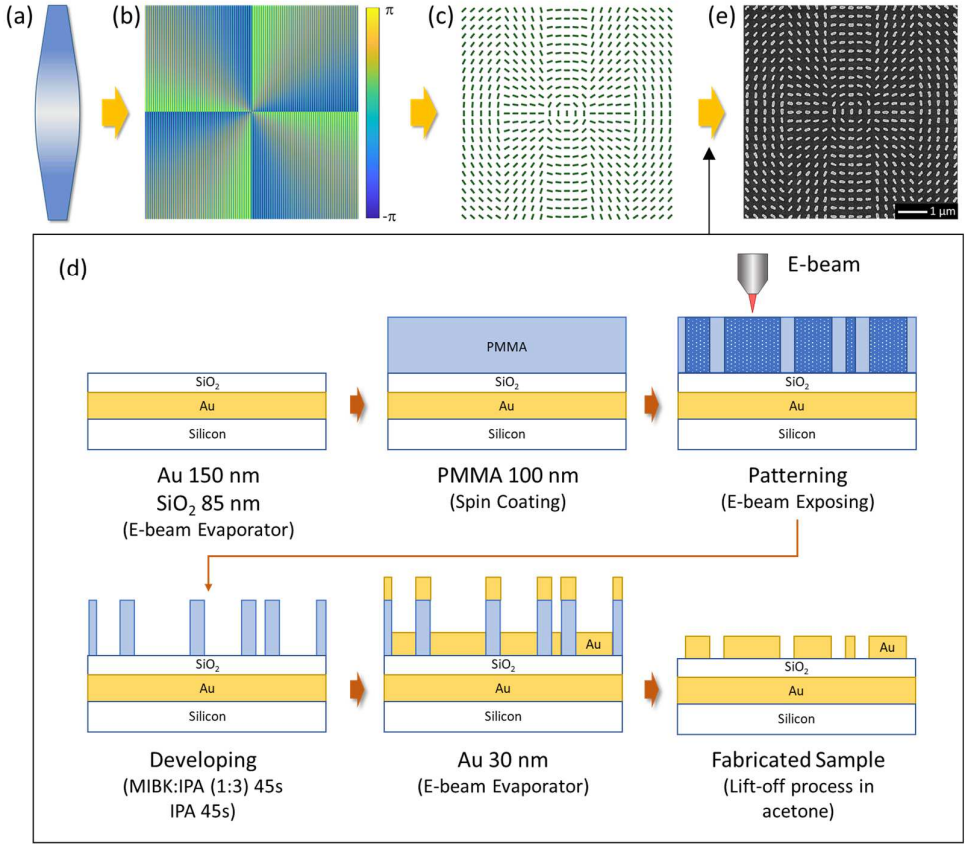

Figure 2.8 Procedure for development of reflective metasurfaces. (a) Desired functionality. (b) Generated phase profile. (c) Generated patterns for fabrication. (d) Fabrication procedure of reflective metadevices. (e) SEM image.

2.5.3. Experimental Setup

The experimental setup to characterise the reflective metadevices is shown in Figure 2.9. A tuneable laser source (NKT-SuperK EXTREME) is used to generate the desired laser beam. Polarization states of the generated beam can be controlled by using a linear polarizer (P1) and a quarter-waveplate (QWP1) in front of the metadevice (see details in Section 2.6). A convex lens (L1) is used to weakly focus the light beam onto the metadevice which is sitting on a 3-axis stage. A digital camera is used to collect the displayed patterns on the screen after passing through a sheet of polariser (P2) whose transmission axis is fixed along the horizontal direction. The distance between the screen and the metasurface can be adjustable from 5 to 15 cm. The experiment is suitable for observation of the reconstructed pattern on the screen that can be directly seen by the

naked eye. Notably, the screen and P2 have small holes in the middle to allow the incident light to pass through.

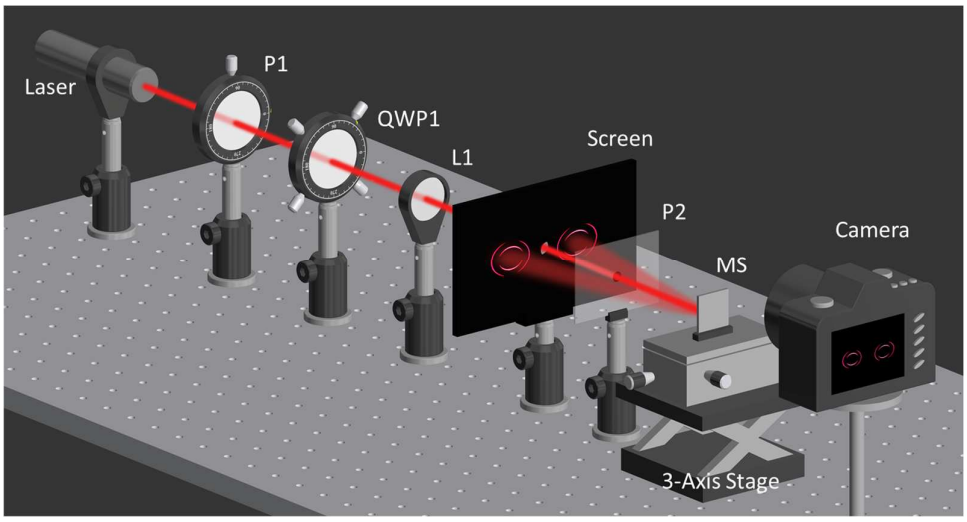

Figure 2.9 Schematic diagram of the experimental setup to characterise the reflective metadevices. P1 and P2: Polarizers, QWP1: Quarter-waveplate, L1: Convex lens (f=15 cm), MS: Metasurface device.

For small patterns created by the refractive metadevices, the experimental setup illustrated in Figure 2.10 is used. In this experiment, an objective lens (Obj.) with a magnification of 20×, a convex lens (L2), and a charge-coupled device (CCD) camera are used to collect the output light and image the results for visualization. As most of our developed metadevices are based on off-axis design, the QWP2 in both setups (Figure 2.9 and 2.10) is not necessary. The P2 is only used to analyse a polarization distribution of the patterns coming out from the metadevices.

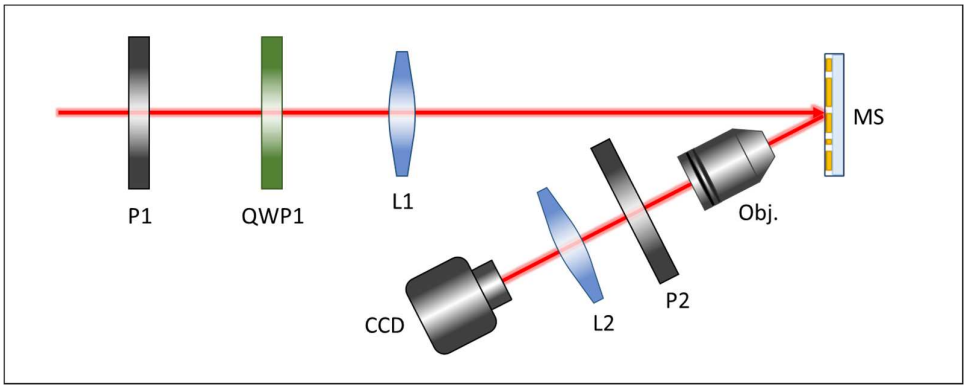

Figure 2.10 Schematic diagram of the experimental setup to characterise the refractive metasurfaces providing small patterns.

2.6. Generation of Incident Light with the Various Polarization States

As briefly discussed in Section 2.4.3 about the generation of LCP and RCP light with a pair of P1 and QWP1, this section will be covered the generation of any arbitrary polarization state used in this thesis. Suppose the P1 generates an LP light in the direct of α w.r.t. the x-axis, its associated Jones vector is $\begin{bmatrix} \cos\alpha \\ \sin\alpha \end{bmatrix}$. Taking the Jones matrix of the QWP1 from Equation 2.7 into account, the LP light after passing through the QWP1 can be written as

$$J_{QWP1}LP = e^{-\frac{i\pi}{4}} \begin{bmatrix} \cos^2\beta_1 + i\sin^2\beta_1 & (1-i)\sin\beta_1\cos\beta_1 \\ (1-i)\sin\beta_1\cos\beta_1 & \sin^2\beta_1 + i\cos^2\beta_1 \end{bmatrix} \begin{bmatrix} \cos\alpha \\ \sin\alpha \end{bmatrix} \quad (2.16)$$

Here, the output product can be expressed as

$$J_{QWP1}LP = a\begin{bmatrix} 1 \\ -i \end{bmatrix} + b\begin{bmatrix} 1 \\ i \end{bmatrix} \quad (2.17)$$

where

$a = \frac{\sqrt{2}}{4}\big(\sin 2\beta_1\cos\alpha + \cos\alpha - \cos 2\beta_1\sin\alpha + i(-\cos 2\beta_1\cos\alpha - \sin 2\beta_1\sin\alpha + \sin\alpha)\big)$

and

$b = \frac{\sqrt{2}}{4}\big(-\sin 2\beta_1\cos\alpha + \cos\alpha + \cos 2\beta_1\sin\alpha + i(-\cos 2\beta_1\cos\alpha - \sin 2\beta_1\sin\alpha - \sin\alpha)\big)$ are the components of RCP and LCP light, respectively. Here, different polarization states of incident light are obtained by rotating the angle α and β_1.

2.7. Explanation of our Characterisation Method

The device design is mainly based on the phenomena in the far-field. We usually use one sample for proof-of-concept demonstration. To obtain the statistical data, such as standard variation or any errors from the fabrication process, sample characterisation, and lifetime of the metadevices, we have to fabricate more metasurface samples. However, nanofabrication cost is very expensive. So, we usually do not have the statistical data to show in the experimental results, such as error bars in the polarization detection, and the fabrication errors against the designs. Due to the imperfection of the fabricated samples (loss of gold nanostructures) and misalignment of optical setups, there is slight difference between experiment and simulation. However, the difference is acceptable for concept

demonstration. Further improvement will include the optimization of the fabrication process and optical alignment.

2.8. Summary

In this chapter, the theoretical details about the geometric metasurfaces are provided. Both reflective and transmissive types of optical metasurfaces have been developed by using a standard electron-beam lithography, film deposition, and lifting-off process. Different experimental setups are built to characterize the developed metasurface devices and evaluate their performances. The next chapter will concentrate on the experimental details of specific metadevices and their unusual functionalities.

CHAPTER 3 – POLARIZATION GENERATION WITH METASURFACES

In the first two chapters, the relevant physical background of optical metasurfaces and their unprecedented capability in light manipulation at the subwavelength scale have been reviewed. In this chapter, we will focus on the utilisation of the optical metasurfaces based on the geometric phase to develop metadevices for creating polarization structures in two-dimensional (2D) and three-dimensional (3D) spaces. In this chapter, Sections 3.3, and 3.4.1 have already been published in Nano Letter 2021 [72], where my main contributions include sample fabrication, experimental setup, sample characterisation, and data analysis. Work done in Section 3.6 has been published in Physical Reviewed Applied 2019 [73], where my main contribution includes the design of a polarization profile hidden in the second harmonic wave. In other sections, I have contributed to both simulation and experimental parts.

3.1. Background

Polarization has been a central concept in our understanding of optics and has found many applications ranging from quantum science [74, 75] to our daily life (e.g., polarized sunglasses and 3D cinema). Polarization control has been used to record, process, and store information [55, 56, 76, 77]. The ability to precisely control the polarization distribution of light beams is critical to both fundamental science and practical applications. Conventional optical elements (e.g., polarizers, wave plates) for polarization manipulation typically treat polarization as a uniform characteristic of an optical beam that can be globally controlled. Light beams with spatially nonuniform polarization distributions have received great attention owing to their peculiar optical features including Möbius strips with non-orientable surfaces [78], and their practical applications such as higher resolution lithography [79] and patterning of lyotropic chromonic liquid crystals by photoalignment [80]. There has been much advancement in the theoretical understanding of 2D and 3D polarization structures to further our knowledge [81, 82], but the experimental research has not advanced at the same rate. This is essentially due to the technical and fundamental challenges in creating 2D and 3D polarization profiles with conventional methods. So far, only a few types of these structures were generated at the expense of complex systems, large volume, and high cost [78, 83, 84], limiting their practical applications.

Optical metasurfaces, planar nanostructured interfaces, have attracted increasing interest due to their unprecedented capability in light manipulation at subwavelength scale [10, 12, 13, 23, 38, 39, 85-89]. The optical metasurface based flat optics has revolutionized design concepts in photonics, providing a compact platform to develop ultrathin (light wavelength scale) and lightweight planar optical devices with novel functionalities that cannot be obtained with conventional optical elements, with examples including dual-polarity lenses [23], multi-foci lenses [88], light sword lenses [87], polarization-sensitive holograms [12, 13, 39, 43, 85, 86, 89], and longitudinally variable polarization [90]. In this work, we experimentally demonstrate a single metasurface device that can change a linearly polarized incident light beam into polarization structures with a predesigned polarization profile in 2D or 3D space depending on a parametric equation of those structures, which will be detailed throughout this chapter from Section 3.2 to 3.5.

3.2. Design and Method

To create 2D or 3D polarization structures with the engineered polarization profiles, the design of a metadevice involves the multi-foci design, and polarization rotation as follows.

Design of multi-foci metasurface: To design an arbitrary multi-foci metadevice in 2D/3D space, we first formulate the phase distribution of the lens for the n^{th} focal point, which is given by

$$\varphi(x,y)_n = -\frac{2\pi}{\lambda}\left(\sqrt{f_n^2 + (x-u_n)^2 + (y-v_n)^2} - \sqrt{f_n^2 + u_n^2 + v_n^2}\right) \qquad (3.1)$$

where λ is the operating wavelength, f is the focal length, u and v are the locations of a focal point along the x and y directions, respectively. (u, v, f) are the 3D coordinates of the focal point. The position of a focal point (on the optical axis or off-axis) depends on the values of u and v. The desired field profile of the multi-foci lens is the sum of the fields for generating each focal point and the corresponding phase distribution $\Phi(x,y)$ is given by

$$\Phi(x,y) = \arg\left\{\sum_{n=1}^{N} e^{i\varphi(x,y)_n}\right\} \qquad (3.2)$$

where N is the total number of the desired focal points and n ranges from 1 to N (integer numbers).

Adding polarization rotation functionality: The multiple focal points in Equation 3.2 can only be generated for one CP light beam, while the opposite circular polarization would generate a divergent lensing effect due to the flipped sign of the phase profile.[15] To simultaneously focus an LP light beam and control its polarization direction at each focal point, a metadevice is required to focus both LCP and RCP light beams, but with different phases. The phase distribution is governed by

$$\Phi(x,y) = \arg\left\{\sum_{n=1}^{N}\left(e^{i\varphi(x,y)_n} + e^{-i\varphi(x,y)_n}\right)\right\} \tag{3.3}$$

Where the two terms $e^{i\varphi(x,y)_n}$ and $e^{-i\varphi(x,y)_n}$ are respectively responsible for focusing an LCP light beam and an RCP one. With an LP incident beam, the superposition of the LCP and RCP light beams with equal intensity at the same focal point can generate polarization rotation. Thus, the polarization direction (ϕ_n) for each focal point in Equation 3.3 can be precisely controlled with the following phase distribution of the metadevice

$$\Phi(x,y) = \arg\left\{\sum_{n=1}^{N}\left(e^{i[\varphi(x,y)_n+\phi_n]} + e^{-i[\varphi(x,y)_n-\phi_n]}\right)\right\} \tag{3.4}$$

For an LP incident beam, the overall generated output beam consists of four CP components with different phases: $A_{RCP}\cdot e^{i[\varphi(x,y)_n+\phi_n]}$, $A_{RCP}\cdot e^{-i[\varphi(x,y)_n-\phi_n]}$, $A_{LCP}\cdot e^{-i[\varphi(x,y)_n+\phi_n]}$, and $A_{LCP}\cdot e^{i[\varphi(x,y)_n-\phi_n]}$, where A_{RCP} and A_{LCP} correspond to the amplitudes of RCP and LCP light. Among these four components, $A_{RCP}\cdot e^{i[\varphi(x,y)_n+\phi_n]}$ and $A_{LCP}\cdot e^{i[\varphi(x,y)_n-\phi_n]}$ contribute to the construction of each focal point with predesigned polarization rotation. By giving a parametric equation to the parameter *u*, *v*, and *f* for the n^{th} focal point, a polarization structure with a predesigned polarization rotation can be generated.

The designed metadevices are realised by using transmissive metasurfaces as described in Section 2.4. Here, the orientation angles $\delta(x,y)$ of the nanorods are defined by $\Phi(x,y)/2$. The experimental setup shown in Figure 2.4 is used to characterise the fabricated devices. According to the predesigned polarization angle ϕ and Equation 2.15, where the angle ϕ is relative to the phase shift of 2δ by the geometric phase. Thus, Equation 2.15 can be modified to

$$E_{clp}^{out} = J_{P2}E_{clp} = \frac{B}{4}\left\{\begin{bmatrix}\cos\ (\phi-\alpha)\\ \sin\ (\phi-\alpha)\end{bmatrix} - \begin{bmatrix}\cos\ (3\alpha-\phi)\\ \sin\ (3\alpha-\phi)\end{bmatrix}\right\} \tag{3.5}$$

From Equation 3.5, the darkest intensity captured by a CCD camera can be found at the position that $\phi - \alpha = 3\alpha - \phi$. Thus, the darkest intensity or a gap of the polarization structures can be found at the generated polarization angle $\phi = 2\alpha$ as well as $\phi = 2\alpha + \pi$.

To confirm the obtained results from the experiment, the simulated 2D/3D structures are performed based on the Fresnel-Kirchhoff diffraction integration, which is governed by [91]

$$E(x,y) = \frac{z}{i\lambda}\iint_{\sum} E(x_0,y_0)\frac{e^{ikr}}{r^2}dxdy \tag{3.6}$$

where $r = \sqrt{z + (x-u)^2 + (y-v)^2}$, x and y are the coordinates of nanorods, u and v are the coordinates on the observation plane at a distance of z.

3.3. Two-Dimensional (2D) Polarization Structures

Figure 3.1 illustrates our proposed concept of a metadevice to generate a polarization structure in 2D space. Under the illumination of an LP light beam, an arbitrary focal curve with a predesigned polarization profile is obtained on the focal plane of the metadevice. The metadevice consists of gold nanorods with different in-plane orientations on a glass substrate. The polarization profile can be revealed after the transmitted light passes through a linear polarizer (analyser), which leads to various modulated intensity profiles collected by a CCD camera. In the 2D space, a ring focal curve and the Archimedean spiral focal curve have been chosen to verify and demonstrate the concept.

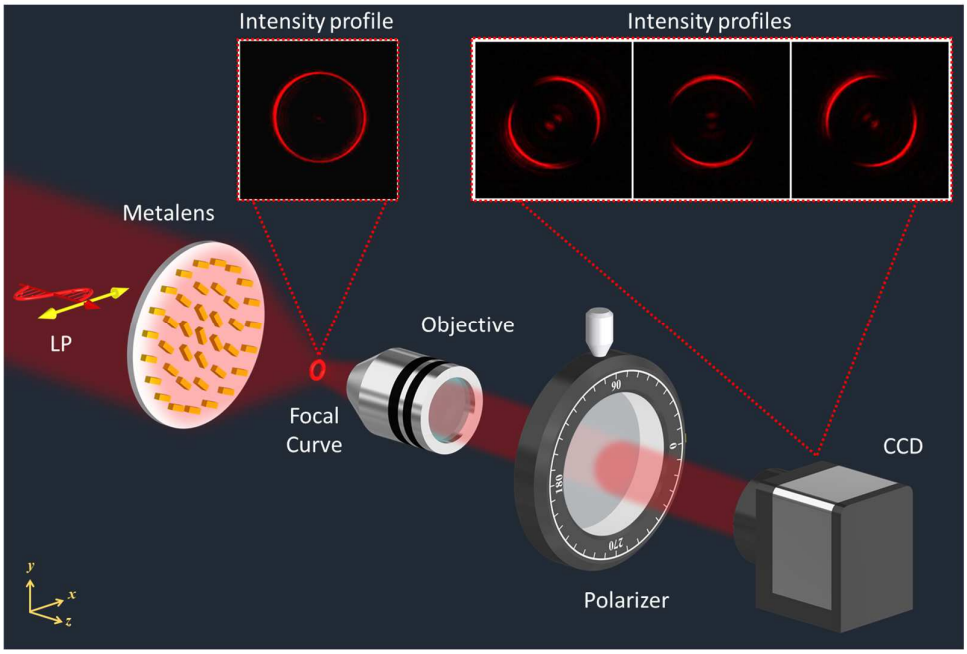

Figure 3.1 Schematic of the metadevice with customized focal curve and polarization profile.

3.3.1. Ring Focal Curve

In this design, 2000 points ($N = 2000$) are selected on the focal curve with coordinates as given by the following parametric equations,

$$\begin{cases} u_n = r\cos\phi_n \\ v_n = r\sin\phi_n \\ f_n = f_0 \end{cases} \tag{3.7}$$

The metadevice is designed to operate at the wavelength of λ = 650 nm, the focal length f_0 is 300 μm and a radius r is 30 μm. The polarization rotation angles of the points ϕ_n vary from 0 to 2π, which is along the radial direction upon the illumination of a horizontal LP light beam as shown in Figure 3.2a. The simulated intensity distribution in the focal plane is also given in Figure 3.2b, where a perfect ring focal curve can be achieved after the incident light passes through the designed metadevice. By substituting the coordinates (u_n, v_n, f_n) in Equation 3.7 to Equation 3.1, then the phase profile of the designed metadevice with a diameter of 300 μm can be calculated by using Equation 3.4 as shown in Figure 3.3a and its corresponding SEM image is shown in Figure 3.3b. At this moment, the developed metadevice is ready to characterise.

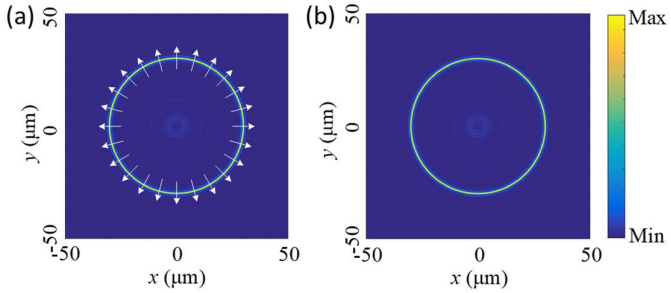

Figure 3.2 Ring focal curve with a predesigned polarization profile. (a) The polarization distribution on the ring focal curve upon the illumination of a horizontal LP light beam. (b) The simulated intensity distribution in the focal plane.

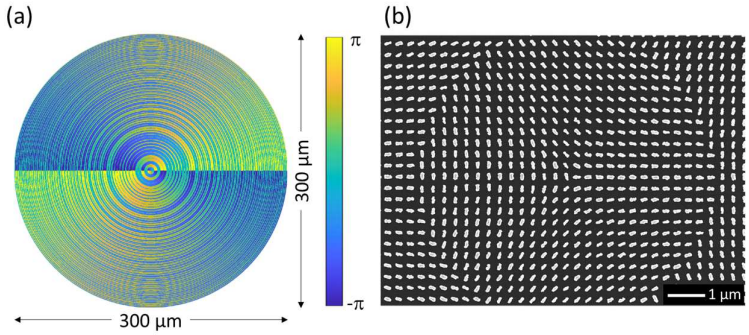

Figure 3.3 (a) The phase profile and (b) SEM image of the metadevice to generate a ring focal curve.

By testing the metadevice with the built-up experiment from Figure 2.4, Figure 3.4 shows the simulation result and the experimental result of the ring focal curve when the metadevice is illuminated by incident RCP light. The experimentally observed focal curve shows a circular shape coincides well to the simulated result. Although the intensity distribution along the focal curve is not uniform, the curve still be a continuous line with no gaps like the simulated one. The non-uniform intensity is due to the distortion of the focal curve after propagating through several optical elements, i.e., Obj., QWP2, P2, and L2 in Figure 2.4. This can be improved by making an alignment of optical path to be normally incident on the centre of all optical devices (including the developed metadevice).

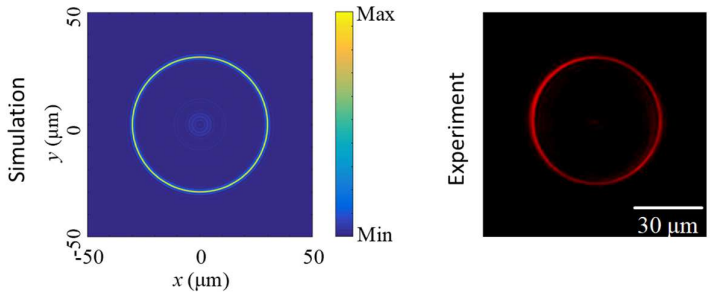

Figure 3.4 The simulated and measured intensity distributions in the focal plane under the illumination of an incident RCP light beam.

For characterization of the metadevice with an incident LP light and the measurement of the polarization profile, the two QWPs are removed, and the two polarizers are kept orthogonal to each other, which can simultaneously remove the unconverted part and reveal the polarization profile of the focal curve through the modulated intensity distribution as described in Section 2.4.3 and Equation 3.5. Figure 3.5 shows the intensity distribution of the simulated and experimental results of the focal curve for different LP directions of the incident beam, where the red and blue double arrows indicate the transmission axes of the linear polarizer and the analyser, respectively. By continuously rotating the polarizer and the analyser and maintaining their transmission axes perpendicular to each other, we can see the rotation of the gaps as predicted in theoretical analysis. The intensity distribution is modulated based on Malus' law where the minimum intensity corresponds to the positions where the predesigned polarization rotation ϕ are equal to 2α and $2\alpha + \pi$ (α is the polarization direction of the incident LP light beam w.r.t. the x-axis). The results here show that the metadevice can achieve a ring focal curve with a customized polarization profile, where the gaps can be rotated following the rotation angle of the polarization direction of the incident LP light. The size of gaps for different angles P1 is slightly different from the simulation, but it is acceptable. This difference is due to the non-uniform intensity along the curve exhibited by a pair of polarizers that shift the direction of the incident beam after rotation.

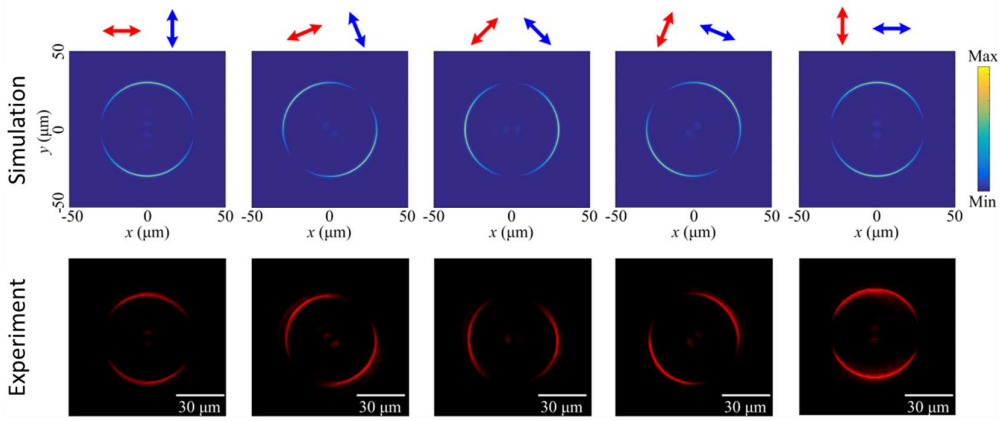

Figure 3.5 Simulation results and experimental measurement of the intensity distributions for polarization distribution detection with different transmission axes of the linear polarizer (P1) and the analyser (P2). The red and blue double arrows indicate the transmission axes of P1 and P2. P1⊥P2. From left to right, P1=0, π/8, π/4, 3π/8, and π/2, respectively.

3.3.2. Archimedean Spiral Focal Curve

In order to show that our method can be employed to design metasurfaces with any arbitrary focal curves of controlled polarization distribution, we further design and realise a metadevice that can generate an Archimedean spiral focal curve whose parametric equation is given by,

$$\begin{cases} u_n = (\zeta + \xi\phi_n)\cos\phi_n \\ v_n = (\zeta + \xi\phi_n)\sin\phi_n \\ f_n = f_0 \end{cases} \tag{3.8}$$

The focal plane is also located at f_0 = 300 μm with Archimedean spiral parameters ζ = 0 μm and ξ = 10 μm. The parameter ζ can shift the centre point of the spiral outward from the origin, while ξ can control the distance between loops. Here the polarization rotation ϕ_n is linearly ranging from 0 to π (Figure 3.6a), and 1000 points are selected along the focal curve as depicted in Figure 3.6b.

By substituting the coordinates (u_n, v_n, f_n) in Equation 3.8 to Equation 3.1, then the phase profile of the designed metadevice with a diameter of 300 μm can be calculated by using Equation 3.4 as shown in Figure 3.7a and its corresponding SEM image is shown in Figure 3.7b. At this moment, the developed metadevice is ready to characterise. Under the illumination of RCP light, the simulation and experimental results of the Archimedean spiral focal curve are shown in Figure 3.8, which agree very well with each other. The intensity of the Archimedean spiral focal curve is non-uniform due to the asymmetry of the curve shape. Upon the illumination of a horizontal LP light beam, a gap appears at the

designed position in both the simulation and experimental results as predicted (Figure 3.9) when we remove the two QWPs and change the transmission axes of the first polarizer and the analyser. Therefore, as long as the trajectory equation of the focal curve is given, a focal curve in 2D space with any shape can be achieved.

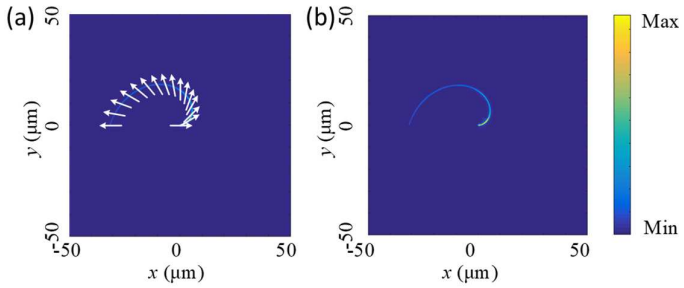

Figure 3.6 (a) Archimedean spiral focal curve with the polarization rotation angle. (b) Simulation results of the Archimedean spiral focal curve.

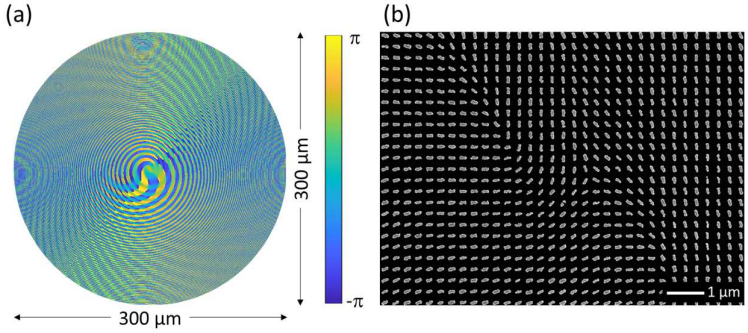

Figure 3.7 (a) The phase profile and (b) SEM image of the metadevice to generate the Archimedean spiral focal curve

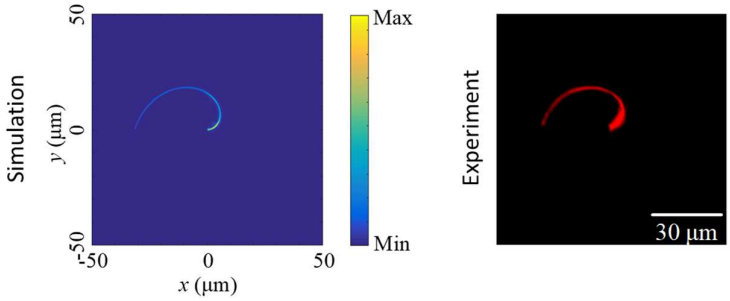

Figure 3.8 The simulated and measured intensity distribution in the focal plane under the illumination of an incident RCP light beam.

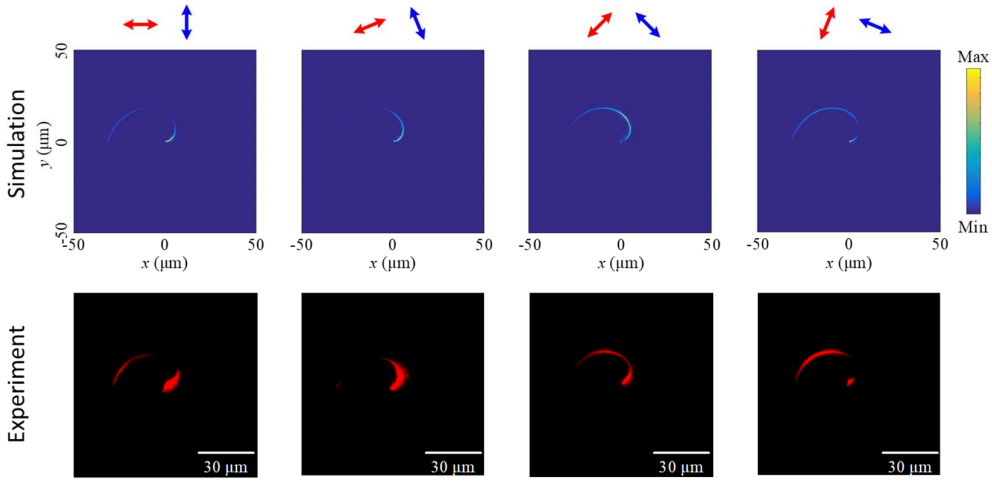

Figure 3.9 Simulation and experimental results of the intensity distributions for polarization distribution detection with different combinations of transmission axes of P1 and P2. P1⊥P2. From left to right, P1=0, π/8, π/4, and 3π/8, respectively.

3.4. Three-Dimensional (3D) Polarization Structures

Figure 3.10 shows the schematic of the metadevice to generate a 3D polarization structure. When the metadevice is illuminated by an LP beam, an arbitrarily shaped focal curve with a predefined polarization profile in 3D space can be obtained. Similar to the 2D scheme, the polarization direction at each point on the focal curve can be arbitrarily rotated relative to that of the incident beam. The generated polarization profile can be revealed by using a linear polarizer (analyser), which leads to various modulated intensity profiles collected by a CCD camera (Figure 3.10c).

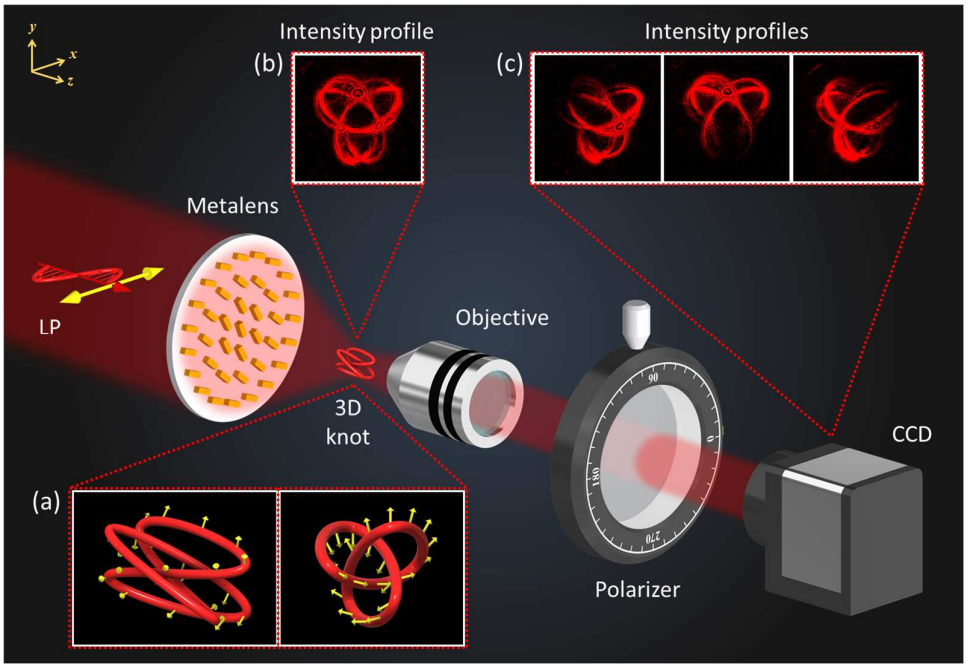

Figure 3.10 Schematic diagram of the metadevice with customized focal curve and polarization profile in 3D space. Here, we take a 3D trefoil intensity knot with a predesigned polarization profile as an example. (a) Side (left) and back (right) views of the enlarged target 3D knot with a predesigned polarization profile. The yellow arrows denote the polarization directions of the points on the knot under the illumination of a horizontal LP light beam. Measured light intensity profiles of the 2D perspective view for the incident light beam with linear polarization (b) before and (c) after passing through the polarizer (analyser). The three Figures in (c) correspond to the analyser with different transmission axes. Gold nanorod structures with various orientations on glass substrates are used to generate the designed 3D knot with a normal incidence of LP light.

3.4.1. 3D Polarization Knot

The proposed approach can be used to realize not only the focal curves in 2D space as above but also arbitrary focal curves with customized polarization profiles in 3D space. Here we demonstrate the construction of a trefoil knot structure with a local polarization texture. The coordinates of each point on the knot are parametrized by the following equations,

$$\begin{cases} u_n = a(\sin\phi_n + 2\sin 2\phi_n) \\ v_n = a(\cos\phi_n - 2\cos 2\phi_n) \\ f_n = -1.5a\sin 3\phi_n + f_0 \end{cases} \tag{3.9}$$

where the knot parameter a = 10 μm controls the size of the knot and f_0 = 300 μm defines the knot central focal plane. The perspective views of the trefoil knot are shown in Figure 3.11. The predesigned polarization distribution ϕ_n on the knot focal curve (yellow arrows) is linearly ranging from 0 to 2π.

By substituting the coordinates (u_n, v_n, f_n) in Equation 3.9 to Equation 3.1, then the phase profile of the designed metadevice with a diameter of 300 μm can be calculated by using Equation 3.4 as shown in Figure 3.12a and its corresponding SEM image is shown in Figure 3.12b. At this moment, the developed metadevice is ready to characterise.

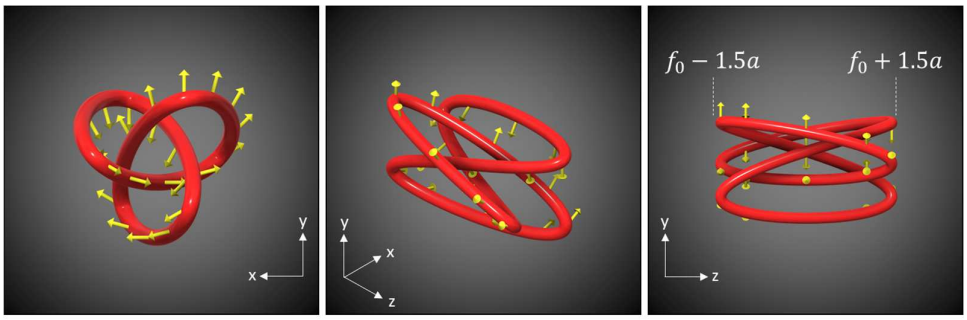

Figure 3.11 The perspective views of the 3D knot with a predesigned polarization profile (yellow arrows).

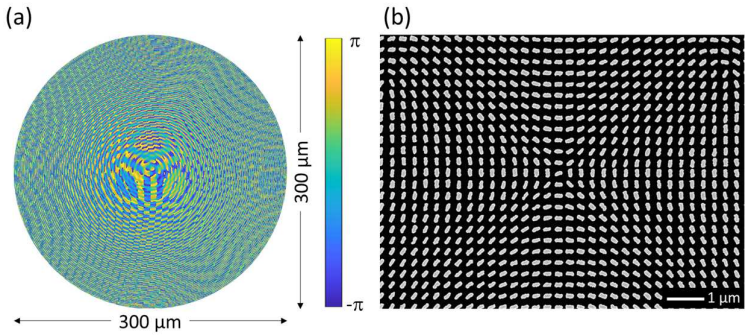

Figure 3.12 (a) The phase profile and (b) SEM image of the metadevice to generate the 3D knot.

Under the illumination of RCP light and LP light beams, the simulated and experimental results of the intensity profiles of the 2D perspective view at the focal plane of z = 285, 300, and 315 μm are presented in Figure 3.13. It shows that, as the focal plane changes, the cross-sectional intensity of the knot changes but preserves the C3 rotational symmetry. Upon the illumination of an LP light beam, each focal point on the trefoil knot has a different polarization angle, leading to the presence of two gaps on the knot after the beam passes through the analyser. By considering the Malus' law, the gaps correspond to the positions where the predesigned polarization rotation is equal to 2α and $2\alpha + \pi$ (α is the polarization direction of the incident LP light beam w.r.t. the x-axis). The gaps in the experimental measurement are clearly observed and agree well with simulation results, indicating that the designed 3D polarization knot is unambiguously realized based on the metadevice we design.

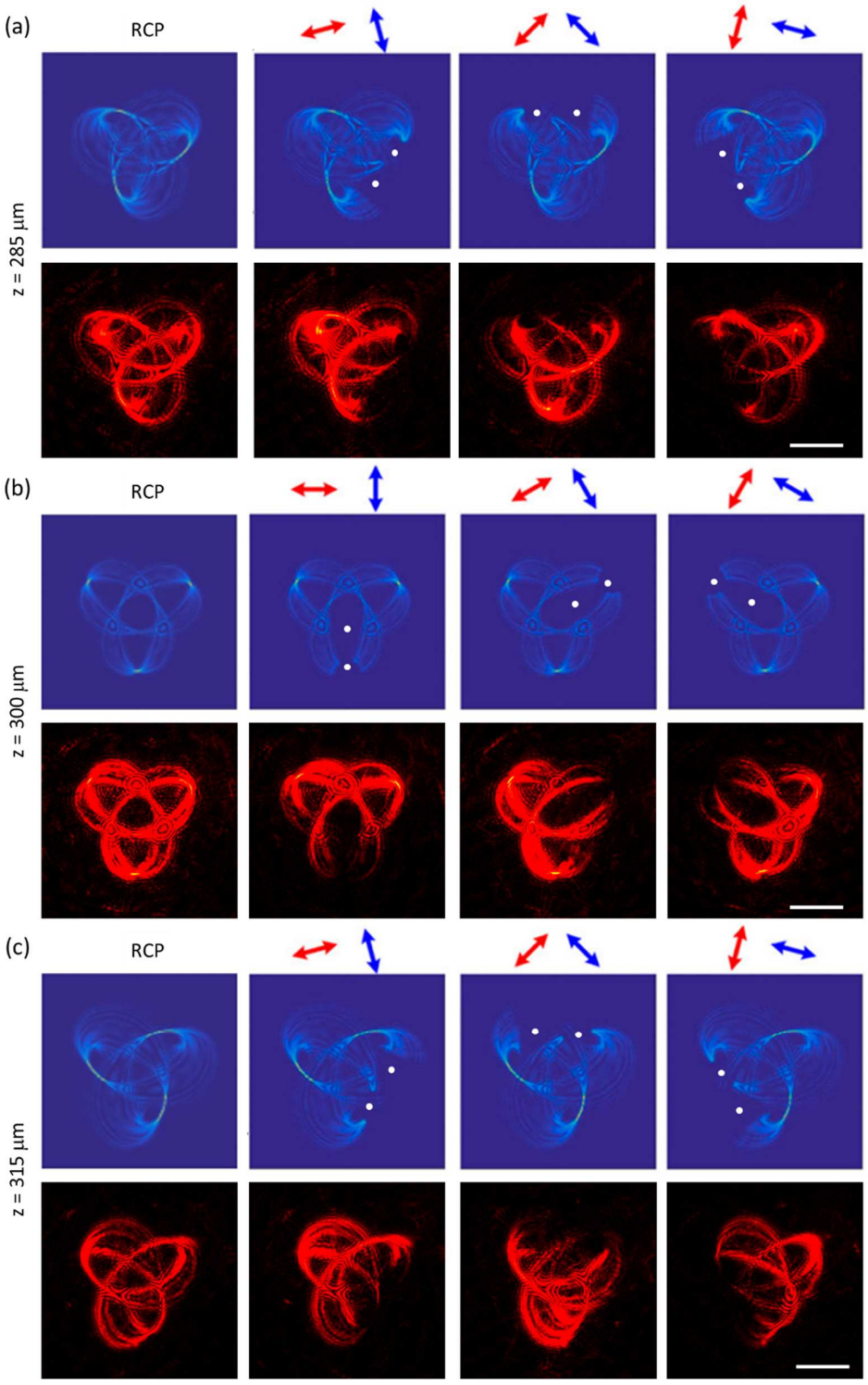

Figure 3.13 The simulated (top) and experimental (bottom) intensity profiles at the focal planes of (a) z = 285 µm, (b) z = 300 µm, and (c) z = 315 µm after passing through the analyser are given by considering the Malus' law with different combinations of the transmission axes of P1 (red arrows) and P2 (blue arrows). P1⊥P2. From left to right, P1 = (a) 15°, 45°, and 75°, (b) 0°, 30°, and 60°, (c) 15°, 45°, and 75°. The white dots indicate the positions of the gaps.

The designed metadevice is realized by a geometric metasurface, which can produce PB phase profiles, indicating that the metadevice has broadband performance but with inevitable chromatic aberration. Here, we test the broadband performance of the metadevice that can generate the 3D knot focal curve. Figure 3.14a shows the experimental results of the 3D knot focal curve (2D perspective view) at different incident wavelengths and the same observation plane z = 300 μm. A clear focal curve is observed under the incidence of 650 nm, while the image is gradually blurred when the incident wavelength deviates from the designed wavelength, which is due to chromatic aberration. In order to obtain the clear 3D knot focal curve images at other wavelengths, we need to adjust the position of the objective lens along the light propagation direction to change the observation plane, indicating the existence of chromatic aberration. Figure 3.14b shows the experimental results of the clear images, with the image quality slightly deteriorating at other wavelengths. The observation plane is shifted towards (or away from) the metadevice when the wavelength increases (or decreases). We also test the polarization distribution of the 3D knot focal curve at other incident wavelengths. Figure 3.14c shows the experimental results at 500 nm, 550 nm, and 650 nm, which indirectly confirm the generated polarization profiles.

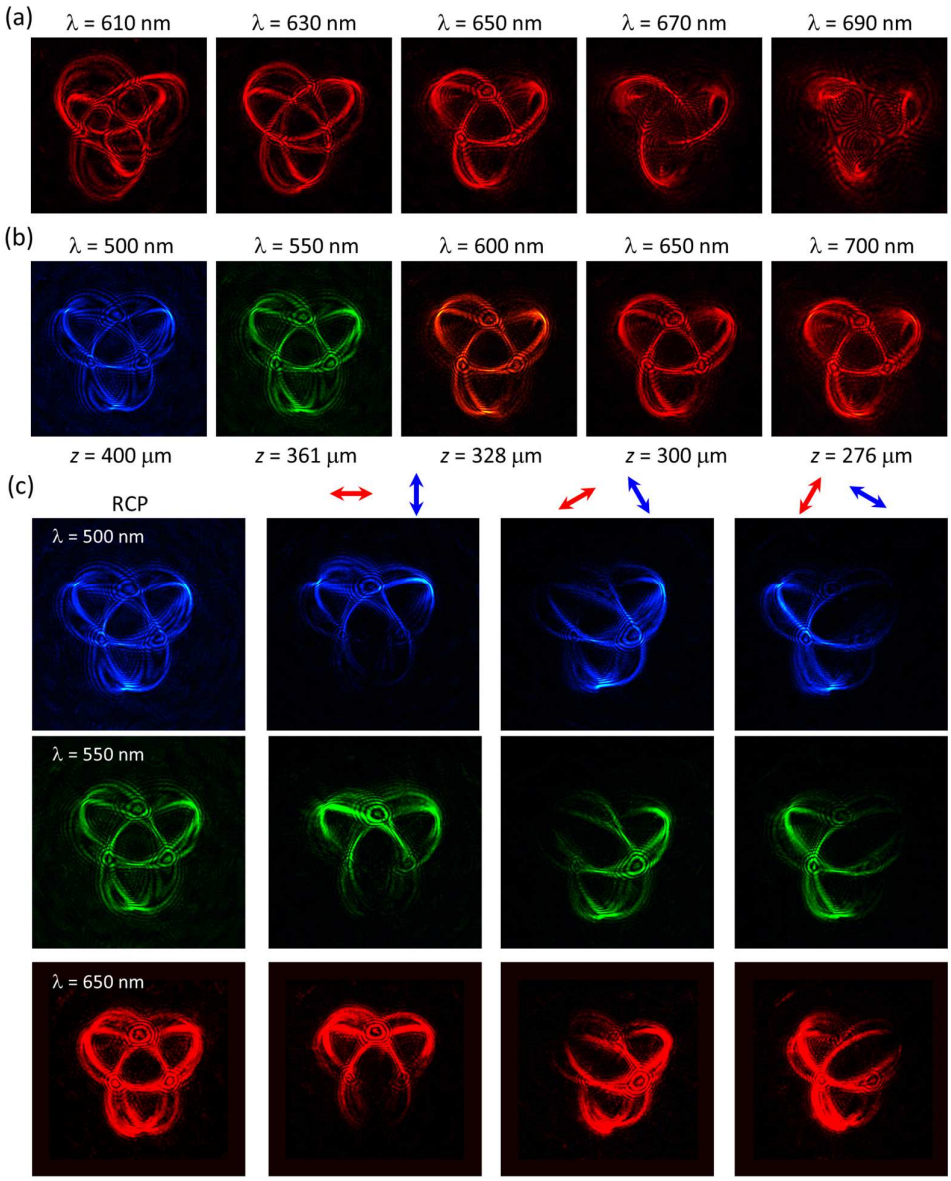

Figure 3.14 (a) Incident wavelengths range from 610 nm to 690 nm at a fixed observation plane (z = 300 μm). (b) Clear images at various wavelengths (500 nm – 700 nm) are obtained by changing the observation planes. (c) Experimental results of the intensity distributions for polarization distribution detection at different wavelengths (z = 300 μm).

3.4.2. Multiple 3D Polarization Knots

To show the robustness of our proposed concept, we also develop a metadevice that can simultaneously create five 3D polarization knots at a single operating wavelength. The coordinates of each point on the 3D knots are given by the following parametric equations,

$$\begin{cases} u_{m,n} = a\left(\sin\phi_{m,n} + 2\sin\left[(1+m)\phi_{m,n}\right]\right) + r\cos\Lambda_m \\ v_{m,n} = a\left(\cos\phi_{m,n} - 2\cos\left[(1+m)\phi_{m,n}\right]\right) + r\sin\Lambda_m \\ f_{m,n} = -1.5a\sin\left[(2+m)\phi_{m,n}\right] + f_0 \end{cases} \quad (3.10)$$

Where $r\cos\Lambda_m$ and $r\sin\Lambda_m$ are the locations of the knot *m* in the *xy*-plane with a radius of *r* from the centre of a focal plane and an angle of Λ_m w.r.t. the *x*-axis (Figure 3.15a). *a* is a constant number used to define the knot dimensions. The polarization direction $\phi_{m,n}$ of any point *n* on the knot *m* is denoted with a yellow arrow. The 3D knots extend into the *z*-direction and the plane $z = f_0$ is the middle observation plane of the knots.

In this design, the 3D polarization structures are the knot 1 (a 3-foil knot; $m = 1$, ϕ varies from 0 to 2π), knot 2 (a 4-foil knot; $m = 2$, ϕ varies from 0 to 2π), knot 3 (a 3-foil knot; $m = 1$, ϕ varies from π/4 to 9π/4), knot 4 (a 4-foil knot; $m = 2$, ϕ varies from π/4 to 9π/4), and knot 5 (a 5-foil knot; $m = 3$, ϕ varies from 0 to 2π). The parameter *a* is defined as 10 μm, f_0 is 500 μm and *r* is 70 μm. The orientation angles Λ_m of the knots are respectively 0°, 90°, 180°, 270° for the knot 1, 2, 3, and 4, while the knot 5 is designed to be on-axis propagation (see Figure 3.15a). In order to maintain the same distance between two adjacent points for different knots, the knots are designed to have different numbers of the total points *N*, which are 2000, 2860, and 3728 points for the knot 1 and 3, 2 and 4, and 5, respectively. Their polarization profiles are represented as yellow arrows. The metadevice is designed to generate five 3D polarization knots at a single operation wavelength of 650 nm on the same observation region.

By substituting the coordinates (u_n, v_n, f_n) in Equation 3.10 to Equation 3.1, then the phase profile of the designed metadevice with a diameter of 360 μm can be calculated by using Equation 3.4 as shown in Figure 3.16a and its corresponding SEM image is shown in Figure 3.16b. At this moment, the developed metadevice is ready to characterise.

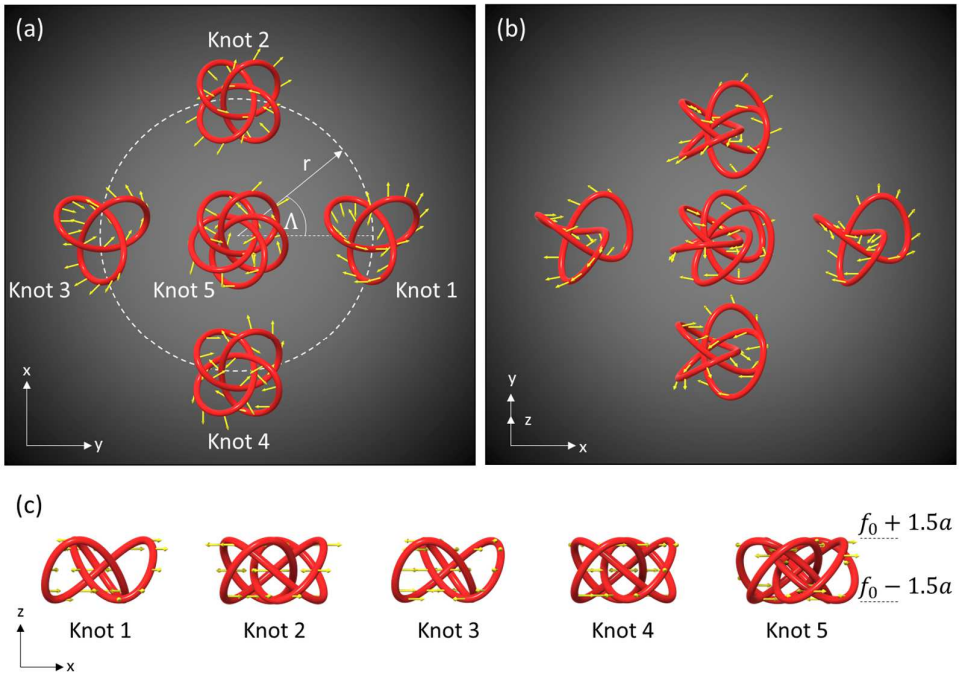

Figure 3.15 (a) An orientation of the 3D knots with a predesigned polarization profile (yellow arrows) in the *xy*-plane. (b) The perspective of the 3D knots. (c) An individual 3D knot in the *xz*-plane.

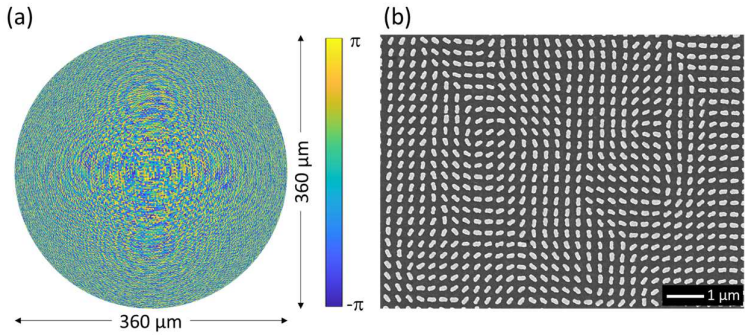

Figure 3.16 (a) The phase profile and (b) SEM image of the metadevice to generate the multiple 3D polarization knots.

Figure 3.17 shows the simulation and experimental results of the created five 3D polarization knots for a single operating wavelength of 650 nm at three observation planes (z = 485 µm, 500 µm, and 515 µm). With the incident LP light beam, the gaps can be found on those three observation planes when the transmission axes of the P1 and P2 are (45°, 135°), (0°, 90°), and (75°, 165°), respectively (Figure 3.17b). The experimental results are in good agreement with the simulated results.

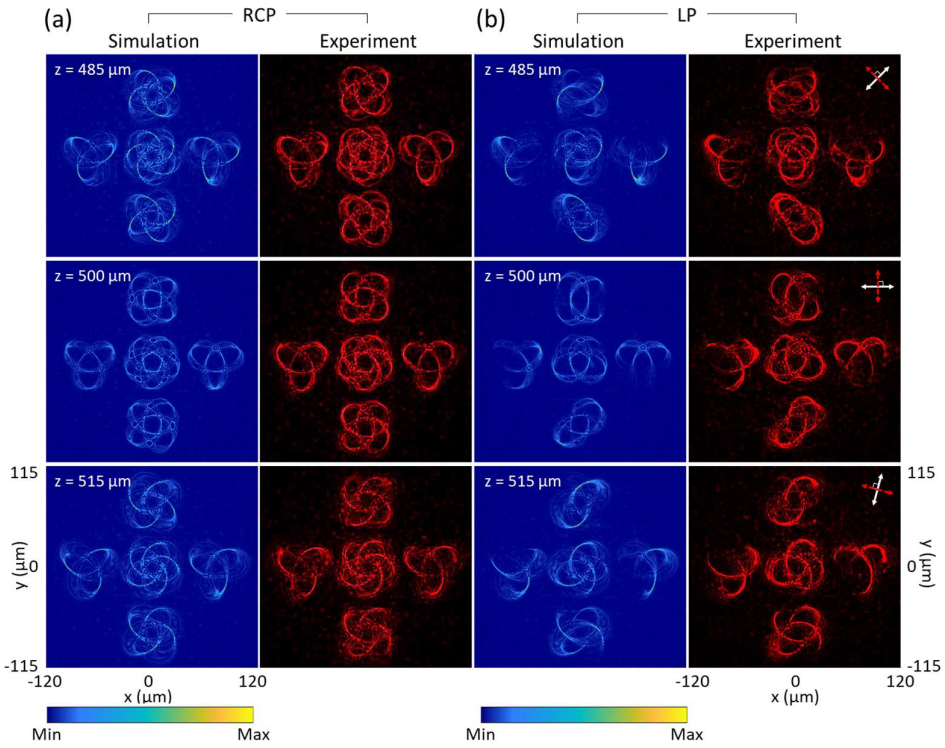

Figure 3.17 Simulation and experimental results of the generated multiple 3D polarization knots at $\lambda = 650$ nm. (a) The intensity distributions at different observation planes under the illumination of the RCP light beam. (b) The intensity distributions under the illumination of an LP light beam for polarization distribution detection with different transmission axes of the linear polarizer and the analyser at different observation planes. The simulated (left) and measured intensity profiles (right) at three observation planes after passing through the analyser by considering the Malus' law with different combinations of the transmission axes of the polarizer and the analyser. The white and red double arrows indicate the transmission axes of the first polarizer (P1) and the analyser (P2), respectively. P1⊥P2. The direction of the white arrows: 45° (z = 485 μm), 0° (z = 500 μm), and 75° (z = 515 μm) w.r.t. the x-axis.

3.4.3. Colour-Selective 3D Polarization Knots

The colour selective functionality of the designed metadevice is inspired by the broadband response of a gold nanorod and the dispersion effect of a metalens, whose focal length varies with the wavelengths. Figure 3.18 shows the schematic of our proposed metadevice for the generation of multiple 3D polarization structures. The metadevice consists of gold nanorods with spatially variant orientations sitting on a glass substrate. Upon the illumination of an LP beam, multiple 3D knots with predesigned polarization profiles are created. At a given observation region of interest, only a single 3D knot can be obtained for a single colour (wavelength). Different 3D polarization knots can be obtained by changing the incident wavelengths (Figure 3.18a-3.18f). The generated polarization structures are unveiled after passing through a linear polarizer, leading to various modulated intensity patterns captured by a CCD camera as depicted in Figure 3.18d-3.18f.

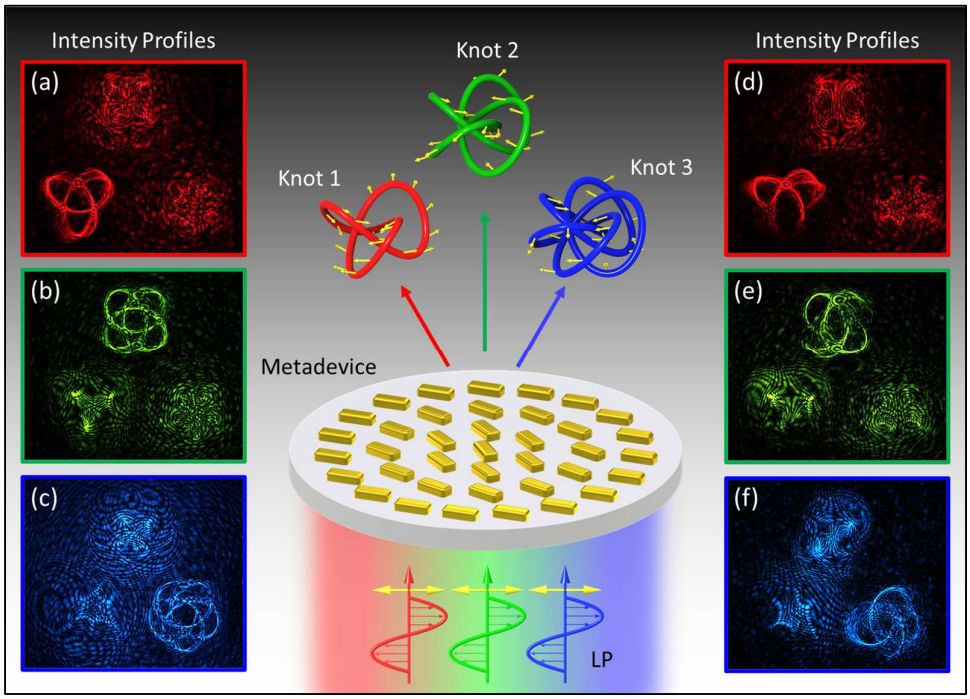

Figure 3.18 Schematic of the metasurface device for generating colour selective 3D polarization structures. Here, a 3-foil knot (knot 1), a 4-foil knot (knot 2), and a 5-foil knot (knot 3) are selected as complex polarization structures. The knot 1, 2, and 3 are predesigned polarization structures in the same observation region for the wavelengths of 650, 575, and 500 nm, respectively. The polarization directions of points on the 3D knots are denoted with the yellow arrows. Both polarization and colour information (wavelength) of these three knots are encoded into a single metasurface consisting of gold nanorods. (a)-(c) The measured intensity profiles upon the illumination of a horizontal LP light beam before and (d)-(f) after passing through a polarizer (analyser). (a) and (d) are generated at λ = 650 nm, (b) and (e) at λ = 575 nm, and (c) and (f) at λ = 500 nm in the same observation plane of z = 500 μm. The intensity profiles (d)-(f) correspond to the analyser with a transmission axis along the vertical direction

To create wavelength-multiplexed polarization profiles, the phase profile of the metadevice is given by

$$\Phi(x,y) = \arg\left\{\sum_{m=1}^{M}\sum_{n=1}^{N}\left(e^{i[\varphi(x,y)_{m,n}+\phi_{m,n}]} + e^{-i[\varphi(x,y)_{m,n}-\phi_{m,n}]}\right)\right\} \qquad (3.11)$$

where $\varphi(x,y)_{m,n} = -\frac{2\pi}{\lambda_m}\left(\sqrt{f_{m,n}^2 + \left(x-u_{m,n}\right)^2 + \left(y-v_{m,n}\right)^2} - \sqrt{f_{m,n}^2 + u_{m,n}^2 + v_{m,n}^2}\right), n$ and m represent the n^{th} focal point on the m^{th} polarization structure, λ_m is the wavelength for the m^{th} structure. N and M are the total numbers of the focal points and 3D polarization structures, respectively. $(u_{m,n}, v_{m,n}, f_{m,n})$ are the coordinates of a given point with a polarization rotation angle of $\phi_{m,n}$ on the created 3D polarization structures. This design features colour selective functionality and multiple 3D polarization structures. In a given observation region, different 3D polarization structures can be generated by controlling the operating wavelengths.

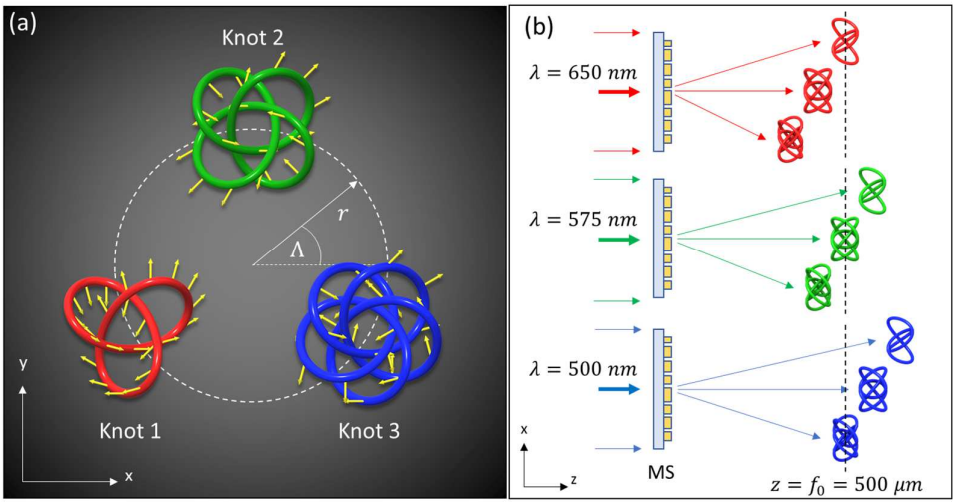

Figure 3.19 (a) The arrangement of the 3D polarization knots. The polarization direction of any given point is denoted with yellow arrows. (b) Colour selective mechanism. The locations of three different 3D knots are given upon the illumination of the incident light at λ = 650 nm (top), λ = 575 nm (middle), and λ = 500 nm (bottom), respectively. The observation region is defined by the two planes: z = 485 μm and z = 515 μm. The plane z = 500 μm is the middle plane of the observation region. Only one 3D polarization knot is obtained for a single incident wavelength, thus the colour selective functionality is realized

As a proof of concept, a 3-foil knot (knot 1, m = 1), a 4-foil knot (knot 2, m = 2), and a 5-foil knot (knot 3, m = 3) are selected as the polarization knots and the arrangements are shown in Figure 3.19a. The coordinates of each point on the 3D knots are also given by the parametric equations from Equation 3.10. In the design, a is defined as 10 μm, f_0 is 500 μm and r is 50 μm. The orientation angles Λ_m of the knots are 210°, 90°, and -30° for m = 1, 2, and 3, respectively. The polarization rotation angles of the points on each knot vary from 0 to 2π. In order to maintain the same distance between two adjacent points for different knots, the knots are designed to have different numbers of the total points N, which are 2000, 2860, and 3728 points for the knot 1, 2, and 3, respectively.

In this designed metadevice, the wavelength information ($\lambda_1 = 650\,nm, \lambda_2 = 575\,nm,$ and $\lambda_3 = 500\,nm$) is added to the polarization profiles to provide the colour selective functionality. The observation region is defined as the 3D space between two planes z = 485 μm and z = 515 μm, and the middle observation plane of the 3D knot is located at z = 500 μm. When the metadevice is illuminated by LP light at λ = 650 nm (red), three polarization knots are generated, but only knot 1 is located in the observation region and the other two knots are outside this region (Figure 3.19b top). When the incident wavelength is 575 nm (green), knot 2 is located in the observation region while knot 1 and knot 3 are outside this region (Figure 3.19b middle). Similarly, only knot 3 is in the observation region at λ = 500 nm (blue) (Figure 3.19b bottom). Therefore, different

polarization structures can be obtained by controlling the wavelengths of the incident light. The calculated phase profiles of the metadevices by using Equations 3.10 and 3.11 are shown in Figure 3.20a and its corresponding SEM image is shown in Figure 3.20b. At this moment, the developed metadevice is ready to characterise.

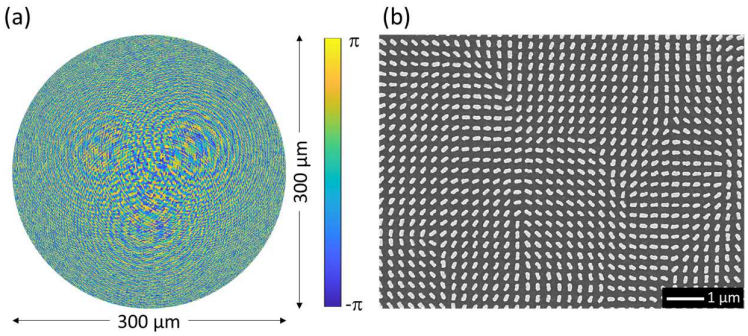

Figure 3.20 (a) The phase profile and (b) SEM image of the metadevice to generate the colour-selective 3D polarization knots.

We then characterize the metasurface for generating colour selective 3D polarization knots by changing the incident wavelengths. Figure 3.21 shows the created 3D polarization knots when the incident wavelength is 650 nm. When the polarization state of the incident beam is RCP, the knot 1 can be clearly seen from the three observation planes (i.e., z = 485, 500, and 515 µm) while the other two knots are blurred and unrecognizable (Figure 3.21a). Similar to other polarization structures with an incident LP light beam, the gaps can be seen at the positions where the predesigned polarization rotation is equal to 2α and $2\alpha+\pi$ (α is the polarization direction of the incident LP light beam w.r.t. the x-axis). Thus, the intensity gaps are found on those three observation planes when the combinations of transmission axes of the P1 and P2 are (45°, 135°), (0°, 90°), and (75°, 165°), respectively (Figure 3.21b). In Figure 3.22-3.23, knot 2 and knot 3 on the observation plane are obtained by tuning the operating wavelength to 575 nm and 500 nm, respectively.

As illustrated in Figure 3.19b, all 3D knots are generated for each operating wavelength. Here, the locations of all generated 3D knots for each operation wavelength have been studied and provided. When the metadevice is illuminated by RCP light at λ = 650 nm (red), three polarization knots are generated (Figure 3.24). The 5-foil knot can be found at the region between z = 365 and 389 µm. The 4-foil knot can be found at the region between z = 425 and 452 µm. The 3-foil knot can be found at the region between z = 485 and 515 µm. When the metadevice is illuminated by RCP light at λ = 575 nm (green) (Figure

3.25). The 5-foil knot can be found in the region between z = 418 and 444 μm. The 4-foil knot can be found in the region between z = 485 and 515 μm. The 3-foil knot can be found in the region between z = 552 and 586 μm. When the metadevice is illuminated by RCP light at λ = 500 nm (blue) (Figure 3.26). The 5-foil knot can be found in the region between z = 485 and 515 μm. The 4-foil knot can be found in the region between z = 562 and 596 μm. The 3-foil knot can be found in the region between z = 638 and 677 μm. The experimental results unambiguously show that the metadevice can generate the 3D polarization knots as predicted by the theoretical analysis.

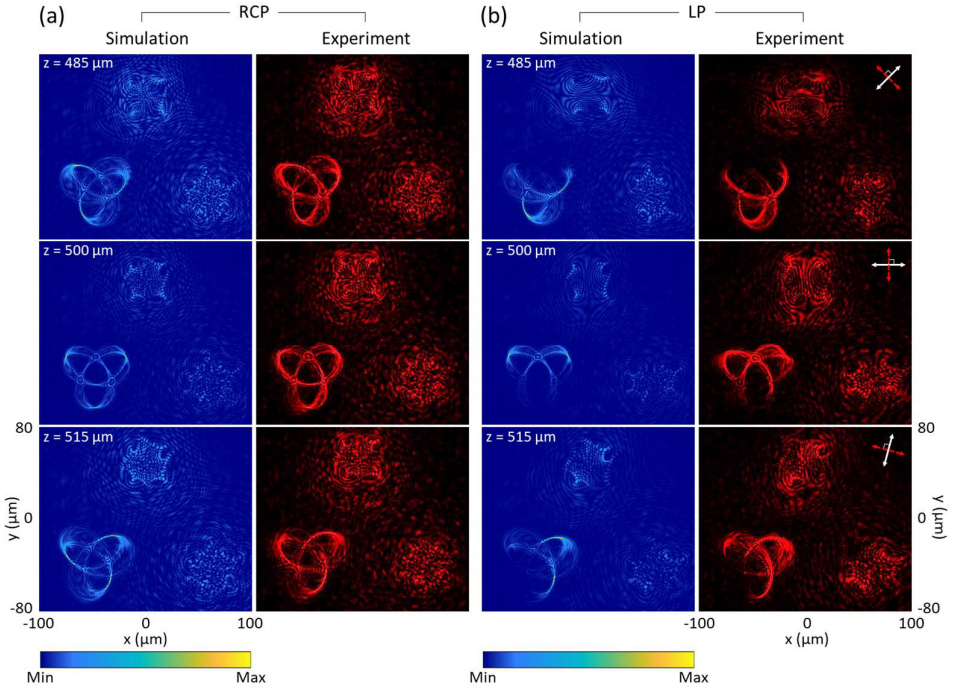

Figure 3.21 Simulation and experimental results of the selected 3D polarization knots at λ = 650 nm. (a) The intensity distributions at different observation planes upon the illumination of RCP light. (b) The intensity distributions at different observation planes upon the illumination of an LP light beam for polarization distribution detection with different combinations of transmission axes of the linear polarizer and the analyser. The direction of the white arrows: 45° (z = 485 μm), 0° (z = 500 μm), and 75° (z = 515 μm) w.r.t. the x-axis.

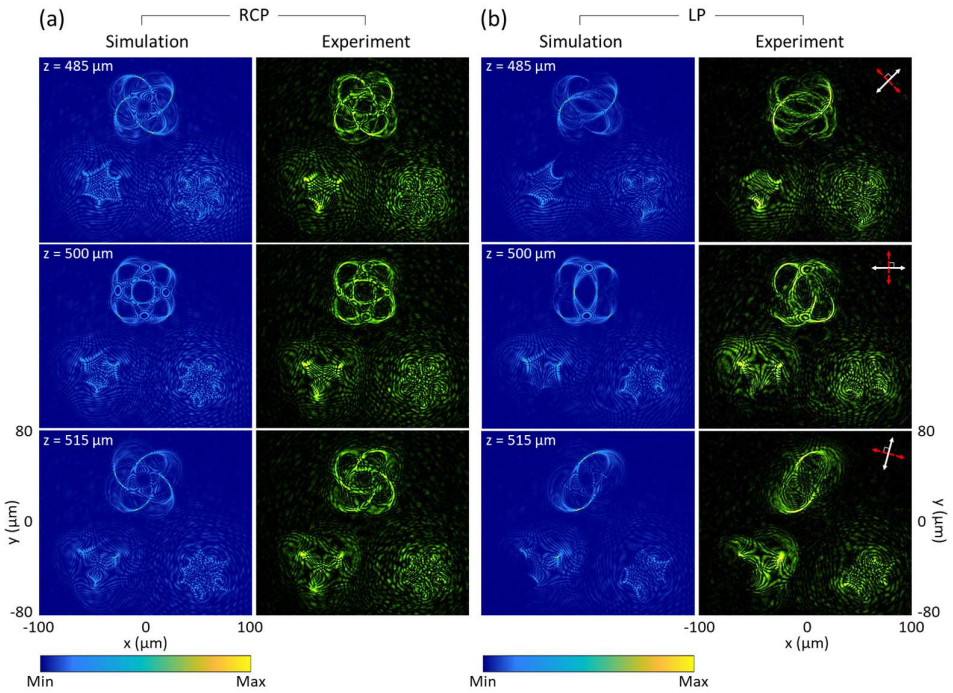

Figure 3.22 Simulation and experimental results of the selected 3D polarization knots at λ = 575 nm. (a) The intensity distributions at different observation planes upon the illumination of RCP light. (b) Polarization structure detection with the same detection method as that in Figure 3.21b.

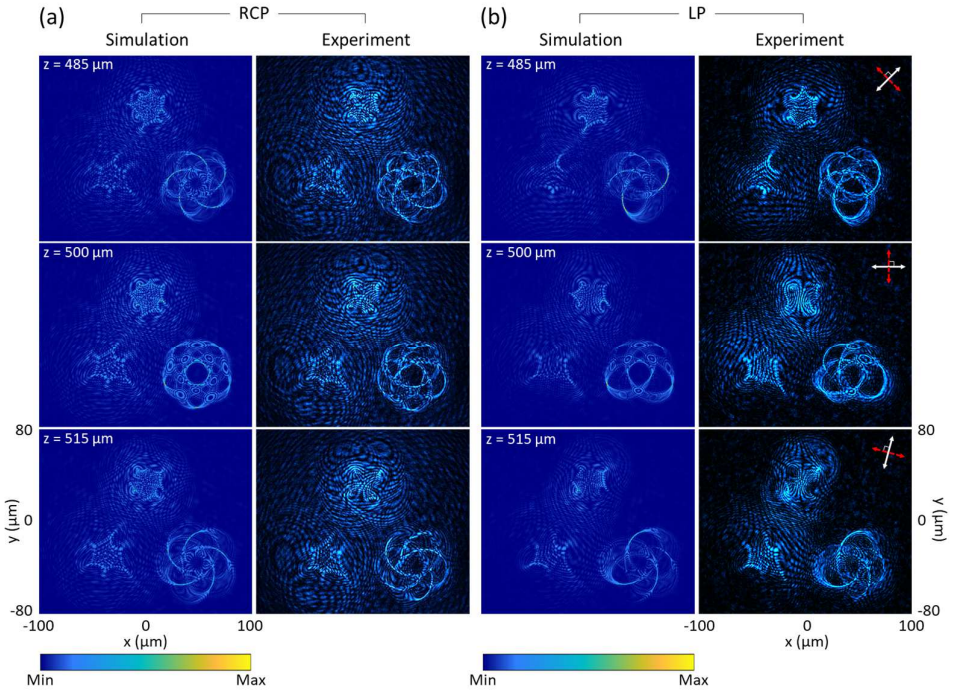

Figure 3.23 Simulation and experimental results of the selected 3D polarization knots at λ = 500 nm. (a) The intensity distribution at different observation planes upon the illumination of RCP light. (b) Polarization structure detection with different combinations of transmission axes of the first polarizer and the second polarizer.

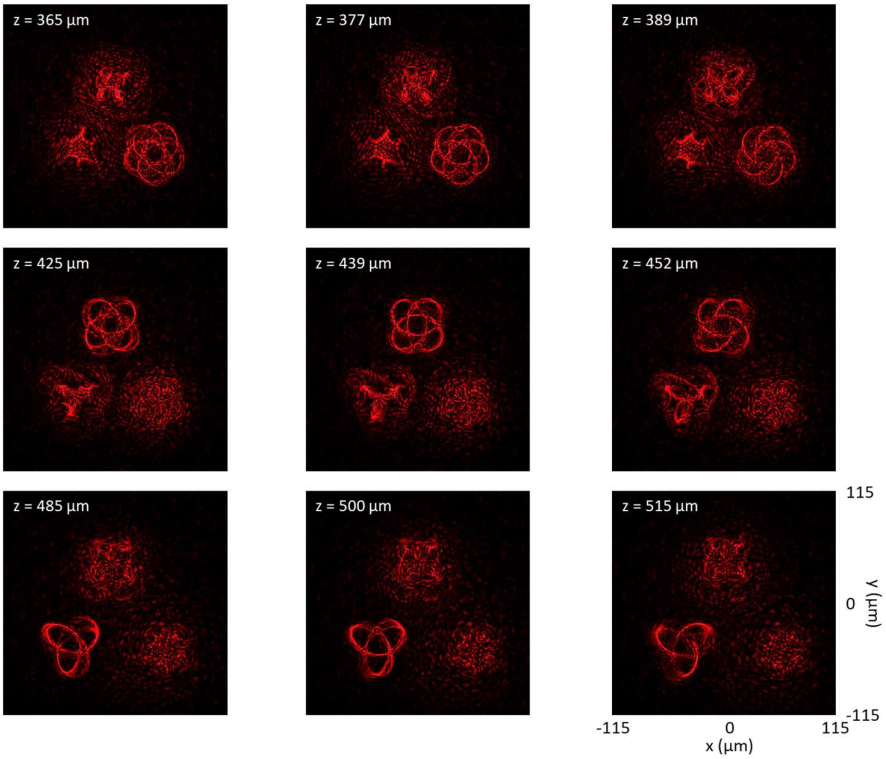

Figure 3.24 Locations of the created 3D knots upon the illumination of $\lambda = 650$ nm.

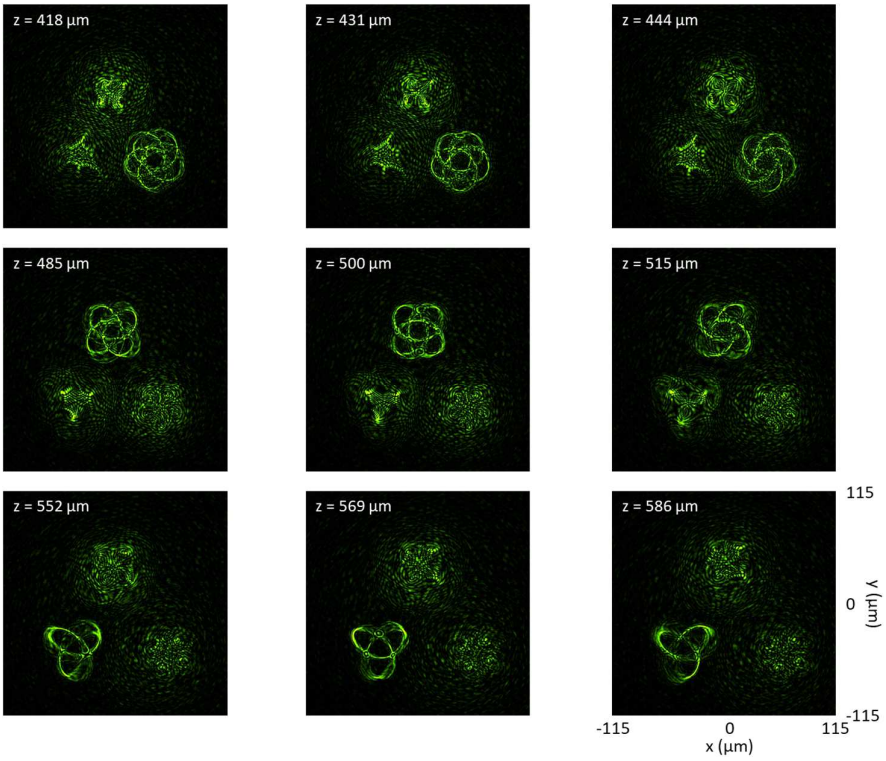

Figure 3.25 Locations of the created 3D knots upon the illumination of $\lambda = 575$ nm.

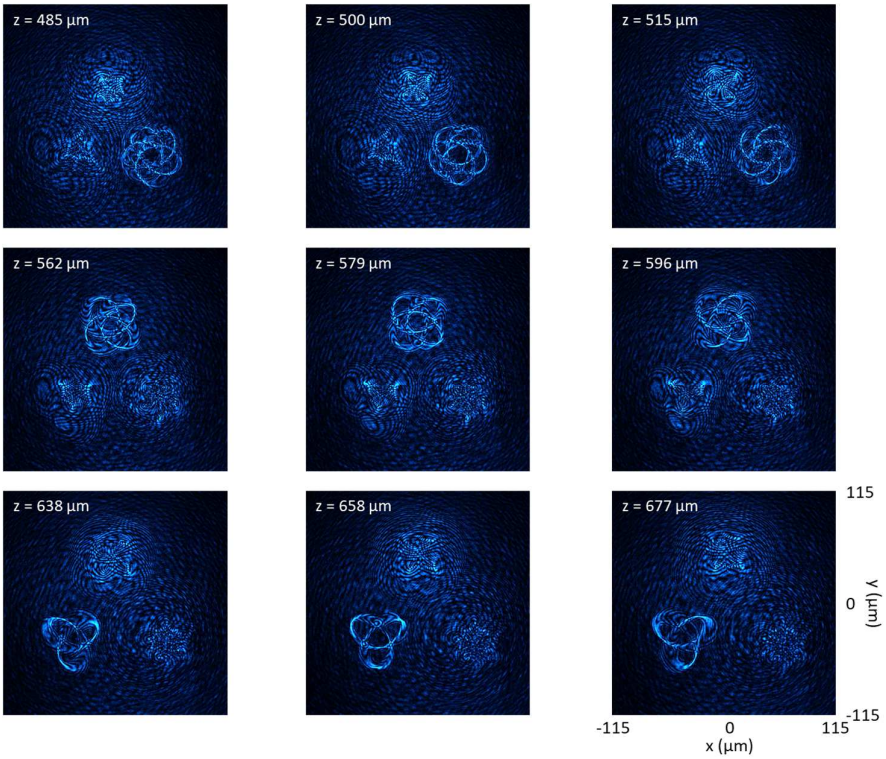

Figure 3.26 Locations of the created 3D knots upon the illumination of λ = 650 nm.

3.5. Wavelength-Selective Digital Numbers

Following the wavelength/colour multiplexing functionality described by Equation 3.10, here we experimentally demonstrate the 10-wavelength multiplexing to create the seven-segment digital numbers ranging from 0 to 9 in a 2D space. Figure 3.27 shows the operating wavelengths spanning the 500-680 nm range generated by a Supercontinuum laser source are used to choose the desired display number on the observation plane. Each wavelength corresponds to an individual digital number, which consists of 7 segments. With a wavelength step size of 20 nm, the numbers with predesigned polarization profiles ranging from 0 to 9 are created on the focal plane. Each number includes seven focal lines with linear polarization states along the vertical or horizontal directions. The ON and OFF states of the focal lines are controlled by the predesigned polarization rotation with an angle of 90° and 0°, respectively. Without an analyser, all segments (focal lines) appear simultaneously. The desired number can be revealed with the aid of an analyser. Due to the low conversion efficiency of a plasmonic metasurface, the convolutional neural network is used to identify the displayed number on the observation plane, which can improve the performance of our approach for the applications such as optical security and optical communications.

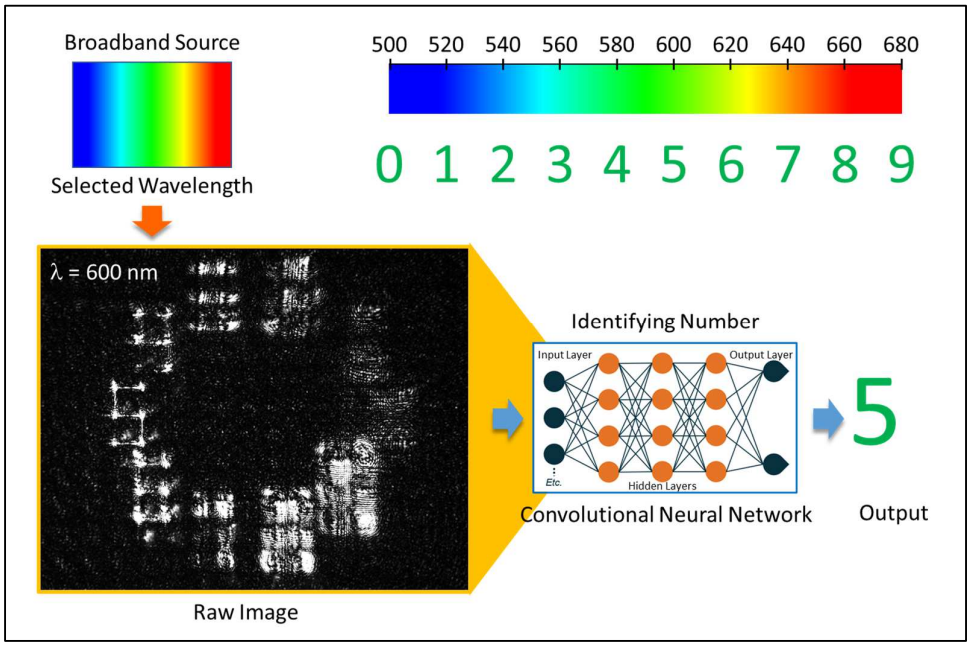

Figure 3.27 Schematic of the proposed method for wavelength selective digital numbers with a metadevice and the deep learning approach for identifying the correct display numbers on the observation plane.

To create wavelength-multiplexed polarization profiles in a 2D space, the phase profile of the metadevice is given by

$$\Phi(x,y) = \arg\left\{\sum_{m=1}^{M}\sum_{q=1}^{Q}\sum_{n=1}^{N}\left(e^{i[\varphi(x,y)_{m,q,n}+\phi_{m,q,n}]} + e^{-i[\varphi(x,y)_{m,q,n}-\phi_{m,q,n}]}\right)\right\} \quad (3.12)$$

where

$$\varphi(x,y)_{m,q,n} = -\frac{2\pi}{\lambda_m}\left(\sqrt{f_{m,q,n}^2 + \left(x-u_{m,q,n}\right)^2 + \left(y-v_{m,q,n}\right)^2} - \sqrt{f_{m,q,n}^2 + u_{m,q,n}^2 + v_{m,q,n}^2}\right)$$

, n, q, and m represent the n^{th} focal point, the q^{th} focal line and the m^{th} digital number, respectively. λ_m is the wavelength for the m^{th} digital number. N, Q, and M are the total numbers of the focal points, focal lines, and digital numbers, respectively. $(u_{m,q,n}, v_{m,q,n}, f_{m,q,n})$ are the coordinates of a given point with a polarization rotation angle of $\phi_{m,q,n}$ on the created display numbers.

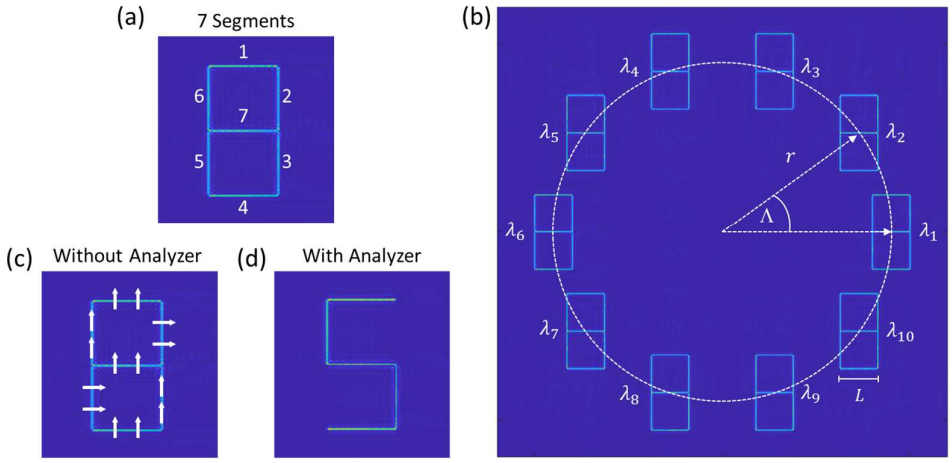

Figure 3.28 (a) A digital number with seven focal lines. (b) The arrangement of the digital numbers in a 2D space. (c) An example of the predesigned polarization rotation states along two different directions, which correspond to the ON and OFF states. (d) The intensity distribution of the revealed number in (c) when an analyser is used.

The 7-segment- digital numbers consist of seven focal lines with an arrangement of each line depicted in Figure 3.28a. Each segment is 20 μm long (L) and includes 200 focal spots (N = 200). The segments along vertical and horizontal directions are created with different parametric equations as follows.

For q = 1, 4, 7 (horizontally focal lines), the equation is given by

$$\begin{cases} u_{m,q,n} = \left(n \times \left(\frac{L}{N}\right)\right) - \frac{L}{2} + r\cos\Lambda_m \\ v_{m,q,n} = r\sin\Lambda_m \\ f_{m,q,n} = f_0 \end{cases} \tag{3.13}$$

For q = 2, 3, 5, 6 (vertically focal lines), the equation is given by

$$\begin{cases} u_{m,q,n} = r\cos\Lambda_m \\ v_{m,q,n} = \left(n \times \left(\frac{L}{N}\right)\right) - \frac{L}{2} + r\sin\Lambda_m \\ f_{m,q,n} = f_0 \end{cases} \tag{3.14}$$

where $r\cos\Lambda_m$ and $r\sin\Lambda_m$ are the coordinates of the digital number m in the xy-plane. r is the radius of the circle with its centre in the focal plane. Λ_m is the central angle formed between an arbitrary radius and the radius along the x-axis (Figure 3.28b). f_0 is the focal length of the lens-based metadevice.

In this design, f_0 and r are 300 μm and 90 μm, respectively. The central angles Λ_m of the numbers are respectively 0°, 36°, 72°, 108°, 144°, 180°, 216°, 252°, 288°, and 324°

(corresponding to numbers 0 to 9). The polarization rotations of each number *m* are given by

$$\text{Number '0': m = 1; } \phi_{1,q,n} = \{\frac{\pi}{2}, \frac{\pi}{2}, \frac{\pi}{2}, \frac{\pi}{2}, \frac{\pi}{2}, \frac{\pi}{2}, 0\}$$

$$\text{Number '1': m = 2; } \phi_{2,q,n} = \{0, \frac{\pi}{2}, \frac{\pi}{2}, 0, 0, 0, 0\}$$

$$\text{Number '2': m = 3; } \phi_{3,q,n} = \{\frac{\pi}{2}, \frac{\pi}{2}, 0, \frac{\pi}{2}, \frac{\pi}{2}, 0, \frac{\pi}{2}\}$$

$$\text{Number '3': m = 4; } \phi_{4,q,n} = \{\frac{\pi}{2}, \frac{\pi}{2}, \frac{\pi}{2}, \frac{\pi}{2}, 0, 0, \frac{\pi}{2}\}$$

$$\text{Number '4': m = 5; } \phi_{5,q,n} = \{0, \frac{\pi}{2}, \frac{\pi}{2}, 0, 0, \frac{\pi}{2}, \frac{\pi}{2}\}$$

$$\text{Number '5': m = 6; } \phi_{6,q,n} = \{\frac{\pi}{2}, 0, \frac{\pi}{2}, \frac{\pi}{2}, 0, \frac{\pi}{2}, \frac{\pi}{2}\}$$

$$\text{Number '6': m = 7; } \phi_{7,q,n} = \{\frac{\pi}{2}, 0, \frac{\pi}{2}, \frac{\pi}{2}, \frac{\pi}{2}, \frac{\pi}{2}, \frac{\pi}{2}\}$$

$$\text{Number '7': m = 8; } \phi_{8,q,n} = \{\frac{\pi}{2}, \frac{\pi}{2}, \frac{\pi}{2}, 0, 0, 0, 0\}$$

$$\text{Number '8': m = 9; } \phi_{9,q,n} = \{\frac{\pi}{2}, \frac{\pi}{2}, \frac{\pi}{2}, \frac{\pi}{2}, \frac{\pi}{2}, \frac{\pi}{2}, \frac{\pi}{2}\}$$

$$\text{Number '9': m = 10; } \phi_{10,q,n} = \{\frac{\pi}{2}, \frac{\pi}{2}, \frac{\pi}{2}, \frac{\pi}{2}, 0, \frac{\pi}{2}, \frac{\pi}{2}\}$$

where the values in the curly brackets represent the polarization rotation angles of $\phi_{m,1,n}, \phi_{m,2,n}, \phi_{m,3,n}, \phi_{m,4,n}, \phi_{m,5,n}, \phi_{m,6,n}$, and $\phi_{m,7,n}$, respectively. The ON and OFF states are represented by π/2 and 0, respectively. As an example of the number '5' in Figure 3.28c, the polarization angles of segments 2 and 5 are designed to be 0, while the other five segments are π/2. Under the illumination of the incident LP light, the number '5' can be revealed with the aid of an analyser with the transmission axis along the y-direction (see Figure 3.28d). The designed metadevice is realised by using a transmissive metasurface. The calculated phase profile from Equation 3.12 and its corresponding SEM image are shown in Figure 3.29.

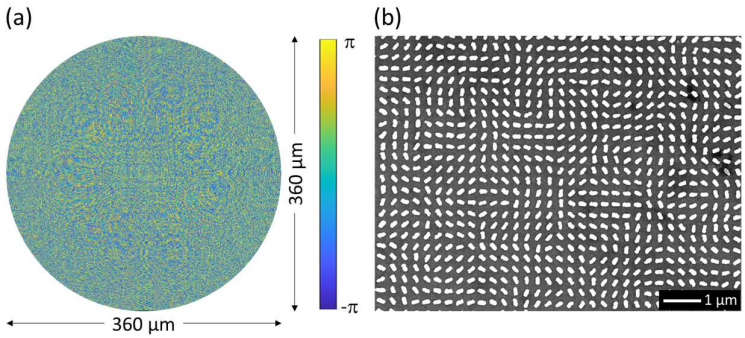

Figure 3.29 (a) The phase profile and (b) SEM image of the metadevice to generate the wavelength-selective digital numbers.

The fabricated metadevice is characterised by using the optical setup in Section 2.4.3. The laser source is controlled to vary the incident wavelengths from 500 to 680 nm with an interval of 20 nm. Under the incident RCP light, the intensity distributions of the ON and OFF states in each number are similar due to the uniform intensity. This means that all created numbers on the observation plane look like the number '8' as shown in Figure 3.30. Due to a low conversion efficiency of the developed metadevice, the power of the incident RCP beams has to be increased, causing the high intensity of the non-converted part as a background noise. The background noise cannot be completely suppressed by the two pairs of a QWP and an analyser due to the experimental error that cannot meet the requirement of angle $\beta_1 = \beta_2 = \frac{\pi}{4}$ and $\vartheta = 0$ in Section 2.4.3. The generated numbers are disturbed by the background noise, but their patterns are like the number '8' similar to the simulated results, which is acceptable for the proof of concept.

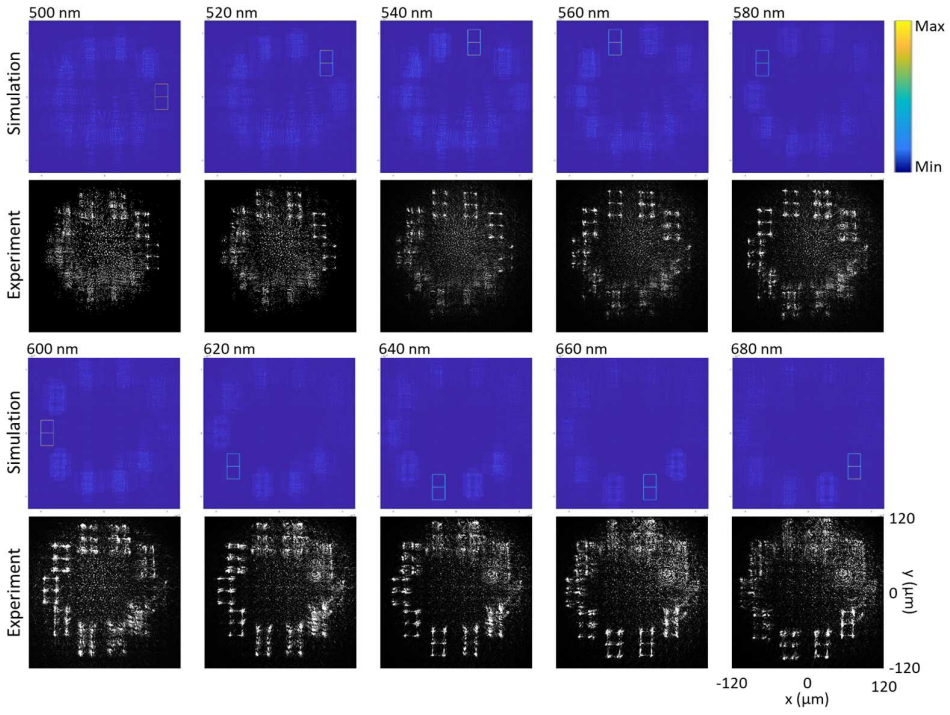

Figure 3.30 Simulation and experimental results of the intensity distribution on the observation plane under the illumination of RCP light from ten wavelengths.

With the incident LP light along the x-axis and the transmission axis of the analyser along the y-axis, only the segments that have a predesigned polarization rotation of π/2 can be observed (Figure 3.31a). Due to the low conversion efficiency of the fabricated metadevice across the visible region, there is background noise arising from the non-

converted part, which disturbs the number visibility when the intensity of the incident light is increased.

To increase perception capability and automatically recognise the numbers, we introduce a built-in deep learning approach in MATLAB to identify the revealed numbers (the generated number when the incident light is LP as shown in Figure 3.31a) on the observation plane. The learning approach is based on a convolutional neural network (CNN), which learns directly from data rather than extracted features. CNNs are supervised learning so that inputs and correct outputs are needed for training. The CNNs are particularly useful for the recognition of objects, faces, and scenes in images [92]. The typical configuration of the CNNs includes an input layer, an output layer, and many hidden layers between those input and output layers. In this design, totally 7 layers with the built-in functions in MATLAB are used for training and validating the dataset as follows.

1. ImageInputLayer function is used to receive images to a network and apply data normalisation.

2. Convolution2DLayer function is used to apply sliding filters to the input. The filters are moved along vertical and horizontal directions to calculate the dot product of the weights and the input data, and then add a bias term.

3. BatchNormalizationLayer function is used to speed up a training process and increase the stability of the layers through the network. A batch normalization layer normalizes each input channel across a mini-batch (a consecutive subset of the dataset). The layer first normalizes the activations of each channel by subtracting the mini-batch mean and dividing by the mini-batch standard deviation. Then, the layer shifts the input by a learnable offset β and scales it by a learnable scale factor γ. The learnable parameters β and γ are updated during network training.

4. ReLULayer function performs a threshold operation by setting the value of each element of the input to zero when the value is a negative value.

5. FullyConnectedLayer function is performed by multiplying the input data with a weight matrix and then adding the result with a bias vector.

6. SoftmaxLayer function is a transfer function used to apply a softmax function to the input. The function is described by softmax(n) = exp(n)/sum(exp(n)), where n is an input element.

7. ClassificationOutputLayer function uses the results from the softmax function to classify the input images to the correct classes that have been provided in the training process, i.e., number 0 to 9.

In this case, 20 captured images of each incident wavelength are used for training. Other 20 captured images are used for validation and 100% accuracy has been found. We further evaluate the performance of the learning method by developing an application programme embedded with the trained data set to recognise the revealed numbers in real-time (Figure 3.31b). The captured images for different wavelengths have their own unique patterns. In other words, the focused number, blurred numbers as well as the background noise on the observation plane of each image make the captured images different from each other. This difference provides an advantage for the CNN to identify the generated number correctly. As a result, the generated numbers are 100% correctly identified in the real-time recognition when the incident wavelength is either sequentially or randomly changed between 500 and 680 nm. The displacement of the optical elements in the setup and the incident power of the laser are two factors that affect the identification accuracy. In the event of displacement of the optical elements, the generated numbers have to be acquired and trained with the CNN again. If the power of the laser is dropped or increased by 50%, the accuracy can be reduced to 80%. This performance has been artificial investigated by increasing and decreasing the brightness of the captured images by 50% and then used them as the validation samples. Here, we have experimentally demonstrated the metadevice to create the different sets of seven focal lines with predesigned polarization rotations for ten incident wavelengths. An analyser is used to reveal the corresponding displayed number for each wavelength, which can be automatically recognised with a deep learning approach. Our method here provides a two-level security system in optical communication.

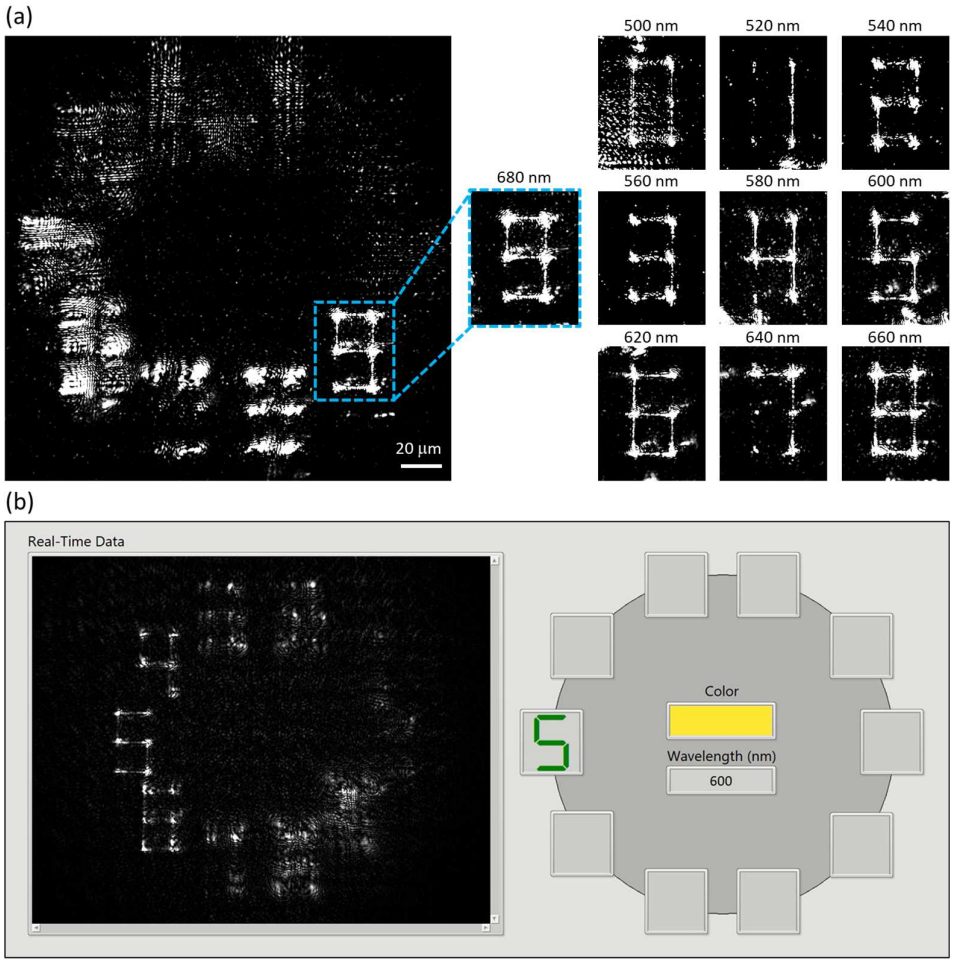

Figure 3.31 (a) The intensity distributions on the observation plane under the illumination of LP light with ten wavelengths. (b) The developed application programme for real-time recognition of the numbers on the observation plane.

3.6. Nonlinear Polarization Profile

Nonlinear optical processes, such as second, third, and high harmonic generation, and broadband optical frequency mixers are extensively investigated by using both plasmonic and dielectric metasurfaces. A nonlinear optical metasurface has been demonstrated to locally manipulate the polarization states of the second harmonic wave and encode a high-resolution image in the polarization profile accordingly as an illustration in Figure 3.32. To encrypt image information into nonlinear optical devices, the nonlinear plasmonic meta-atoms with threefold rotational (C3) symmetry have been utilized to construct the nonlinear metasurface (Figure 3.33a). The *C*3 30-nm-gold meta-atoms sit on an indium tin oxide (ITO) glass, with an ITO thickness of approximately 20 nm. The width and length of each arm of the *C*3 meta-atom are 80 and 180 nm, respectively. Each pixel is a 500×500 nm^2 square cell with the *C*3 meta-atom at the centre. Two images comprising

201×201 pixels are eventually embedded into two small metasurfaces of 100×100 μm^2, where the orientation angles of the meta-atom are $\delta = \left(\cos^{-1}\sqrt{I_{img}/I_{max}}\right)/3$. For a meta-atom with m-fold rotational symmetry, upon illumination along its rotational axis by circularly polarized fundamental waves, the allowed orders of nonlinear harmonic generation are restricted by the selection rule to $n = lm \pm 1$, where l is an integer and the "+" and "–" signs indicate that the harmonic waves and the fundamental waves (FWs) possess the same and opposite spin states, respectively. Therefore, the C3 meta-atom can selectively produce a second harmonic wave with opposite handedness to that of the incident circularly polarized FW. Regarding the selection rule, the C3 meta-atom can produce second and fourth harmonics. But the fourth harmonic has not considered due to the very low conversion efficiency [62]. More significantly, the nonlinear polarizability of the meta-atoms can be continuously manipulated by varying their orientations. As a result, a nonlinear geometric phase, $-3\sigma\delta$, is simultaneously imparted to the second harmonic wave, where σ = ±1 is the handedness of the incident FW and δ is the angle by which the C3 meta-atom is rotated with respect to the laboratory frame. By using this characteristic, image information can be encrypted into a polarization profile of the second harmonic waves. With such an encoding process, one can effectively control the polarization states of the second harmonic wave in the transverse plane. Using a linear polarizer P2 in Figure 3.33b, the polarization profile can be converted into an intensity profile, which allows for easier observation (see Figure 3.34).

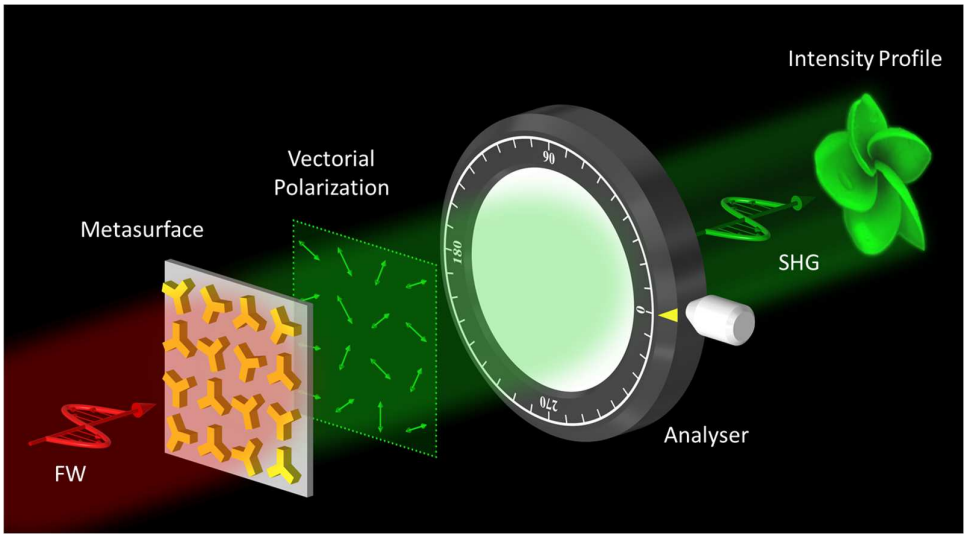

Figure 3.32 Schematic illustration of a nonlinear optical process to generate a polarization profile of the second harmonic wave, by using a nonlinear photonic metasurface. A linear polarizer acts as an analyser to convert the polarization profile into a grayscale image. FW: Fundamental wave, SHG: Second-harmonic generation.

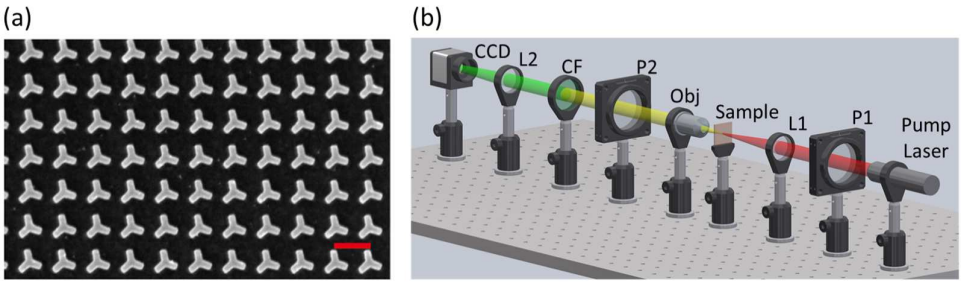

Figure 3.33 (a) SEM image of the metadevice for encoding an image of a flower. (b) Schematic of the experimental setup. P: Linear polarizer, L: Lens, Obj: Objective lens, CF: Colour filter (short-pass filter), CCD: Camera. Scalebar is 500 nm. The working principle of the experiment is the same as described in Section 2.4.3, where the QWP1 and QWP2 are removed. The CF is used to filter out the FW. The laser provides 15 mW at λ=1225 nm.

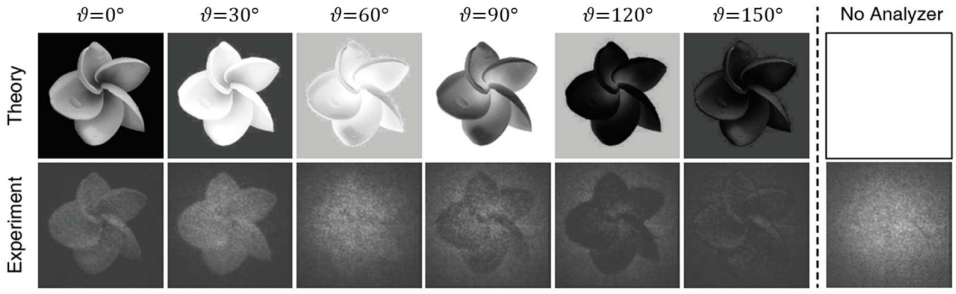

Figure 3.34 Simulation and experimental results of a nonlinear metadevice for encoding a flower into the polarization profile of the second harmonic wave. The pumping wavelength is 1250 nm. ϑ is the angle of the transmission axis of the analyser w.r.t. the x-axis. The last column shows the results when the analyser (P2 in Figure 3.33b) is absent in the experimental setup.

3.7. Summary

In this chapter, we have experimentally demonstrated the developed metadevices that can realize arbitrary focal curves in 2D and 3D spaces with customized polarization profiles without the aid of additional optical elements. A number of focal curves ranging from a simple ring to a more complicated colour-selective 3D knot are observed in the focal region of the metadevices. we used a metasurface with gold nanorods with a low conversion efficiency, which can be dramatically increased by using dielectric metasurfaces [93, 94]. Our design method can combine the colour information and 3D polarization manipulation in a single device, offering more degree of freedom for polarization engineering and enabling the realization of wavelength-selective functionality. Furthermore, we have also demonstrated the nonlinear metadevice to manipulate a polarization profile in 2D space. The unique properties of the developed metasurface devices may promote both fundamental research (e.g., complex 3D polarization structure) and practical applications (e.g., virtual reality and anti-counterfeiting). Furthermore, the developed metasurface devices can be vertically

integrated to build a complex system composed of various planar components (e.g., gratings, splitters) to perform sophisticated tasks. We expect that this capability will fuel the continuous progress of wearable and portable consumer electronics and optics where low-cost and miniaturized systems are in high demand.

CHAPTER 4 – POLARIZATION DETECTION WITH METASURFACES

In the last chapter, polarization generation and manipulation in 2D and 3D spaces have been experimentally demonstrated. Since the geometric metasurfaces are polarization-sensitive devices. In this chapter, the different methods with optical metasurfaces are used to detect the polarization states of light, including hybrid holography, light's OAM, and optical ring vortex beams. Work presented in Section 4.2 that I have contributed in both simulation and experimental parts has already been published in Advanced Photonics Research 2021 [95]. Section 4.3 and 4.4 have already been published in Advanced Optical Materials 2020 [96], Laser & Photonics Reviews 2020 [97], and Advanced Materials 2022 [98], where my main contributions include sample fabrication, experimental setup, sample characterisation, and data analysis.

4.1. Background

Polarization detection has been used for a wide variety of applications. Based on the measurement and interpretation of the polarization of light waves, polarimetry has been applied in many areas of science and technology [99], ranging from ellipsometry [100, 101], remote sensing [102] to polarization light scattering [103] and ophthalmic polarimetry [104]. For example, in defence and security, polarization information can be used to pick out artificial materials against natural surfaces. In atmospheric monitoring, it can be used to track the size and distribution of particles in the atmosphere, which can be used to monitor air quality. To measure the polarization state of a light beam, many polarization elements (e.g., polarizers, waveplates, polarization modulators) are usually employed and placed in a beam of light in front of a power meter. The traditional measurement systems have advantages in measuring speed and accuracy, but their applications are still limited due to the various polarization elements and complicated data processing systems adopted, leading to a large volume and high cost. The metasurface approach differs from previous approaches in that the phase change occurs abruptly at the interface rather than slowly evolving in, for example, a birefringent material commonly used in bulky polarization optics. Consequently, this can lead to further miniaturization and a greater potential for system integration. The ultrathin circular polarizers [105-107] and polarization rotators [108, 109] based on metamaterials have been developed recently. As planar metamaterials, metasurfaces [10, 110, 111] do not require complicated

3D nanofabrication techniques but can convert the linearly polarized incident light to its cross-polarization [73], or convert a circularly polarized light to its opposite handedness [11, 23, 112-114]. Metasurfaces have been used in circular polarization detection [16, 17, 115-118], full polarization measurement [18, 32, 119-127] and polarimetric imaging [19, 28, 31, 128]. Here, in this chapter, we experimentally demonstrate ultrathin devices to detect polarization states of light by means of hybrid holograms, light's orbital angular momentum, and optical ring vortex beams. The impact of these ultrathin devices may be substantial in a variety of fields, including encryption, imaging, optical communications, quantum science, and fundamental physics.

4.2. Polarization Detection with a Hybrid Hologram

4.2.1. Design and method

A light beam can be polarized into different polarization states such as linear, elliptical, and circular polarization states. These states of polarization are mainly determined by two parameters: handedness and ellipticity. Since geometric metasurface-based holograms are polarization-sensitive devices. In this work, we propose and experimentally demonstrate a hologram approach for measuring the polarization state of a light beam.

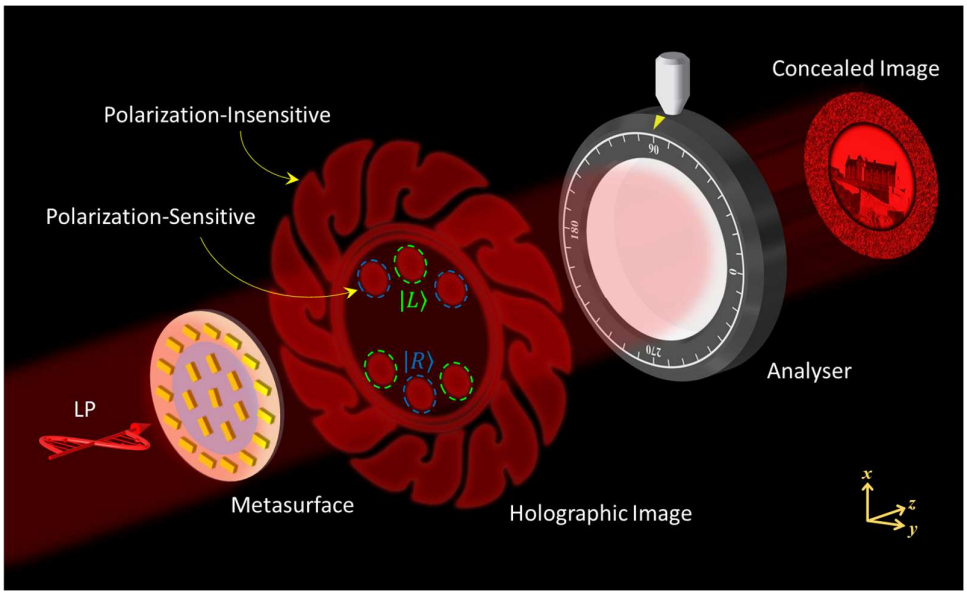

Figure 4.1 Illustration of the proposed multifunctional metasurface device. The metadevice is based on a transmissive plasmonic metasurface, which combines the functionalities of polarization-sensitive and polarization-insensitive holograms, and a spatially variant polarization profile onto a single metasurface. $|L\rangle$ is LCP. $|R\rangle$ is RCP. A linear polarizer (analyser) whose transmission axis is perpendicular to the polarization direction of the LP incident light beam.

Figure 4.1 illustrates the proposed multifunctional metasurface device. The metadevice combines the functionalities of polarization-sensitive and polarization-insensitive holograms, and a spatially variant polarization profile onto a single metasurface. By controlling the helicity and ellipticity of the incident light beam, the functionality of a polarization-sensitive hologram can enable the generation of holographic images consisting of six circular dots with various intensities. The three dots (green-dash-circle marks) correspond to the incident LCP light, while the other three dots (blue-dash-circle marks) correspond to the incident RCP light. The polarization-insensitive hologram, in contrast, can reconstruct the polarization-independent holographic Chakkar image due to its centrosymmetric shape. Those holographic images can be observed with the naked eye since the image size is proportional to the distance between the metadevice and the screen. Under the illumination of the LP light beam, the device can be used to encode a high-resolution grayscale image into the polarization profile of the transmitted light beam. The concealed image in the polarization profile can be revealed by filtering out the non-converted beam by using a linear polarizer (analyser) whose transmission axis is perpendicular to the polarization direction of the linearly polarized incident light beam.

The uniqueness of this design is that we combine both polarization-sensitive and insensitive holograms, and image concealment into a single metadevice. The projection parameters of the metadevice are depicted in Figure 4.2a. The holographic image is designed to have a full projection angle of 30° along both horizontal (Θ_h) and vertical (Θ_v) directions, while the hidden image is encoded in the polarization profile of the light beam along the optical axis, which is realized based on the superposition of two different phase profiles for circular polarization states with opposite handedness. To generate a holographic image, the Gerchberg-Saxton (GS) algorithm is used to calculate a phase profile of a hologram via a propagating function [129]. The amplitudes of the sampled incident beam profile and the intensity distribution of target image at the diffraction plane are used as the input data to the algorithm. The amplitude can be calculated by taking the square roots of the intensities. At the beginning, a random number between -π to π is used to generate an initial array of phases and the array is then multiplied by the respective sampled amplitudes of the incident beam. After that, the Fast Fourier Transform is used to perform the Fourier transform of this synthesized complex discrete function. By calculating the phase of the discrete complex function after the Fourier transform and combining with the corresponding intensity distribution of target image, a new synthesized complex function can be obtained by the inverse Fourier transform for the

next iteration. After multiple iterations (500 times in this design), the required phase profile can be obtained. The designed parameters of a target image for the hologram are illustrated in Figure 4.2b. The metadevices are designed to generate the holographic images at the angles of $30° \times 30°$, which correspond to the number of hologram pixel $(M \times N)$ of 1201×1201 pixels, and the number of desired images $(m \times n)$ of 301×301 pixels, where $m = 2M\Delta p\, tan(\Theta_h/2)/\lambda$ and $n = 2N\Delta p\, tan(\Theta_v/2)/\lambda$ [12, 39]. Here, Θ_h and Θ_v are the projection angles along the horizontal and vertical directions (see Figure 4.2a), respectively. Δp is the distance between neighbouring nanorods and λ is the operating wavelength.

In this design, centrosymmetric (a Chakkar image) and non-centrosymmetric (three dots) patterns are combined into a single target image for optical holography (Figure 4.2c). The centrosymmetric pattern is a pattern that can be recognised as the same geometry when it is rotated by 180°. Usually, the holographic image generated by geometric metasurfaces will be rotated by 180° when an incident polarization changes from RCP to LCP or vice versa [39]. Thus, the Chakkar image is expected to maintain the same pattern when the polarization state of the incident light beam is varied. The three dots around a centre of an image are designed to be sensitive to the polarization states of the incident beam, which can gradually change their intensity and position when the polarization state of the incident beam is changed. Then the target image is fed into the GS algorithm and the generated phase profile is shown in Figure 4.2d.

The metasurface includes two regions marked by I and II as shown in Figure 4.3a. The radius of the region I is r_1, and the inner radius and the outer radius of the region II are r_1 and r_2, where $r_1 = 120$ μm and $r_2 = 180$ μm. The overall size of the designed device is 360 μm. The region I is used for image concealment, while the region II is used for optical holography. According to the generated phase profile in Figure 4.2d, the selected phase profile of the holography related to the region II is shown in Figure 4.3b.

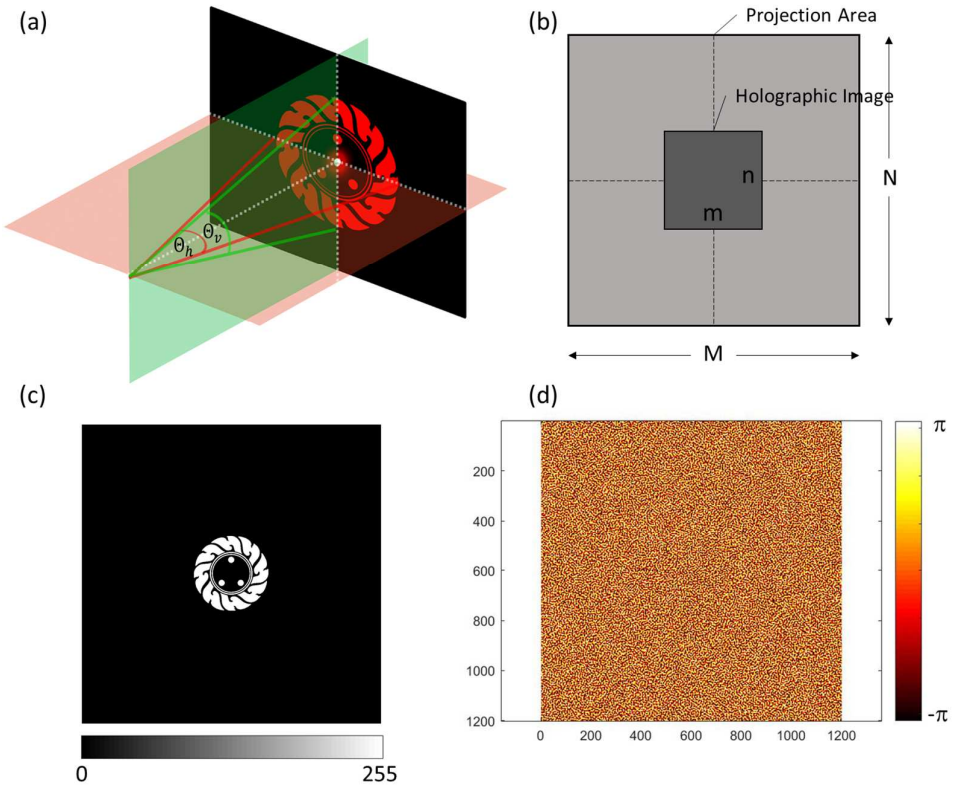

Figure 4.2 (a) Geometric parameters of the projected holographic images and the on-axis vector beams for image concealment. The full off-axis angles Θ_h and Θ_v for holographic image are designed to be 30°, while the hidden image is encoded in the polarization profile of the light beam along the optical axis. (b) Geometric parameters of the target image to generate a holographic image. (c) The target images for generation of the holographic images with the projection angle of 30° along horizontal and vertical axes. (d) Generated phase profiles of the target images by using the GS algorithm. M and N are the pixel numbers of the hologram along the x and y directions, while m and n are the pixel numbers for the desired image. $M = N = 1201$, $m = n = 301$.

According to Malus' law, the output intensity (I) is proportional to the square of $cos\,\theta$, where θ is the angle between the direction of the incident LP and the transmission axis of the analyser. Suppose the reference axis is chosen along the x-direction, the output intensity is changed to $I = I_0 \sin^2 \varphi$, where φ is the polarization angle of the incident LP w.r.t. the x-axis, and I_0 is the intensity of that incident LP. The hidden grayscale image with 1201 × 1201 pixels and the required polarization profile based on $\varphi_{(x,y)} = \sin^{-1}\left(\sqrt{I_{(x,y)}/I_0}\right)$ are shown in Figure 4.3c and Figure 4.3d, respectively. LP light with an angle φ between the polarization direction and the horizontal axis can be considered by the superposition of two orthogonal circular polarization with equal components, i.e. $RCP \cdot e^{i\varphi}$ and $LCP \cdot e^{-i\varphi}$ [55], which can be realized with a geometric metasurface that can generate spatially variant phase profile φ for RCP and $-\varphi$ for LCP under the illumination of LP light. Thus, the required polarization profile in Figure 4.3d is also

related to the phase profile for RCP. Finally, the combined phase profile for both hologram and image concealment is depicted in Figure 4.4a. The designed metadevice is realised by using transmissive metasurfaces as described in Section 2.4 and its corresponding SEM image is shown in Figure 4.4b. At this moment, the developed metadevice is ready to characterise. The experimental setups based on the diagram in Figure 2.4 and 2.6 are then built up to test the metadevice.

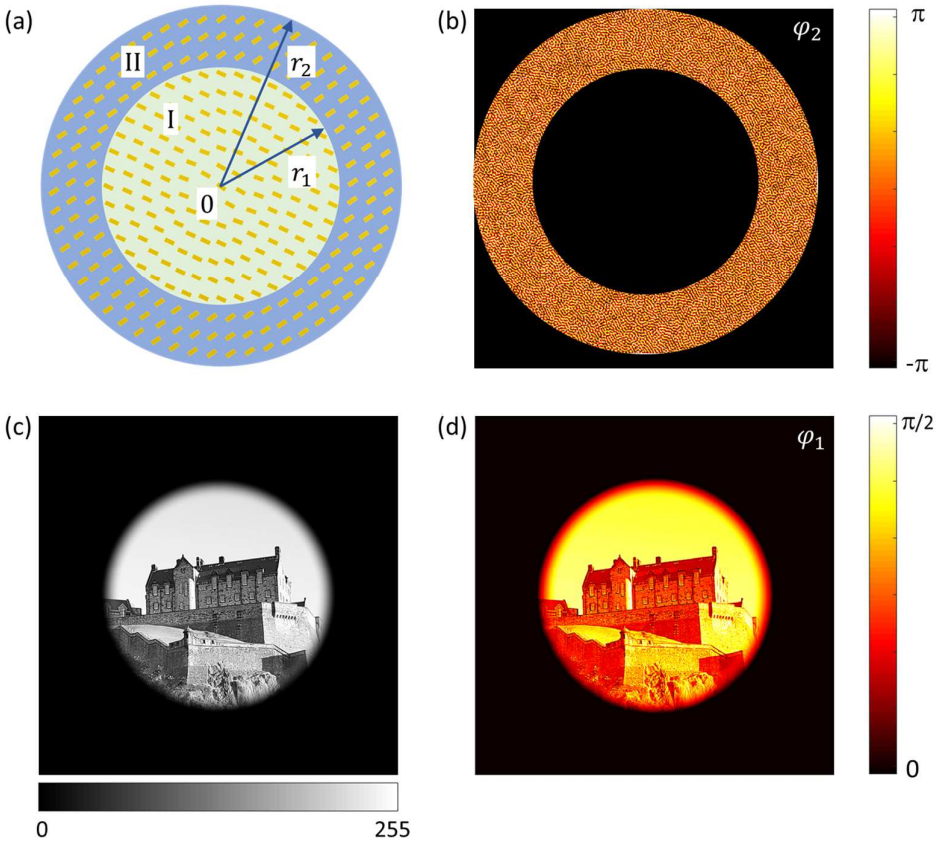

Figure 4.3 (a) Schematic illustration of the designed metadevice including two regions marked by I and II. The radius of the region I is r_1, the inner radius and the outer radius of the region II are r_1 and r_2. $r_1 = 120$ μm and $r_2 = 180$ μm. (b) the selected phase profile φ_2, which is calculated based on the Gerchberg-Saxton algorithm. (c) The high-resolution target image for image concealment and (d) the required phase profile φ_1.

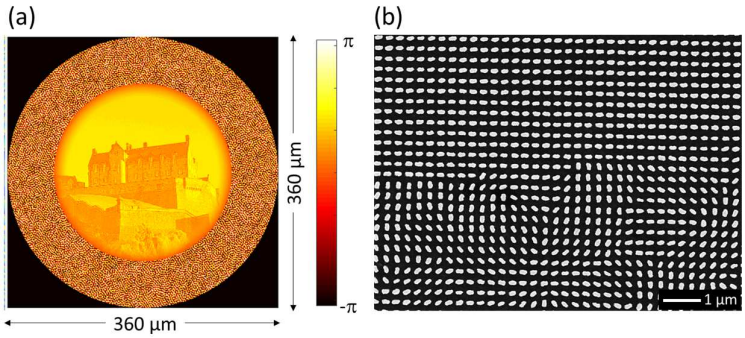

Figure 4.4 (a) The phase profile and (b) SEM image of the metadevice to generate the image concealment and hybrid hologram.

4.2.2. Hybrid Hologram

The experimental result in Figure 4.5a (left) shows that the image-hidden functionality is unambiguously realized. A high-quality image with detailed information (e.g., tracery of windows and the wall) is revealed (Figure 4.5a (right)) after passing through the analyser. Here, the transmission axes of the polarizer and the analyser are in horizontal and vertical directions, respectively. Figure 4.5b shows the reconstructed image on the image plane with a distance of 17 cm between the screen and the metadevice at the wavelength of 650 nm. A clear image with high fidelity and no distortion are observed when the metadevice is illuminated with the LCP light.

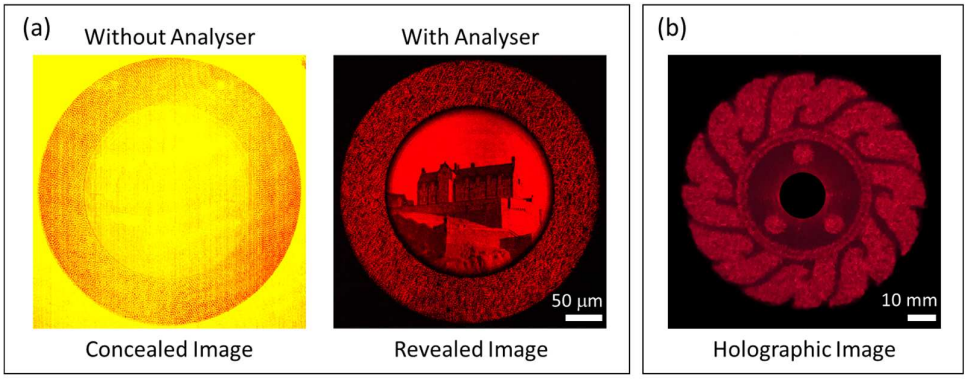

Figure 4.5 (a) The concealed images in the light beam before and after passing through an analyser with a vertical transmission when the transmission axis of the polarizer and the fast axis of the QWP are in a horizontal direction. (b) The experimental result of the reconstructed image projecting on the screen when the incident light beam is LCP.

Figure 4.6a-4.6e show the measured and simulation results of the hybrid hologram under the illumination of incident light with different polarization states. The intensities of the six dots rise and fall according to the ellipticity of various incident polarized light, which is realized by changing the angle between the polarization axis of the polarizer and the

fast axis of the QWP. As we predict, the experimental results of the Chakkar image remain unchanged when the incident polarization is varied, while the dots are changed relative to those incident polarizations. Initially, only the three dots (1st group: blue-dash-circle marks in Figure 4.1) are observed around the optical axis on the image plane (Figure 4.6a) upon the illumination of the pure RCP. Gradually, we can find six dots with high intensity in the 1st group and low intensity of the new three dots (2nd group: green-dash-circle marks in Figure 4.1) when the sample is illuminated by right-handed elliptically polarized light (Figure 4.6b). The intensities of the six dots are the same upon the illumination of the linearly polarized light since it contains an LCP light beam and an RCP light beam with equal intensities (Figure 4.6c). The intensity of the 2nd group will dominate when the incident light is left-handed elliptically polarized (Figure 4.6d). Finally, only the 2nd group appears when LCP light is incident on the sample (Figure 4.6e).

Since the intensities of six dots are closely related to the polarization states, thus both helicity and ellipticity of those polarization states can be determined by measuring the light intensities in the six dots. The ellipticity η and helicity of the incident light can be calculated by the intensity ratio $\tau = I_{LCP}/I_{RCP}$, $\eta = \left(1-\sqrt{\tau}\right)/\left(1+\sqrt{\tau}\right)$. $\eta = \pm 1$ and $\eta = 0$ correspond to RCP (LCP) and LP, respectively [16, 117]. The ellipticities versus the incident polarization (a function of γ) are obtained, where γ is the angle between the transmission axis of the polarizer and the fast axis of the QWP. The measured and simulated results are given in Figure 4.6f, where the inset diagram illustrates the position of the 1st group of dots (blue dots) and the 2nd group of dots (green dots) for extracting the intensities. Furthermore, the simulated and measured polarization states of the incident light are given on a Poincaré sphere (Figure 4.6g), which shows good agreement between simulation and experiment.

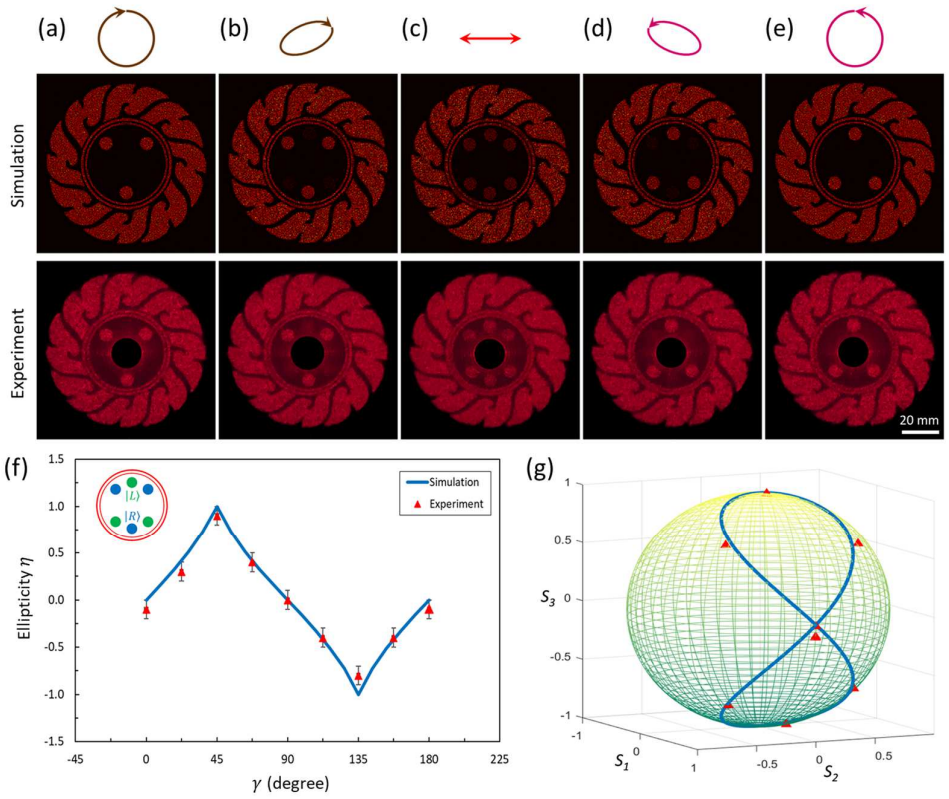

Figure 4.6 Reconstructed images versus incident polarization states and polarization measurements at the wavelength of 650 nm. The polarization states of the incident light are chosen to be (a) RCP, (b) REP, (c) LP, (d) REP, and (e) LCP. (f) Experimentally measured ellipticities η versus γ (an angle between the transmission axis of a polarizer and the fast axis of a QWP). The solid curve and discreet triangles represent the simulation and experimental results, respectively. Green three dots and blue three dots are the positions on holographic images used to extract the field intensity for LCP and RCP, respectively. (g) Poincaré sphere to show the experimentally measured polarization states of the incident light, experimental (rod triangles), and theoretical data (blue solid line).

4.2.3. Additional Functionality

Figure 4.7a shows the dependence of simulated and measured results on the direction of the transmission axis of the analyser while maintaining the transmission axis of the polarizer along a horizontal direction. The results without and with an analyser show the consistency between experimental and simulation results. The intensity of the non-converted part is much higher than the converted part when the analyser is not used. It is worth mentioning that the image is hidden in the polarization profile of the converted part. In our simulation, the intensity efficiency of the converted part and that of the non-converted part at the wavelength of 650 nm are 0.11 and 0.56, respectively. To better understand the image concealment approach, we also study the dependence of the image on the incident polarization state while the transmission axis of the analyser is fixed along the vertical direction. The polarization state is changed by controlling the angle between the transmission axis of the polarizer and the fast axis of the QWP. These simulation and

experimental results are shown in Figure 4.7b. The concealed image is unveiled clearly when the transmission axis of the analyser is perpendicular to the polarization direction of the incident LP. In our design, the incident light beam is a plane wave with uniform intensity, whereas it is a weakly focused laser beam in the experiment, leading to a slight discrepancy between the experimental and simulation results. Another possible reason for the discrepancy is the imperfection of the experimental setup and fabrication error.

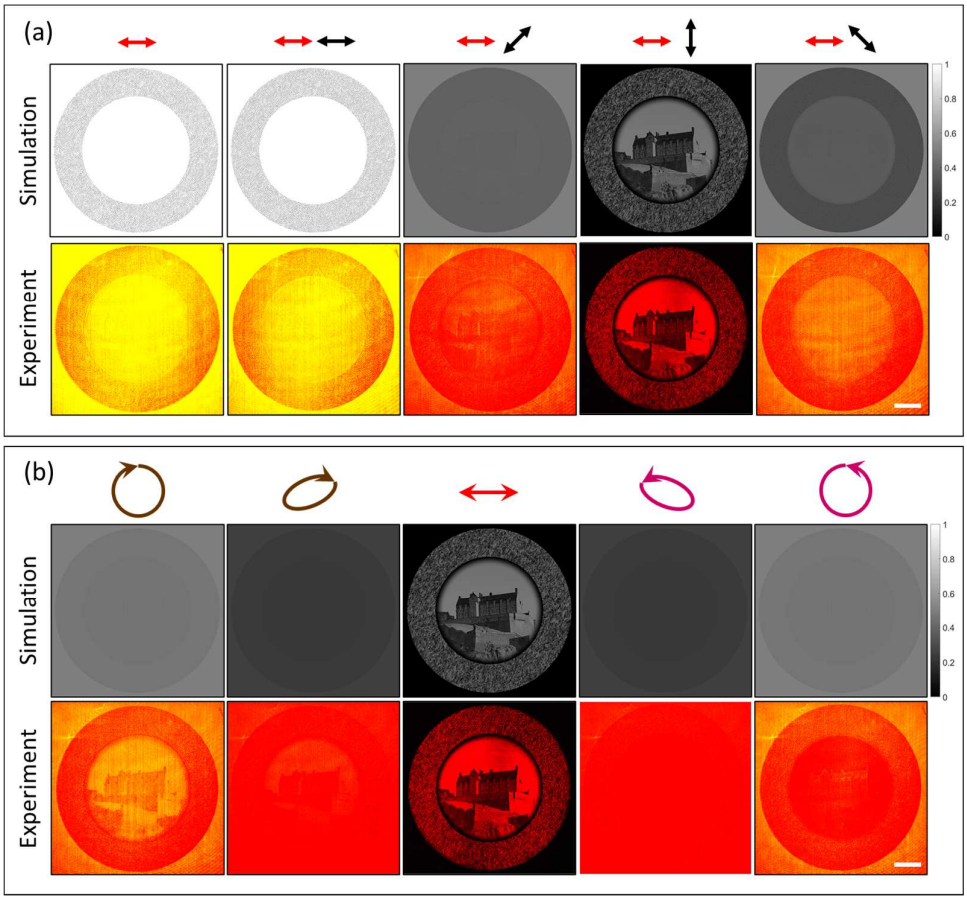

Figure 4.7 Characterization of the metadevice at the wavelength of 650 nm. (a) The simulated and experimental results for the analyser with various directions of the transmission axis (black double-headed arrows) when the incident light beam is linearly polarized along the horizontal axis (red double-headed arrows). Results without an analyser (first column) and with an analyser (second to fifth columns) with transmission axes of 0°, 45°, 90° and 135°. (b) The simulated and experimental results for the different polarization states of the incident light when the transmission axis of the analyser is fixed along the vertical direction. The polarization states are chosen to be RCP, right-handed elliptically polarized, linearly polarized (horizontal), left-handed elliptically polarized, and LCP. The scale bar is 50 μm.

Although the devices are designed at 650 nm, the measured hidden images and holographic images at other wavelengths are also observed (Figure 4.8a-b). We also notice that the size of the reconstructed images increases with the operating wavelength on the same screen.

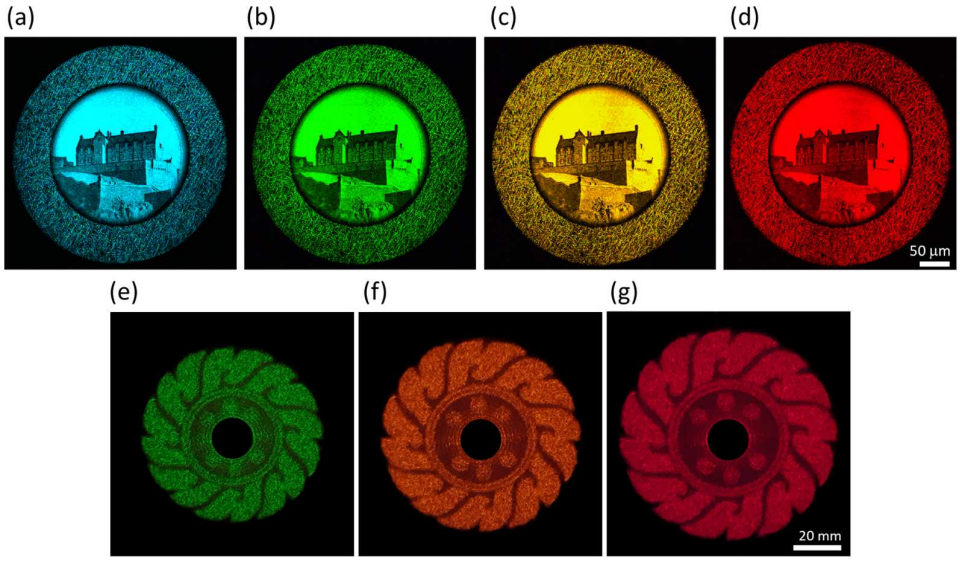

Figure 4.8 (a) The revealed images of image concealment captured by a CCD camera at the wavelength of (a) 500 nm, (b) 550 nm, (c) 580 nm, and (d) 650 nm. The reconstructed images of the hybrid hologram captured by a digital camera at the wavelength of (e) 550 nm, (f) 600 nm, and (g) 650 nm.

4.3. Polarization Detection with Light's Orbital Angular Momentum (OAM)

4.3.1. Design and method

In 1992, it was recognized that light beams with a helical phase structure described by $\exp(i\ell\theta)$, where θ is the azimuthal angle and ℓ is the topological charge (TC) of an optical vortex, carry an OAM of $\ell\hbar$ per photon [130, 131]. Twisted light beams have been applied in various research fields, including optical communication [132], optical trapping [133], new forms of imaging systems [134-136], nonlinear material [137, 138], and quantum optics [139-141]. As a promising candidate, optical metasurfaces have been used to generate various twisted light beams [11, 142, 143] and to control the superpositions of twisted light beams [51]. In this work, we propose and experimentally demonstrate a superposition of OAM beams and a facile metasurface approach to measure the polarization state of incident light based on the superposition of twisted light beams. The major axis and ellipticity of the polarized light are determined by the interference pattern of two twisted light beams with the same topological charges and opposite signs, while the handedness is measured by using topological charges with different values.

Figure 4.9 shows the schematic of our approach for polarization detection. When a light beam with unknown polarization shines on a reflective optical metasurface, the emitted light generates the superposition of two OAM states, which passes through an analyser (linear polarizer), whose transmission axis is fixed along the x-direction. The interference

patterns collected by a CCD camera are closely related to the polarization state of the incident light. Based on the analysis of the intensity distribution, the polarization state is directly measured. The direction of the major axis and the ellipticity of incident light are measured by the intensity distribution of the superpositions of OAM states with the same topological charges and opposite signs. The handedness of incident light is measured by the distance of two maximum intensities of the superpositions of OAM states with different topological charges and opposite signs.

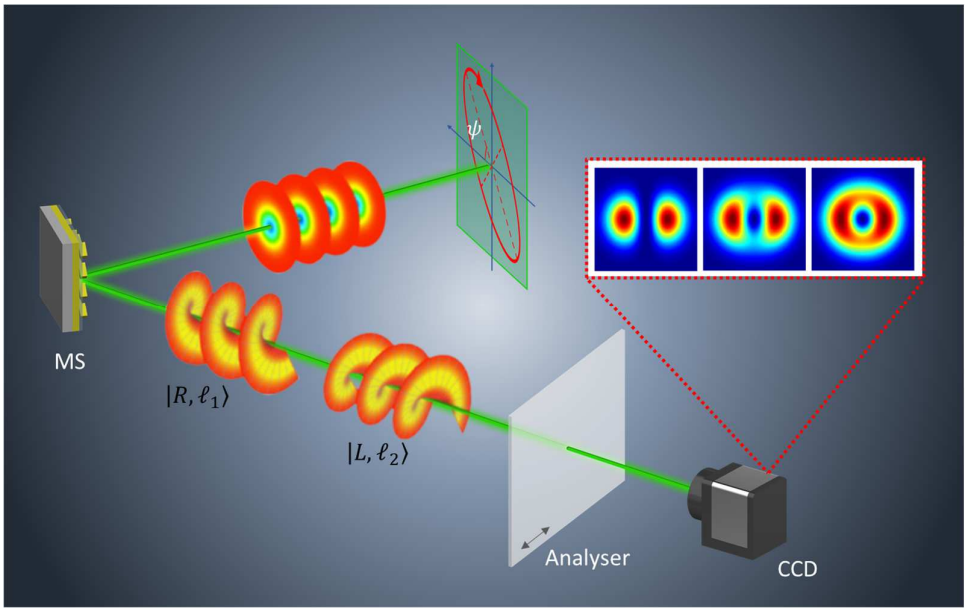

Figure 4.9 Schematic of the approach for polarization detection using light's OAM. A light beam with unknown polarization shines on a reflective optical metasurface. The emitted light generates the superposition of two OAM states with different topological charges (ℓ_1 and ℓ_2) and opposite circular polarizations, which are described by $|R, \ell_1\rangle$ and $|L, \ell_2\rangle$, where $|R\rangle$ and $|L\rangle$ represent RCP and LCP, respectively. The resultant beam is modulated by passing through an analyser (linear polarizer) whose transmission axis (denoted by a double-headed arrow) is fixed along the *x*-direction. A CCD camera is used to collect the interference patterns of OAM superposition, which is used to measure the polarization state of the incident light.

The superposition of OAM states is based on our recent work that indicates that the incident polarization can be used to arbitrarily control superpositions of OAM states using a single plasmonic metasurface [51]. The key point of this method is to design a reflective metasurface that can generate a phase profile, which can be used to produce two required OAM beams that can always meet with each other. Upon the illumination of incident light with pure circular polarization states (LCP or RCP), the two OAM beams can propagate along symmetry-equivalent directions with respect to the axis of incident light. The phase distribution of the metasurface is governed by

$$\Phi(x,y) = \arg\left(E_1 e^{i(\ell_1\theta+\Delta\phi_{off})} + E_2 e^{i(\ell_2\theta-\Delta\phi_{off})}\right) \quad (4.1)$$

where E_1 and E_2 represent the amplitude components of two ring OAM beams with TCs of ℓ_1 and ℓ_2, respectively. θ is the azimuthal angle and $\Delta\phi_{off}$ is the phase difference between neighbouring pixels to generate a phase gradient along the x direction, which can introduce off-axis deflection for the OAM mode of interest. To generate the off-axis reflection, the additional phase difference between neighbouring pixels of the sample along the direction is $\pi/5$, resulting in a reflection angle of 12.2° at the incident wavelength of 650 nm. It is worth mentioning that the off-axis design can avoid the disturbance of the non-converted part. To maintain high efficiency, we use reflective metasurfaces to develop the designed metasurface device where the details can be found in Section 2.5.

An arbitrary polarization state is the superposition of orthogonal circular polarizations. For example, an incident LP light beam along a direction angle α w.r.t. the *x*-axis can be decomposed into two equal-weighted RCP and LCP components with a phase difference, which can be described by $e^{i\alpha}|R,-\ell_1\rangle + e^{-i\alpha}|L,\ell_2\rangle$, where $|R\rangle$ and $|L\rangle$ represent RCP and LCP respectively. When an LP light shines on the metasurface, the superposition of OAM states with $\ell = 1$ and $\ell = -1$ is generated since a linearly polarized light beam can be decomposed into OAM beams with equal weight and opposite topological charges. The superimposed mode can be characterized by passing through a linear analyser and forming an angle ϑ with respect to the horizontal axis (*x*-axis). The Jones matrix of the analyser has the form [51]

$$\begin{bmatrix} \cos^2\vartheta & \sin\vartheta\cos\vartheta \\ \sin\vartheta\cos\vartheta & \sin^2\vartheta \end{bmatrix} \quad (4.2)$$

The transmitted intensity profile can be expressed by $\mathrm{E} = \frac{1}{2}[1+\cos^2(\ell\theta+\alpha+\vartheta)]$.

For two twisted light beams with the same topological charges and opposite signs, the transmitted intensity values are maximum at the azimuth angles $\theta_{max} = \frac{n\pi-\alpha-\vartheta}{|\ell|}$ ($n = 0, 1, \cdots, |2\ell|-1$), leading to $|2\ell|$ lobes. For $|\ell| = 1$ and the analyser with a fixed direction along the *x*-axis ($\vartheta = 0$), the angle between the major axis and *x*-axis is $\psi = \theta_{max} = -\alpha$. Here, θ_{max} is the angle between the line through the two maximum intensity points and the *x*-axis. Since the type of metasurface in this work is reflective so $\psi = \theta_{max} = \alpha$ for $\vartheta = 0$ and $|\ell| = 1$. The modulated intensity patterns (bright region and

dark region) can be used to determine the major axis of the ellipse. There exists a dark region (gap) between neighbouring bright petals. If the incident light is elliptically polarized, the darkest region will become brighter in comparison with LP, indicating this property can be used to determine the ellipticity of the polarized light. To measure the handedness of the polarized light, we use the superposition of two twisted light beams with different topological charges, which can produce OAM beams with different diameters. The handedness of the ellipse is determined by the dominated doughnut shape (brighter) with predesigned handedness. All developed metadevices in this section (Section 4.3) have been characterised by using the experimental setups in Figure 2.5 and Figure 2.10.

4.3.2. OAM Superposition

Prior to discussing polarization measurement, this section provides details about the superposition of multiple OAM beams. To experimentally realize the superposition of multiple OAM beams with different combinations of circular polarization states, a transmissive metasurface with an off-axis design is used. The schematic of the superposition mechanism is shown in Figure 4.10. The off-axis design can avoid the hassle of the non-converted part.

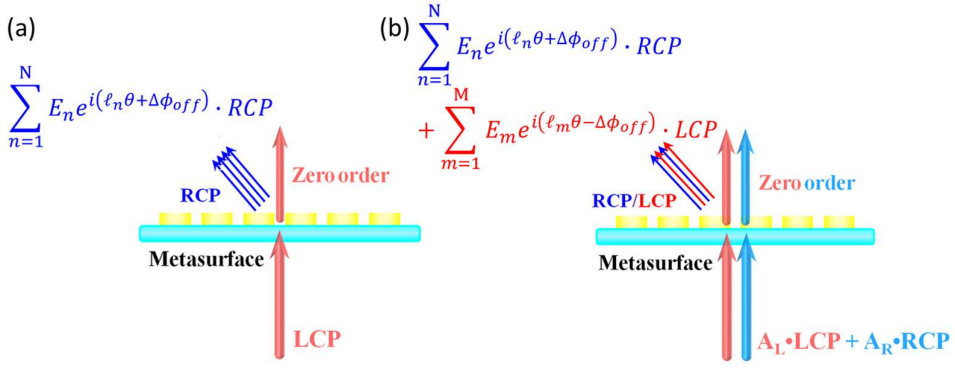

Figure 4.10 Schematic of the superposition mechanism. (a) Upon the illumination of a pure LCP light beam, the deflected light forms the OAM beams with the opposite circular polarization (RCP). (b) When the input light has an arbitrary polarization state (A_L·LCP + A_R·RCP), the OAM beams are generated with different combinations of circular polarization states.

The phase profile for the superposition of OAM beams with the same circular polarization states is given by

$$\Phi(x,y) = \arg\left(\sum_{n=1}^{4} E_n e^{i(\ell_n\theta+\Delta\phi_{off})}\right) \quad (4.3)$$

While the phase profile for the superposition of OAM beams with different circular polarization states is given by

$$\Phi(x,y) = \arg\left(\sum_{n=1}^{2} E_n e^{i(\ell_n \theta + \Delta\phi_{off})} + \sum_{n=3}^{4} E_n e^{i(\ell_n \theta - \Delta\phi_{off})}\right) \tag{4.4}$$

As shown in Figure 4.10a, when an LCP or RCP light beam shines on the metasurface, the OAM with the opposite circular polarization (RCP or LCP) is generated based on the deflected light through the superposition of multiple OAM beams, which are given in Equation 4.3. Figure 4.10b exhibits the other case when the input light has an arbitrary polarization state, which can be decomposed into LCP and RCP components. The resultant is formed by the superposition of OAM beams with different circular polarization states.

In the design, the values of ℓ in Equation 4.3 are $\ell_1 = 1$, $\ell_2 = 5$, $\ell_3 = 20$, $\ell_4 = -20$. Then, the calculated phase profile is shown in Figure 4.11a and its corresponding SEM image is shown in Figure 4.11b. The designed metadevices are realised by using transmissive metasurfaces as described in Section 2.4. The fabricated metadevice is characterised by using the experimental setup as described in Figure 2.5. In Figure 4.12, the experimental result is good agreement with the simulation result and the metadevice exhibits excellent broadband performance operated in the visible region (Figure 4.13).

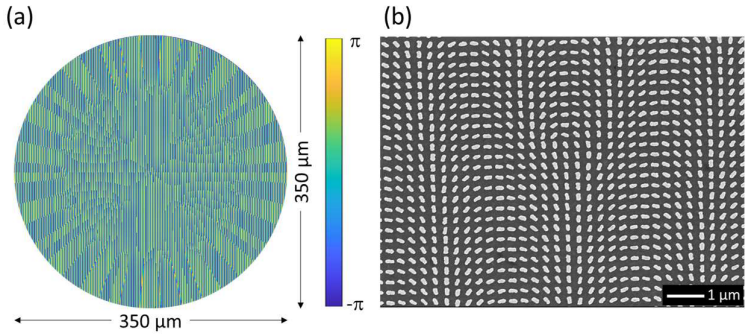

Figure 4.11 (a) The phase profile and (b) SEM image of the metadevice to generate the superpositions of four OAM beams with the same circular polarization states.

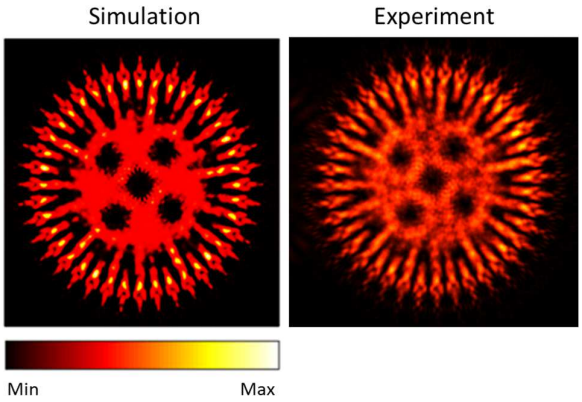

Figure 4.12 Simulation and experimental results for the superposition of four OAM beams with the same circular polarization states.

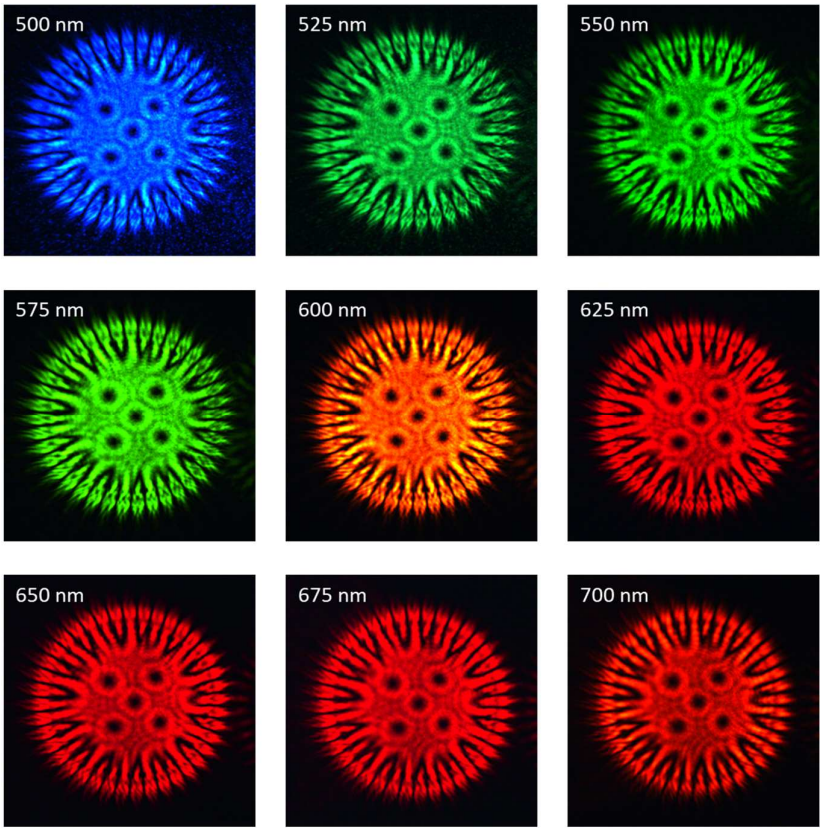

Figure 4.13 Broadband performance of the fabricated metadevice. The metadevice has been tested under the incident wavelengths from 500-700 nm.

For another design, the values of ℓ in Equation 4.4 are $\ell_1 = 1$, $\ell_2 = -1$, $\ell_3 = 7$, $\ell_4 = -7$. Then, the calculated phase profile is shown in Figure 4.14a and its corresponding SEM image is shown in Figure 4.14b.

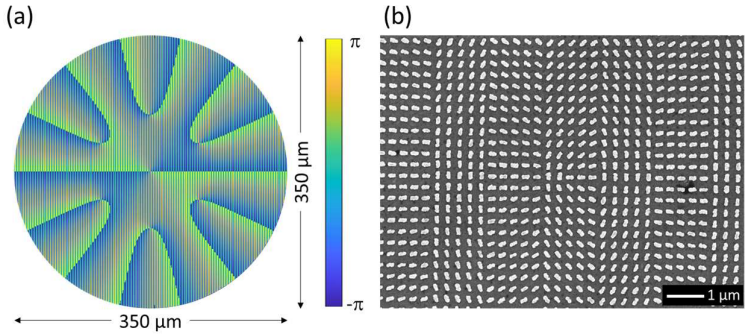

Figure 4.14 (a) The phase profile and (b) SEM image of the metadevice to generate the superpositions of four OAM beams with different circular polarization states.

Upon the illumination of the incident light with linear polarization, the simulation and experiment results are given in the first and second rows (Figure 4.15a), respectively. The red double arrows show the transmission axes of the linear polarizer. The transmission axis of the analyser is fixed along the vertical direction. The dark gaps in the middle of the intensity patterns clearly show the nature of the vector beam. The resultant OAM beams can be modulated by controlling the polarization state of the input light. The effect of different polarization states on the simulation and experiment results are given in Figure 4.15b. The fast axis of the quarter-wave plate and the transmission axis of the analyser are fixed along the horizontal and vertical directions, respectively. The polarization states of the incident light are changed by controlling the transmission axes of the first linear polarizer. Both the calculated and measured intensity patterns for the incident light with the circular polarization states (RCP and LCP) show a simple "flower" shape. Since an elliptical polarization state is an intermediate state between circular and linear polarization states, the intensity profile for the elliptical polarization state appears to be the combination of the intensity distributions for the two polarization states.

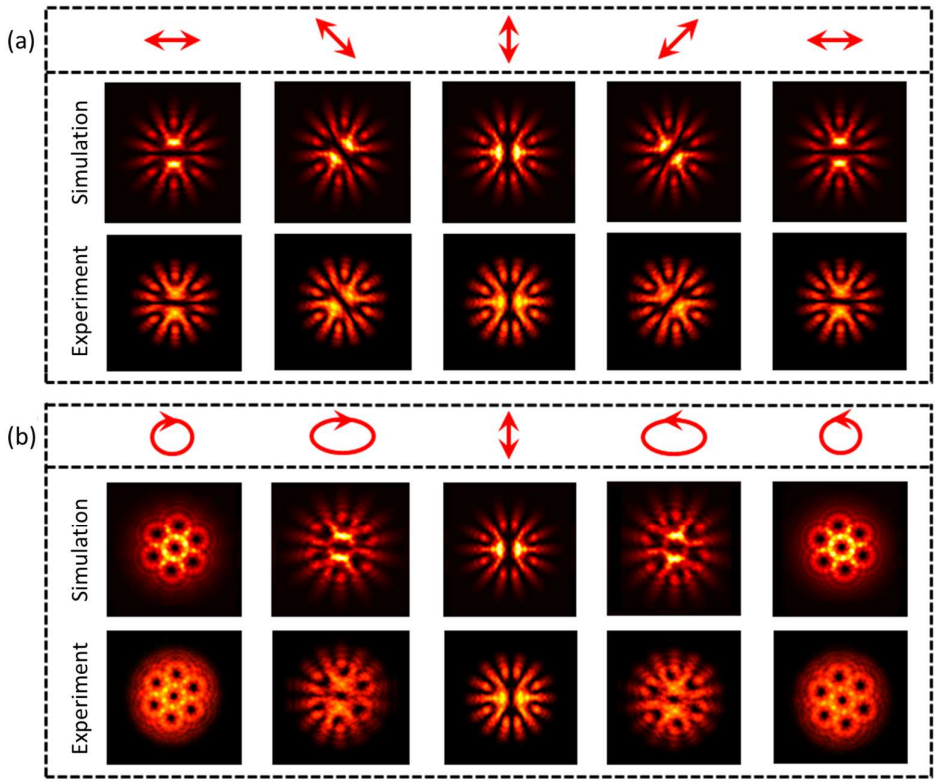

Figure 4.15 The superposition of four OAM beams with different circular polarization states. (a) Intensity patterns of the OAM beams after passing through an analyser (linear polarizer) with a fixed transmission axis (vertical direction). The transmission axes of the first linear polarizer are denoted by the red double arrows. The QWP1 is removed here. (b) Effect of the polarization state on the intensity patterns. The fast axis of the quarter-wave plate and the transmission axis of the analyser are along the horizontal and vertical directions, respectively. To change the polarization state of the incident light, the transmission axis of the first linear polarizer is rotated.

4.3.3. OAM beam $\ell = 1$ and $\ell = -1$

From this section onwards, only the superposition of two OAM beams with different polarization states is experimentally demonstrated for the detection of light's polarization with the experimental setup shown in Figure 2.10. We firstly design a metasurface to measure the major axis and the ellipticity of the incident polarization based on the superpositions of OAM states with $\ell = 1$ and $\ell = -1$. Figure 4.16a shows the phase profile of the designed metadevice. Its corresponding SEM image is shown in Figure 4.16b.

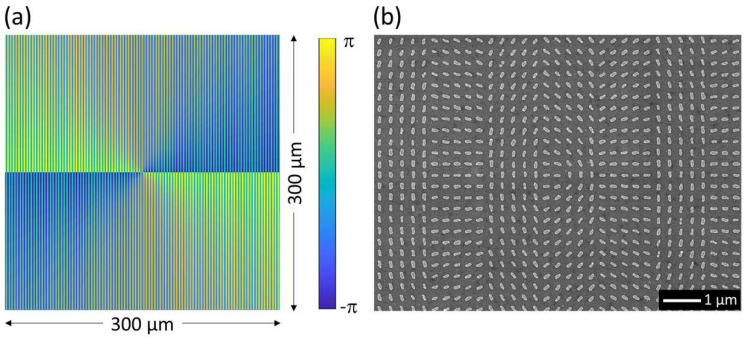

Figure 4.16 (a) The phase profile and (b) SEM image of the metadevice to generate the superpositions of OAM beams with $\ell = 1$ and $\ell = -1$.

Figure 4.17a shows the simulated superpositions of OAM states with $\ell = 1$ and $\ell = -1$ under the illumination of a linearly polarized beam. The transmission axes of the polarizer and analyser are 45° and 0° with respect to the *x*-axis, respectively. Figure 4.17b is the experimentally measured superpositions of OAM states. The image contains 460×460 pixels. The green circle in Figure 4.17b has a radius *r* around the centre of the Figure. The radius *r* is determined by the distance between the centre (the zero intensity) and the maximum intensity. To enhance the signal-to-noise ratio, the intensities in the ring region at each azimuth angle θ are considered, as schematically illustrated by the orange ring region in Figure 4.17b. The width *d* of the orange ring is 20 pixels. The intensity distribution along the orange ring is extracted based on an experimental result, as shown in Figure 4.17c. By integrating the intensity over the ring width at each azimuth angle θ ranging from 0° to 360°, the corresponding intensity distribution along the ring is obtained (shown by the blue curve in Figure 4.17d). Although there are many oscillations induced by the noise, which can be improved by using a fitted curve using the 10^{th} polynomial (denoted by the yellow colour), as shown in Figure 4.17d. In comparison with an experimental result, the corresponding simulation result is given in the red curve (Figure 4.17d). Both simulation and experiment have a maximum value of 45 degrees, indicating there is a good agreement between them. The slightly differences on the azimuth angles of 135 and 225 degrees are due to the distortion of the OAM beam after propagating through several optical elements, i.e., Obj., P2, and L2 in Figure 2.10. The distortion changes the OAM beam to be an asymmetric pattern that cannot fit well with the ring region. However, this difference is acceptable and enough for proof of our concept. To further confirm the validity of this approach, we measured various linear polarization states with different major axes by rotating the transmission axis of the polarizer, while the transmission axis of analyser is fixed along the horizontal direction.

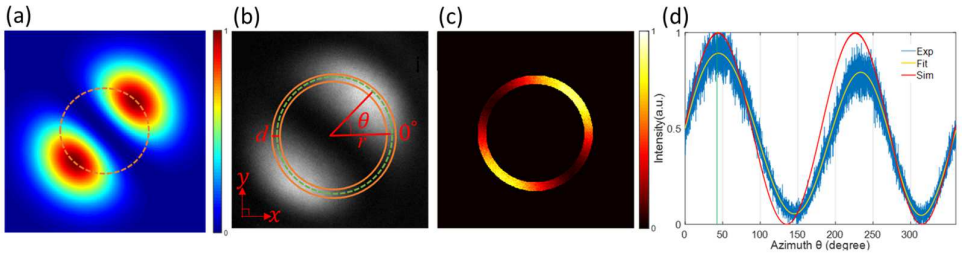

Figure 4.17 Measurement of the major axis of the polarization state. (a) Numerically calculated superpositions of OAM states with $\ell = 1$ and $\ell = -1$. The transmission axes of the polarizer and analyser are $\pi/4$ and 0 with respect to the x-axis, respectively. The orange dash circle passes through the two maximum intensity points. (b) The corresponding experimental result. The image contains 460×460 pixels. The green dash circle has a radius r around the centre of the Figure. The radius r is determined by the distance between the centre (the zero intensity) and the maximum intensity. To improve the signal-to-noise ratio, the intensities in the ring region at each azimuth angle are considered, as schematically illustrated by the orange ring region. The width d of the orange ring is 20 pixels. (c) The intensity distribution along the orange ring is extracted based on an experimental result, as shown in (b). (d) The relation between light intensity distribution in (c) and the azimuth angle. The experimental, fitted and simulated results are in blue, yellow, and red colours. The yellow colour represents the 10^{th} polynomial fitting curve of experimental data.

Figure 4.18 shows numerically calculated and experimentally observed superpositions of OAM states with $\ell = 1$ and $\ell = -1$ when the rotation angles of the polarizer are 0°, 45°, 90° and -45°, respectively. Figure 4.18d presents the simulation (red curves) and experimental results (The blue colour represents the experimental data, and the yellow colour represents the 10^{th} polynomial fitting curve of experimental data), which are normalized intensity distributions as a function of azimuth angle θ, respectively. Because our proposed metasurface is a reflective type, the green vertical line points to the first maximum intensity, whose θ_{max} just corresponds to the major axis $\psi = \theta_{max} = \alpha$ of incident linearly polarized light. The polarization direction of the incident linearly polarized light and the direction of the polarizer's transmission axis in front of the CCD camera are respectively denoted by the red and blue double-headed arrows in the first row of Figures. As we expect, the predesigned major axes of the polarization states agree well with the measured values.

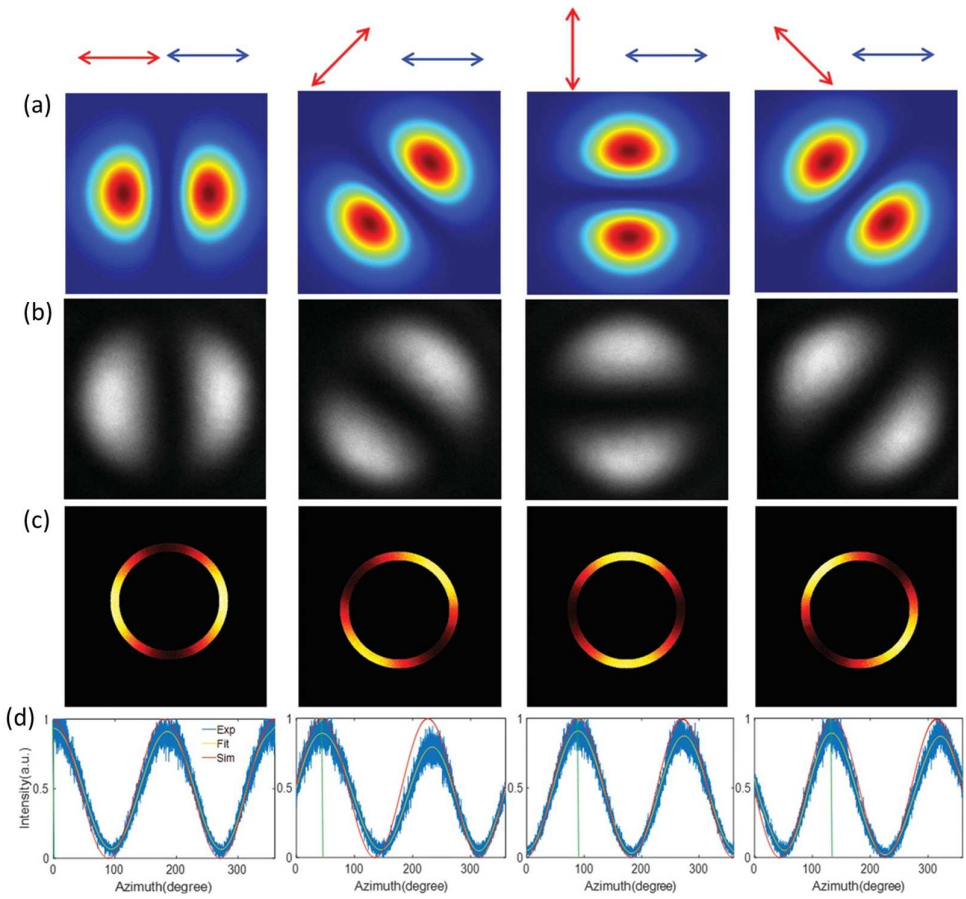

Figure 4.18 Numerically calculated and experimentally obtained results for the measurement of the major axis. (a) Simulation results for the superpositions of OAM states with $\ell = 1$ and $\ell = -1$ when the rotation angles of the polarizer are 0°, 45°, 90°, and −45°, respectively. The polarization direction of the incident linearly polarized light and the direction of the polarizer's transmission axis in front of the CCD camera are respectively denoted by the red and blue double-headed arrows. (b) Experimental results. (c) The intensity distributions along the orange ring in Figure 4.17b. (d) The relation between light intensity distribution in (c) and the azimuth angle.

The ellipticity of the incident polarization state can be determined by comparing the intensity of minimum and maximum from the images. Figures 4.19a and 4.19b show the simulation and experimental results of the intensity distribution for a typical polarization state of the incident light, respectively. The experimentally obtained intensity distribution for the superpositions of OAM states with $\ell = 1$ and $\ell = -1$ is processed by the software ImageJ. The spots A and B on the circle represent the two minimum intensity points in the simulation results, while C and D represent two maximum intensity points in the simulation results. The minimum intensity spots A' and B' on the circle are denoted by $I_{A'}$ and $I_{B'}$ and the maximum intensity spots C' and D' are denoted by $I_{C'}$ and $I_{D'}$ in experimental results. In order to decrease error, the ellipticity η of the incident light can be calculated by the intensity ratio of minimum intensity and maximum intensity, that is $\eta = \sqrt{(I_{A'} + I_{B'})/2}\,/\sqrt{(I_{C'} + I_{D'})/2}$. $\eta = 1$ and $\eta = 0$ correspond to CP and LP,

respectively. Figure 4.19c shows the simulation and experimental results of the ellipticity for the incident light with various polarization states, which are realized by rotating the transmission axis of the polarizer with the angle $\alpha = 0°, 10°, 20°, 30°, 40°, 45, 50°, 60°, 70°, 80°, 90°$ while the fast-axis of QWP and the transmission axis of analyser are fixed along the *x*-direction. The details for the generation of various polarization states can be found in Section 2.6. The experimental results of the light intensity distribution at the above angles are given in the insets of the figure. A clear dark boundary line between two petals and a doughnut shape is observed at $\alpha = 0°$ (linear polarization along the *x*-axis) and $\alpha = 45°$ (circular polarization), respectively. The two petals are located at the top and bottom at $\alpha = 90°$ (linear polarization along the *x*-axis). The two petals are gradually joined with each other with the increase of the angle from $0°$ to $45°$, which is the inverse process for the range from $45°$ to $90°$. As we can see from Figure 4.19c, the experimental data (blue triangle) and simulation data (black line) agree very well with each other. The slight difference between experiment and simulation is due to the imperfection of the sample and measurement error.

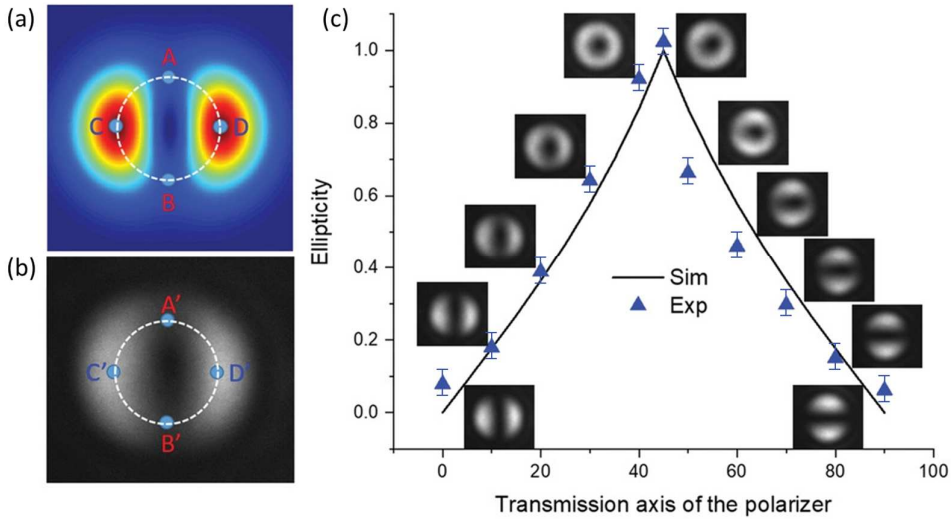

Figure 4.19 Ellipticity measurement based on the minimum and maximum intensities from the images. (a) Simulation and (b) experimental results of the intensity distribution for a typical polarization state of the incident light. The experimentally obtained intensity distribution for the superpositions of OAM states with $\ell = 1$ and $\ell = -1$ is processed using the software ImageJ. The minimum intensity spots A′ and B′ on the circle are denoted by $I_{A'}$ and $I_{B'}$ and the maximum intensity spots C′ and D′ are denoted by $I_{C'}$ and $I_{D'}$ respectively, while the corresponding intensity spots A, B, C, and D for simulated results. (c) Measured and simulated ellipticity value when the transmission axis of the polarizer changes. The experimental interference patterns are given in the insets.

4.3.4. OAM beam $\ell = 1$ and $\ell = -3$

In order to determine the handedness of incident polarized light, we fabricate a metasurface that can realize the superpositions of OAM states with $\ell = 1$ and $\ell = -3$. Figure 4.20a shows the phase profile of the designed metadevice. Its corresponding SEM image is shown in Figure 4.20b. Upon the illumination of LCP light, the doughnut shape has a smaller radius (corresponding to $\ell = 1$), which will become bigger (corresponding to $\ell = -3$) when the polarization state of the incident light is RCP as illustrated in Figure 4.21. Thus, we can tell the handedness of the incident light by comparing the light intensity on the two light rings as demonstrated in Figure 4.22. To facilitate data analysis, we choose a light intensity profile along a rectangle region (edge marked the orange line) with a width of 10 pixels passing through the centre of the superposed mode. The orange dash line in the numerical figure is the vertical centre of the light intensity distribution. We extract 600 × 600 pixels of the centre of the image. The handedness of incident polarized light is determined by the distance between two peak intensities. The normalized intensity profiles of numerically calculated and experimentally observed superpositions of OAM states with $\ell = 1$ and $\ell = -3$ are given in Figure 4.22. To confirm the proposed idea, the incident light with various polarization states is used to evaluate the performance of the fabricated sample. The two figures at the bottom are the polarization profiles of normalized intensity for the linear polarization, and the distance between two green vertical dash lines is about 300 pixels. The distances between two green vertical dash lines in the first column become narrower and narrower from bottom to top, indicating that the polarization state changes from linear polarization to left elliptical polarization, and then to left circular polarization (smallest distance). In comparison with the first column, the distances between two green vertical dash lines in the second column become wider and wider from bottom to top, indicating the polarization states changes from linear polarization to right elliptical polarization and then to right circular polarization.

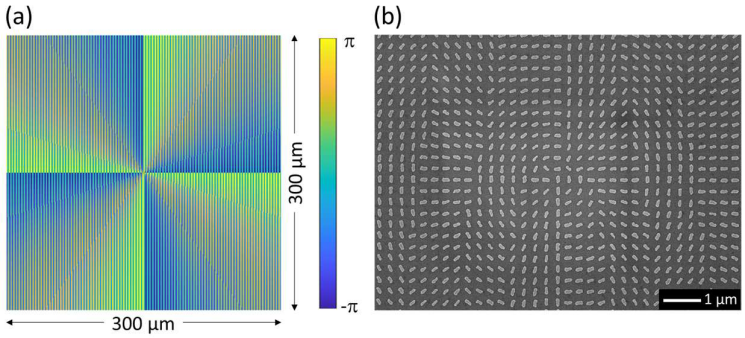

Figure 4.20 (a) The phase profile and (b) SEM image of the metadevice to generate the superpositions of OAM beams with $\ell = 1$ and $\ell = -3$.

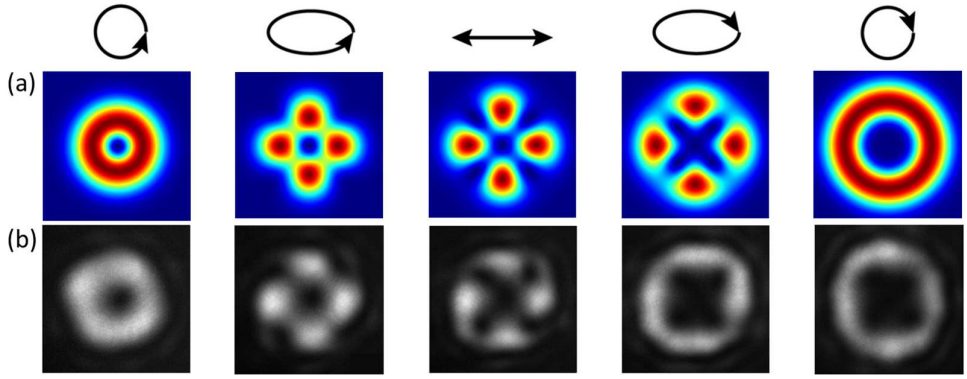

Figure 4.21 (a) Numerically calculated superpositions of OAM states with $\ell = 1$ and $\ell = -3$. (b) Experimentally observed superpositions of OAM states.

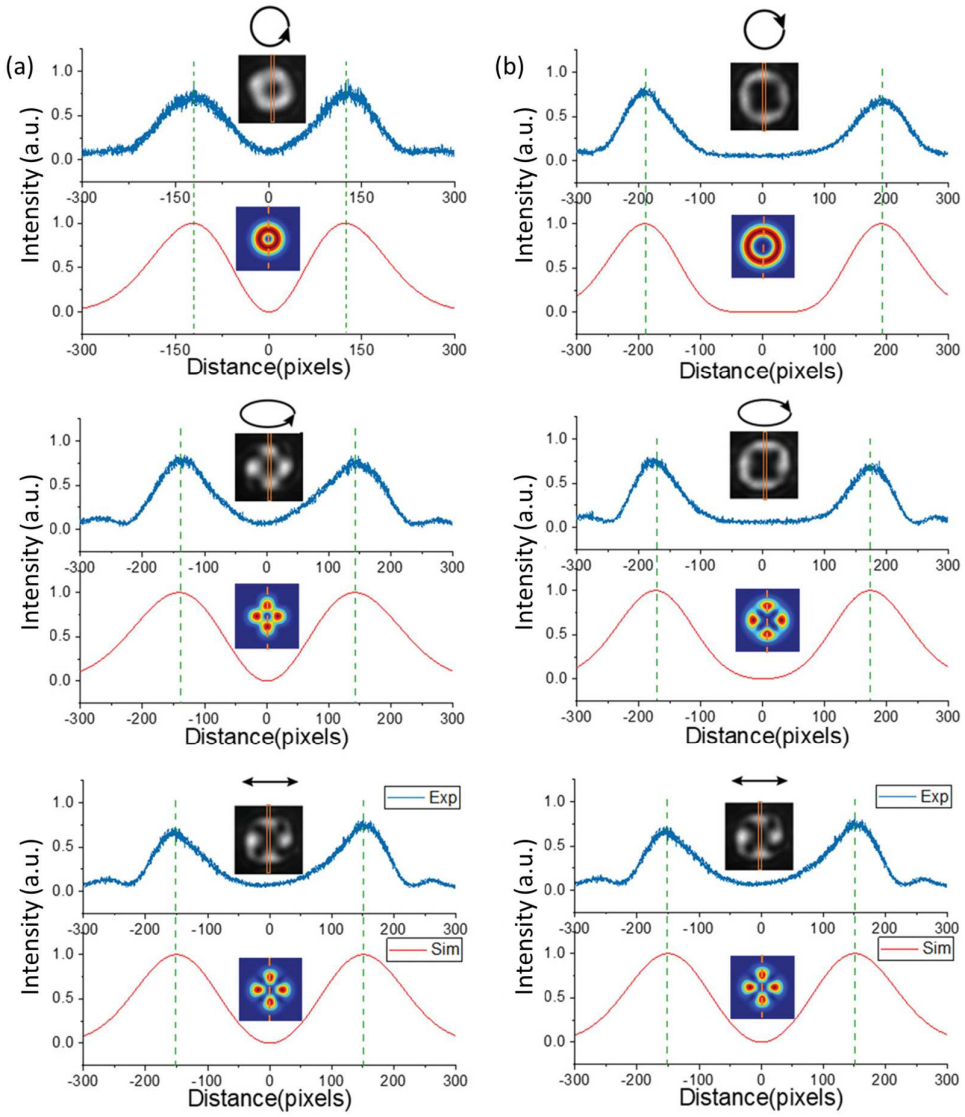

Figure 4.22 Handedness measurement based on the superposition of OAM beams with $\ell = 1$ and $\ell = -3$. (a) The two **figure**s at the bottom are the polarization profiles of normalized intensity for the linear polarization, and the distance between two green vertical dashed lines is about 300 pixels. The distance between two green vertical dash lines becomes narrower and narrower from bottom to top, indicating that the polarization state changes from linear polarization to left elliptical polarization, and then to left circular polarization (smallest distance). (b) The distance between two green vertical dashed lines becomes wider and wider from bottom to top, indicating that the polarization state changes from linear polarization to right elliptical polarization and then to right circular polarization. To facilitate analysis, we choose a light intensity profile along a rectangle region (edge marked by the orange dashed line) with a width of 10 pixels from top to bottom passing through the centre of the superposed mode based on the image processing software ImageJ. The orange dash line in the numerical **figure** is the vertical centre of the light intensity distribution. We extract 600 × 600 pixels of the centre of the image. The handedness of incident polarized light is determined by the distance between two peak intensities.

4.3.5. OAM beam $\ell = 2$ and $\ell = -2$

An interesting question is how to improve the accuracy of the polarization measurement based on this approach, especially the major axis of the polarization state, which can be improved by using the superpositions of the OAM beam with higher topological charges.

In the first experiment, there are only two petals in the interference patterns and one dark line passing through the centre. More petals and dark lines can increase the measurement accuracy since the major axis can be determined by the average values of angle shift at each maximum, equivalent to multiple measurements in an experiment. To test this idea, we fabricate a sample based on the superpositions of OAM states with $\ell = 2$ and $\ell = -2$, which can generate 4 petals with 2 dark lines. Figure 4.23a shows the phase profile of the designed metadevice. Its corresponding SEM image is shown in Figure 4.23b Various interference patterns from the superposition of OAM beams are obtained by rotating the transmission axis of the polarizer, while the transmission axis of the analyser is fixed along the horizontal direction. Figure 4.24 presents numerically calculated and experimentally observed superpositions of OAM states with $\ell = 2$ and $\ell = -2$ when the angles of the polarizer are $0°$, $45°$, $90°$ and $-45°$, respectively. It is worth mentioning that the major axis of the polarization state corresponds to the double angle shift of the petals.

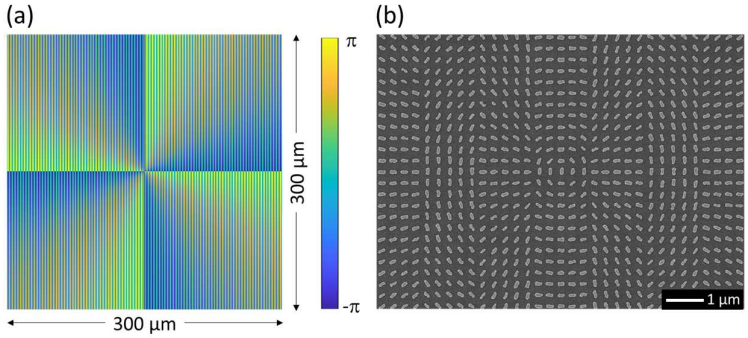

Figure 4.23 (a) The phase profile and (b) SEM image of the metadevice to generate the superpositions of OAM beams with $\ell = 2$ and $\ell = -2$.

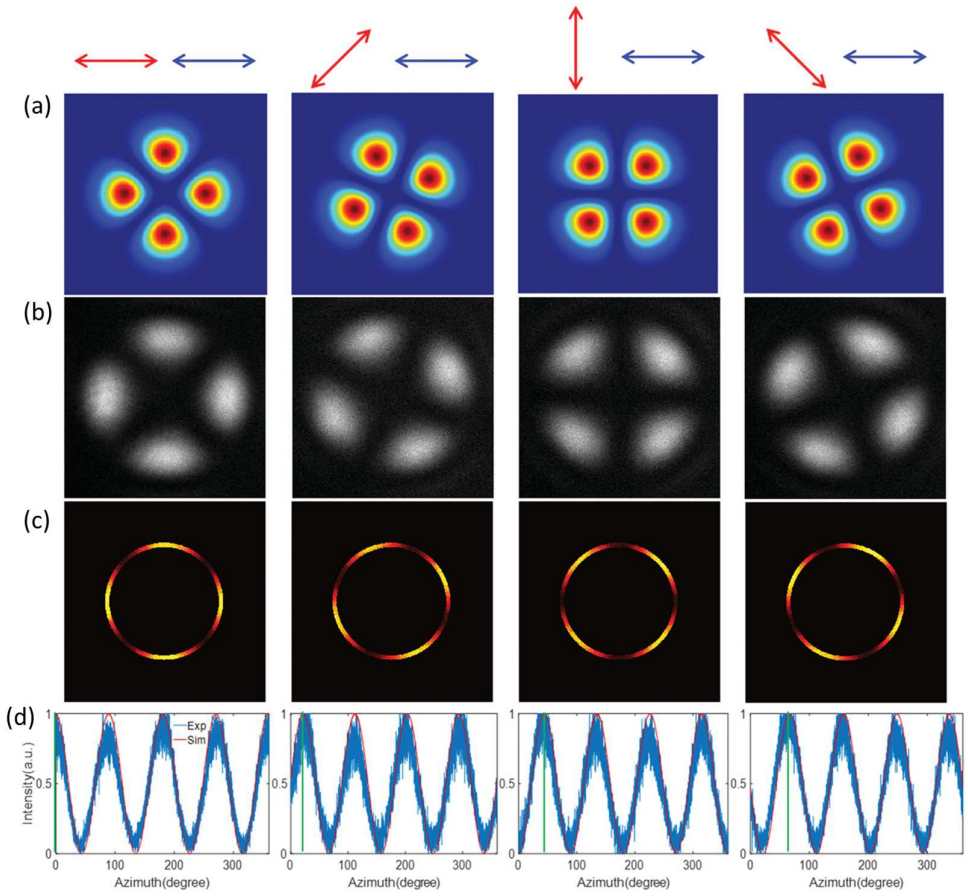

Figure 4.24 Major axis measurement based on superpositions of OAM states with $\ell = 2$ and $\ell = -2$. (a) Simulation results for the superpositions of OAM states with $\ell = 2$ and $\ell = -2$ when the rotation angles of the polarizer are 0°, 45°, 90°, and −45°, respectively. The polarization direction of the incident linearly polarized light and the direction of the polarizer's transmission axis in front of the CCD camera are denoted by the red and blue double-headed arrows, respectively. (b) Experimental results. (c) The intensity distributions along the orange ring in Figure 4.17b. (d) The relation between light intensity distribution in (c) and the azimuth angle.

4.4. Polarization Detection with Optical Ring Vortex (ORV) Beams

4.4.1. Design and method

In section 4.3, polarization detection has been performed by using the superposition of two doughnut beams with the same and also different topological charges and opposite signs. Recently, Liu et al. have experimentally demonstrated a 3D focused perfect vortex beam, which has a constant radius and is independent of TCs [144]. On the other hand, the superposition of OAM beams can generate novel structure beams [51, 145-147], for example, the superposition of $\ell = 1$ and $\ell = -1$ can give rise to a vector beam with a radially distributed polarization profile, which has been applied in various research fields, including focusing [148] and sensing [149]. However, the superposition of ring OAM beams in the far-field has not been studied. In this section, for the first time, we propose

and experimentally demonstrate an efficient method to generate the multiple ring OAM beams through a single metasurface, in which the superposition between the generated OAM beams can be continuously tuned by varying the polarization state of the incident light. The developed device is also studied further to detect the polarization states of incident light beams.

Figure 4.25 shows the schematic of the experimental setup based on an ultrathin metasurface to generate ring OAM states, together with continuous manipulation of their superposition by varying the polarization of the incident light. A polarizer and a quarter-wave plate (QWP) are used to control the polarization state of the incident light. The emitted light from the metasurface generates the superposition of ring OAM beams, which is displayed on a screen after passing through an analyser (linear polarizer), whose transmission axis is fixed along the *x*-direction (see the double-headed arrow in the figure). The screen is a white paper board with an opening (diameter 6 mm) in the middle, which allows the incident light and zero-order reflected light to pass through. In the figure, we also show a typical experimental result of the superposition of ring OAM beams on the screen.

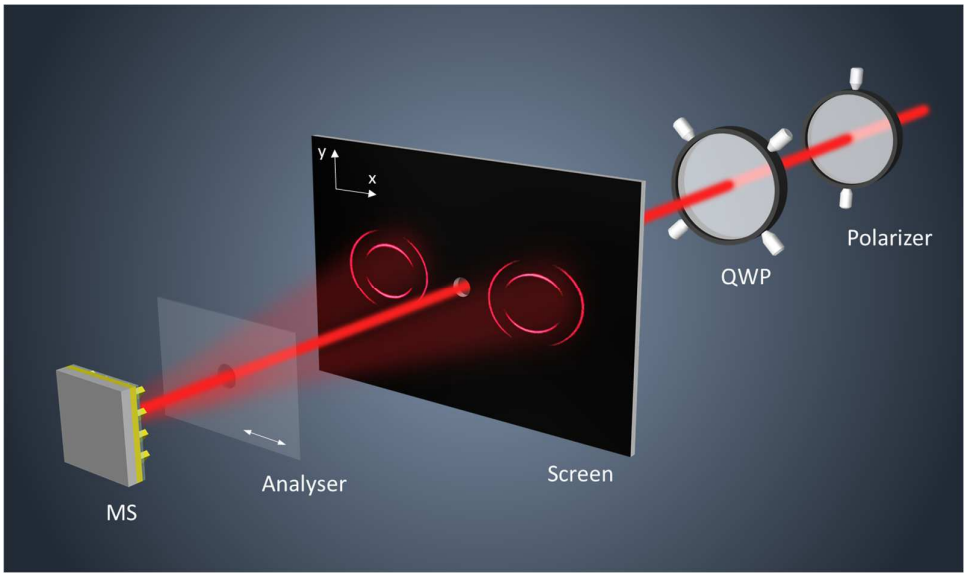

Figure 4.25 Schematic of the approach for generation and manipulation of ring OAM beams. Incident light with various polarization states is generated by a quarter-wave plate (QWP) and a polarizer. The emitted light from the reflective metasurface generates the superposition of two-ring OAM states, which is modulated by passing through an analyser (linear polarizer) whose transmission axis (white double-headed arrow) is fixed along the horizontal direction. The interference patterns of the superposition of ring OAM beams are displayed on the screen.

To generate ring OAM beams and realize their superposition, we design two different types of phase profiles based on the combination of phase profiles of a vortex beam generator, an axicon, and a beam deflector. $|L,\ell_1\rangle$ and $|R,\ell_2\rangle$ are used to describe a ring OAM state with left circular polarization and a TC of ℓ_1 and another ring OAM state with right circular polarization and a TC of ℓ_2, respectively. We start from an example to generate a superposition of two ring OAM beams with LCP incidence, the phase profile for the superposition of $|L,\ell_1\rangle$ and $|L,\ell_2\rangle$ on the left side of the screen is governed by

$$\Phi(x,y) = \arg\left(E_1 e^{i(\ell_1\theta+\Delta\phi_{off}+\phi_{axicon})} + E_2 e^{i(\ell_2\theta+\Delta\phi_{off}+\phi_{axicon})}\right) \tag{4.5}$$

where E_1 and E_2 represent the amplitude components of two ring OAM beams with TCs of ℓ_1 and ℓ_2, respectively. θ is the azimuthal angle and $\Delta\phi_{\text{off}}$ is the phase difference between neighbouring pixels to generate a phase gradient along the horizontal (x-) direction, which can realize the off-axis deflection. It is worth mentioning that the off-axis design can avoid the disturbance of the non-converted part [147]. $\phi_{axicon}(x,y) = -2\pi\sqrt{x^2+y^2}\,/\,d$ is the phase profile for the axicon, where d is the axicon period to control the radius of the generated ring OAM beam [22, 91]. The relationship between d and an axicon angle α can be expressed as $d\cdot\sin\alpha = \lambda$, where λ is the wavelength. Details of explanation are available in the references [22, 91]. In our design, $\Delta\phi_{\text{off}}$ is chosen to be $\pi/5$, corresponding to an off-axis angle of 12.4° at the wavelength of 650 nm. Although larger off-axis angles can be designed, it is not good for our experimental measurement since the collection of high-quality photos for images with wider viewing angles on both sides is more challenging. When the incident polarization changes from LCP to RCP, the superposition of $|R,-\ell_2\rangle$ and $|R,-\ell_1\rangle$ is on the right side of the screen since the sign of the generated phase profile is flipped. The superposition of ring OAM beams only occurs when they are on the same ring. There is a slight change in the diameter of the ring (equal to the sample size) on the right side when the incident light polarization is LCP or RCP. Only when the sign of phase for the axicon (plus or minus) is the same, the two ring OAMs have the same diameters and can generate superposition. For an elliptical polarization state, there are two different types of superpositions on both sides of the screen.

In order to generate the superpositions of $|L,\ell_1\rangle$ and $|R,-\ell_2\rangle$ on the left side and $|L,\ell_2\rangle$ and $|R,-\ell_1\rangle$ on the right side for any elliptical polarization, the phase profile for LCP incident light is governed by

$$\Phi(x,y) = \arg\left(E_1 e^{i(\ell_1\theta+\Delta\phi_{off}+\phi_{axicon})} + E_2 e^{i(\ell_2\theta-\Delta\phi_{off}-\phi_{axicon})}\right) \quad (4.6)$$

It should be noted that the superposition does not exist for pure circular polarizations (LCP or RCP) in this case, but it occurs for any elliptical or linear polarization states. Furthermore, the number of displayed dark gaps after passing through the analyser is determined by $|\ell_1 - \ell_2|$ [144]. Benefiting from high efficiency and broadband, reflective metasurfaces as discussed in Section 2.5 have been used to experimentally realize our proposed concept. The experimental setup in Figure 2.9 is used to characterise the developed devices.

4.4.2. ORV Beams with TCs of Same Absolute Values and Opposite Signs

A typical polarization state can be described by the major axis of polarization, the ellipticity, and handedness (clockwise or anticlockwise). The effect of the major axis of polarization state on the superposition is initially investigated. Based on Equation 4.6, we first design and fabricate two metasurfaces that can generate the superposition of ring OAM states with TCs of the same absolute values and opposite signs (one for $|L,\ \ell_1 = 1\rangle$ and $|R,\ \ell_2 = -1\rangle$ and another for $|L,\ \ell_1 = 2\rangle$ and $|R,\ \ell_2 = -2\rangle$). The phase profile used to generate the superposition of ring OAM beams $|L,\ \ell_1 = 1\rangle$ and $|R,\ \ell_2 = -1\rangle$ is shown in Figure 4.26a. Figure 4.26b shows the SEM image of the fabricated metasurface, which is used to study the relationship between the major axis and superposition of ring OAM beams $|L,\ \ell_1 = 1\rangle$ and $|R,\ \ell_2 = -1\rangle$. The phase profile and SEM images of the metadevice for $|L,\ \ell_1 = 2\rangle$ and $|R,\ \ell_2 = -2\rangle$ are shown in Figures 4.26c and 4.26d, respectively. There is image distortion since the centre of each light beam on one side is not perpendicular to the screen. To solve this issue, we collect the image on one side. By continuously changing the transmission axis of the polarizer, the evolution process of the intensity distribution can be observed, as shown in Figure 4.27. The resultant output beam from the superposition of ring OAM beams $|L,\ \ell_1 = 1\rangle$ and $|R,\ \ell_2 = -1\rangle$ with equal components is an azimuthally polarized ring vector beam upon the illumination of an LP beam with a major axis along the vertical direction (see Figure 4.27a). Although we have $\Delta\phi_{\text{off}}$ destroying the rotational symmetry of the sample in deflecting the superimposed beam to one side, two symmetrically distributed images of red rings with two dark gaps along the horizontal direction are faithfully generated and clearly observed after passing through the analyser with a transmission axis along the horizontal direction. By gradually rotating the polarization axis of the polarizer from the vertical direction to the horizontal direction, the azimuthally polarized beam is changed to a radially polarized beam, leading to the

rotation of two dark gaps on the screen. Furthermore, the rotation angle of gaps is equal to that of the transmission axis of the polarizer with respect to the vertical direction. To facilitate the measurement of the major axis, we set a clock dial on the ring. The results for the ring OAM superposition of $|L, \ell_1 = 2\rangle$ and $|R, \ell_2 = -2\rangle$ with equal components are also provided in Figure 4.27. There are four dark gaps on each light ring and the rotation angle of each gap is halved in comparison with the angle between the transmission axis of the polarizer and the horizontal direction. We can see that the number of gaps in the superposition of ring OAM states $|L, \ell_1\rangle$ and $|R, \ell_2\rangle$ is equal to $|\ell_1 - \ell_2|$. To further confirm the relation between the number of dark gaps and the TCs for the ring OAM superposition, we fabricate a sample to realize the superposition of $|L, \ell_1 = 1\rangle$ and $|R, \ell_2 = -2\rangle$ upon the illumination of LP light. The phase profile and SEM image are shown in Figures 4.26e and 4.26f, respectively. As predicted, three dark gaps are observed in the experimental result (Figure 4.27).

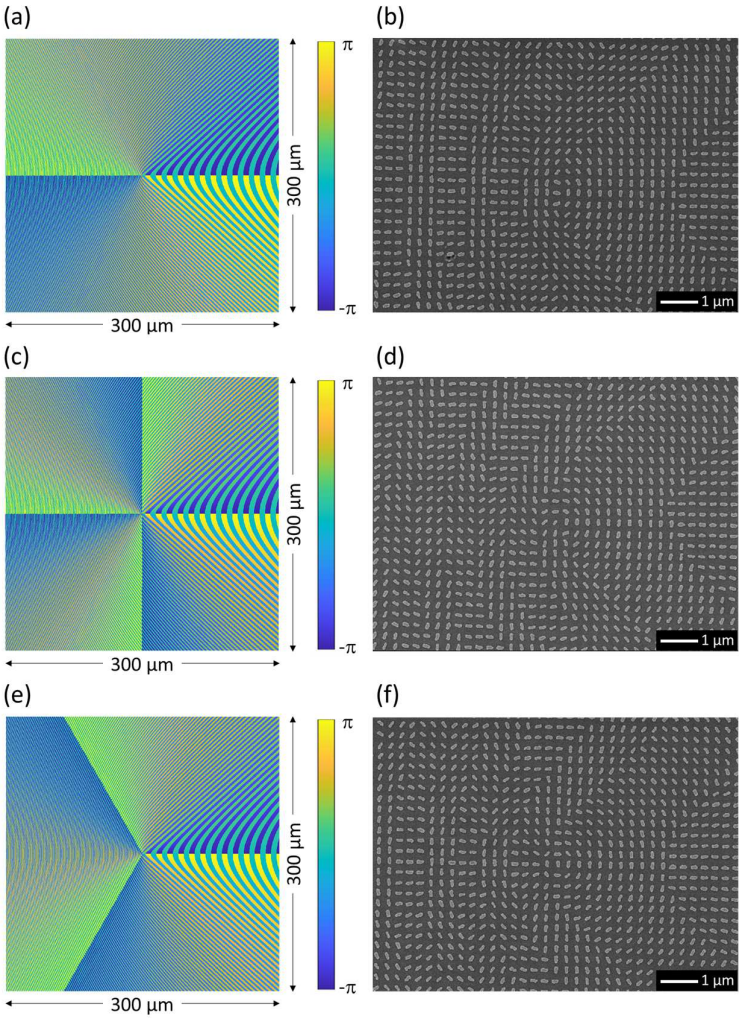

Figure 4.26 (a) The phase profile and (b) SEM image of the metadevice to generate the ring OAM beams with $|L, \ell_1 = 1\rangle$ and $|R, \ell_2 = -1\rangle$. (c) The phase profile and (d) SEM image of the metadevice to generate the ring OAM beams with $|L, \ell_1 = 2\rangle$ and $|R, \ell_2 = -2\rangle$. e) The phase profile and (f) SEM image of the metadevice to generate the ring OAM beams with $|L, \ell_1 = 1\rangle$ and $|R, \ell_2 = -2\rangle$.

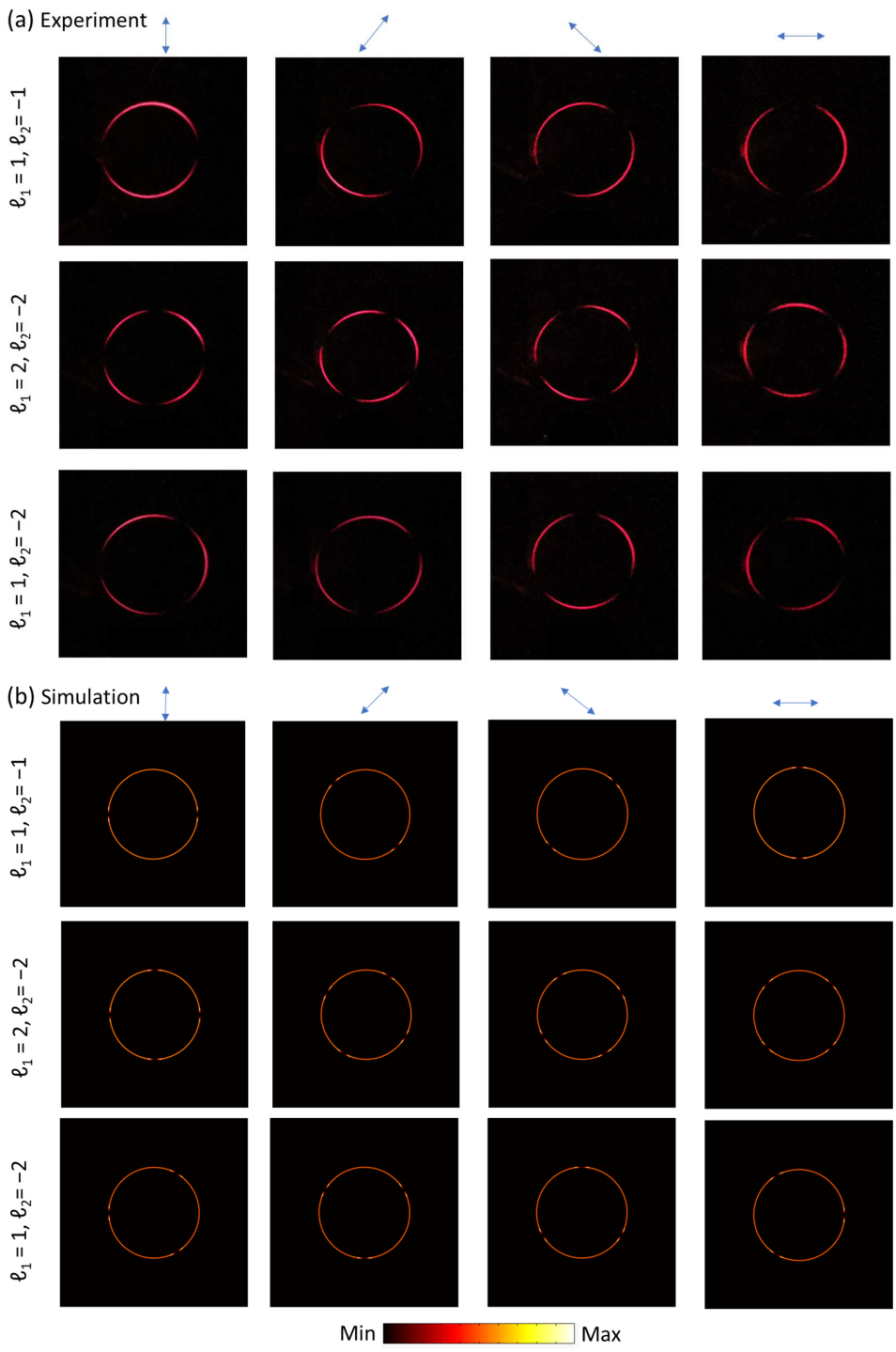

Figure 4.27 Effect of the major axis of the incident polarization on the superposition of the ring OAM beams. (a) Experimental results and (b) simulation results for the incident linear light polarization with different major axes (marked with double-headed arrows). The first, second, and third rows in each figure correspond to the superposition of ring OAM beams for $|L, \ell_1 = 1\rangle$ and $|R, \ell_2 = -1\rangle$, $|L, \ell_1 = 2\rangle$ and $|R, \ell_2 = -2\rangle$, and $|L, \ell_1 = 1\rangle$ and $|R, \ell_2 = -2\rangle$, respectively.

4.4.3. ORV Beams with TCs of Different Absolute Values and Same Signs

We then study the effect of ellipticity and handedness of the polarization state of the incident light on the superposition of ring OAM beams. We design and fabricate a metasurface that can generate the superposition of ring OAM states with TCs of different absolute values and the same signs ($|L, \ell_1 = 1\rangle$ and $|L, \ell_2 = 2\rangle$ for LCP). The phase profile and its corresponding SEM image are shown in Figures 4.28a and 4.28b, respectively. Suppose the fast axis of QWP is fixed along the vertical direction, five different ellipticities of the polarization states with a fixed major axis along the vertical direction can be generated by continuously changing the transmission axis of the polarizer. Only one ring OAM beam is observed on the left or right side of the screen upon the illumination of LCP or RCP light. However, two ring OAM beams can be observed when the incident light is elliptically polarized. When the polarization state is linear polarization, the ring pattern with the same intensity appears on both sides of the screen. The rise and fall of intensities in the ring patterns are closely related to the ellipticity of incident light. It is well known that completely polarized light is composed of LCP and RCP components. The ellipticity and the handedness of the polarized light can be deduced from the intensity ratio of its LCP and RCP component: $\eta = \left(1 - \sqrt{\tau}\right)/\left(1 + \sqrt{\tau}\right)$, where τ is the ratio of intensity component for LCP to that for RCP. η is changed by controlling the angle between the transmission axis of a linear polarizer and the horizontal direction. $\eta = \pm 1$ and $\eta = 0$ represent RCP (LCP) and the linear polarization light, respectively. In addition, $\eta > 0$ and $\eta < 0$ correspond to the right-elliptically polarized (REP) light and left-elliptically polarized (LEP) light, respectively [16, 113]. When the resultant beam from the superposition of ring OAM beams passes through the analyser, two split rings are observed since the uniform light intensity on the rings is modulated. Figure 4.29 shows the effect of various ellipticities and handedness on the superposition of the ring OAM beam passing through the polarizer. We can clearly see that the intensities on the two split rings change when the polarization state of the incident light is changed from RCP to REP, LP, LEP, and LCP. The dark gap originates from the superpositions of ring OAM beams with different topological charges and the same circular polarization states.

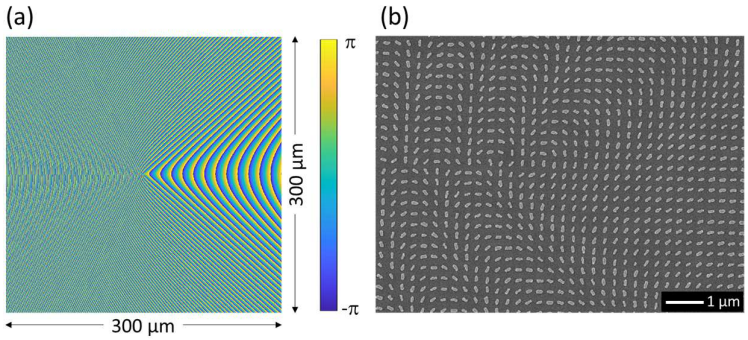

Figure 4.28 (a) The phase profile and (b) SEM image of the metadevice to generate the ring OAM beams with $|L, \ell_1 = 1\rangle$ and $|R, \ell_2 = 2\rangle$.

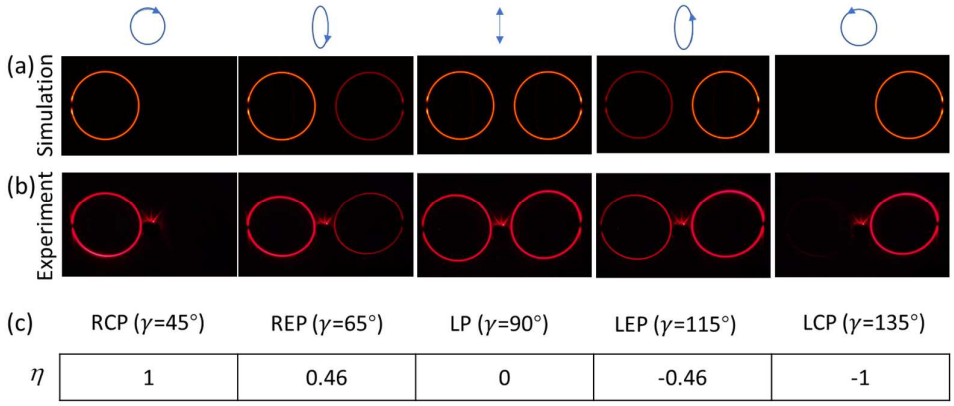

Figure 4.29 Effects of the ellipticity and the handedness of the incident polarization on the superposition of the ring OAM beams. (a) Simulation and (b) experimental results for the incident linear light polarization with different ellipticities and handedness. The evolution process of the intensity change on the two split rings is given when the polarization state of the incident light is changed from RCP to REP, LP, LEP, and LCP. (c) The ellipticity and the handedness of the polarized light are described by a parameter $\eta = \left(1 - \sqrt{\tau}\right)/\left(1 + \sqrt{\tau}\right)$, where τ is the ratio of intensity component for LCP to that for RCP. $\eta = \pm 1$ and $\eta = 0$ represent RCP (LCP) and the linear polarization light, respectively. In addition, $\eta > 0$ and $\eta < 0$ correspond to the REP light and LEP light, respectively. The values for η in the experiment are given in (c). γ is the angle between the transmission axis of the linear polarizer with respect to the horizontal direction.

4.4.4. Multiple ORV Beams

To simultaneously measure the major axis, ellipticity, and handedness of incident light with an unknown polarization state, we design a compact metasurface device that can generate multiple superpositions of ring OAM beams. The polarization detection is based on two split ring patterns. The inner ring and outer ring are used to detect the major axis and the ellipticity of the incident polarization, respectively. By comparing the intensities on the outer ring on both sides of the screen, one can determine the handedness of the incident polarization. We choose the superposition of $|L, \ell_1 = 1\rangle$ and $|R, \ell_2 = -1\rangle$ for the inner ring and that of $|L, \ell_3 = 1\rangle$ and $|L, \ell_4 = 3\rangle$ for the outer ring. It is worth mentioning that $|\ell_3 - \ell_4|$ does not need to be equal to $|\ell_1 - \ell_2|$. We next quantify the performance of the

device. The axicon periods for the inner and outer rings are designed to be $d_1 = 6$ μm and $d_2 = 4$ μm, respectively. The phase profile and its corresponding SEM image are shown in Figures 4.30a and 4.30b, respectively.

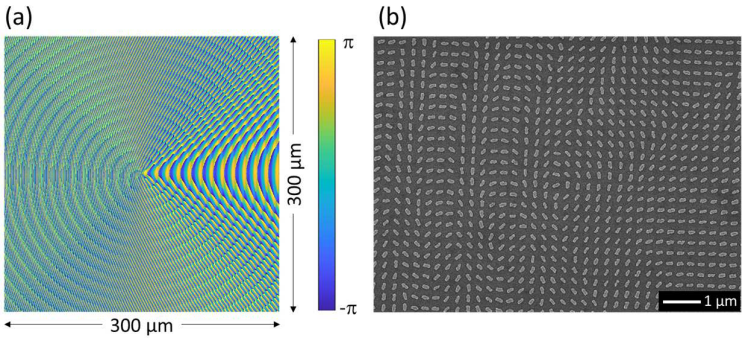

Figure 4.30 (a) The phase profile and (b) SEM image of the metadevice to generate the ring OAM beams with $|L, \ell_1 = 1\rangle$ and $|R, \ell_2 = -1\rangle$ for the inner ring and that of $|L, \ell_3 = 1\rangle$ and $|L, \ell_4 = 3\rangle$ for the outer ring.

Figure 4.31 shows the simulation and the experimental results for the measurement of the major axis of the polarization state. For the inner ring, no gap is obtained without the analyser due to the uniform intensity distribution. For the outer ring, a dark gap exists even without the aid of the analyser (see Figure 4.31a). If we place the analyser in front of the screen, a dark gap is observed in the inner ring (see Figure 4.31b). The double-headed arrow in the figure shows the major axis of the incident polarization state. The diameters of the inner ring and outer rings are 3.3 and 5.0 cm, respectively. The measured and predicted major axes are given by the blue double-headed arrows. The existence of a dim ring within the designed inner ring is due to the weak coupling between the inner and outer ring OAM beams.

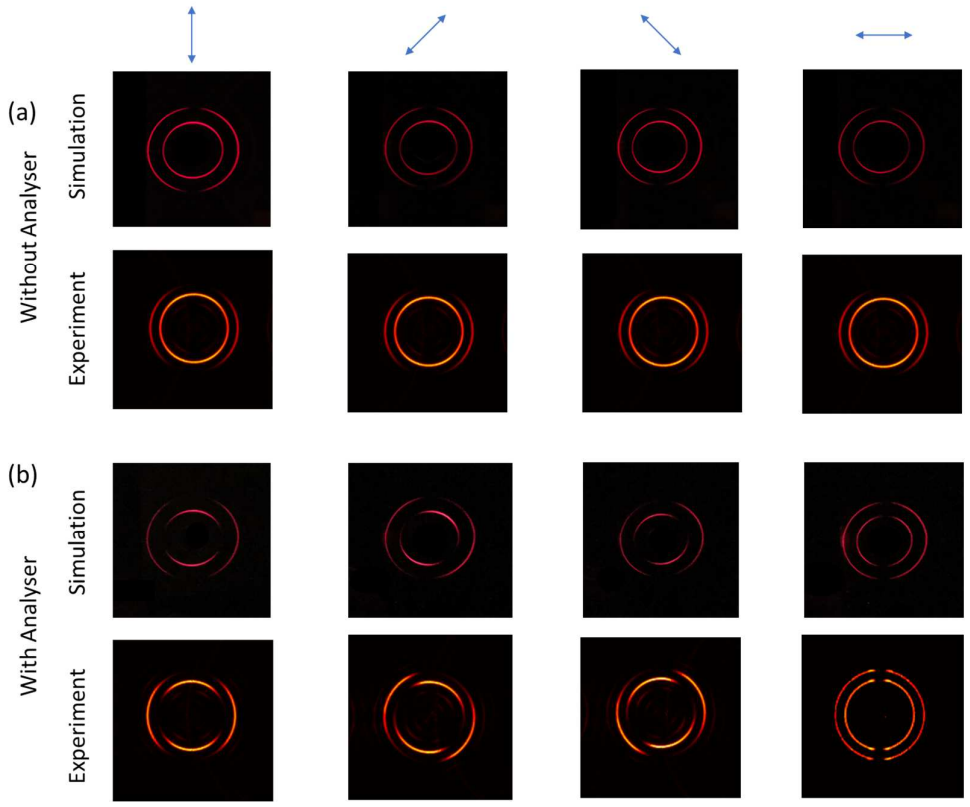

Figure 4.31 Experimental and simulation results for the measurement of the major axis of a polarization state. (a) Without an analyser. (b) With an analyser, the measured and expected major axes are marked by the blue double-headed arrows. The transmission axis of the analyser is along the horizontal direction.

Figure 4.32 shows the simulation and the experimental results for the measurement of ellipticity and handedness of the incident polarization state. Here, we focus on the detailed change on the outer ring. Although a pair of points on the two rings can work, two symmetrically distributed points can facilitate analysis. To minimize the measurement error, six symmetrically distributed points marked by A and A′, B and B′, C and C′ on the outer rings (shown in Figure 4.32a) are used to calculate the ellipticity of polarized light. The ellipticity and handedness are determined by the rise and fall of intensities on the outer ring on both sides of the screen. The intensities of the outer rings are the same for the incident LP light beam since an LP beam contains the same components of RCP and LCP. Finally, the ellipticities versus the incident polarization (a function of γ) are obtained, where γ is the angle between the transmission axis of the linear polarizer with respect to the horizontal direction. Good agreement is found between the simulation results (black solid curve) and the experimental measurements (triangles). In our approach, the spin-orbit interaction provided by the metasurface allows coupling from SAM to OAM. It provides a fast and intuitive approach to visualize the polarization state

of the incident based on the intensity difference between two split ring patterns. As we discussed above, more accurate polarization information can only be obtained based on precise measurement, calibration processes, and detailed analysis.

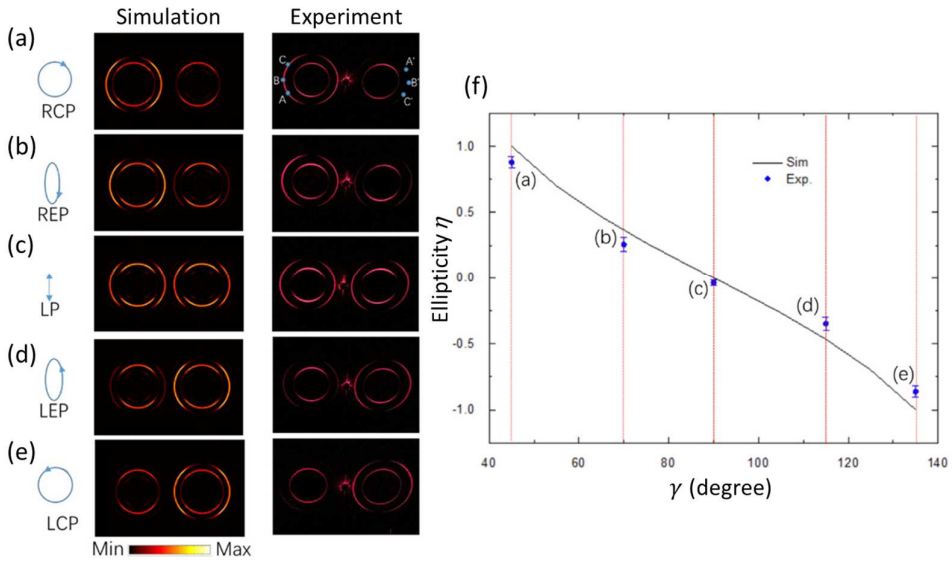

Figure 4.32 Experimentally measured and simulation results for the measurement of ellipticity and handedness of the incident polarization state. The fast axis of QWP is fixed along the vertical direction. The experimental and simulation results for the superposition of ring OAM beams upon the illumination of incident light with (a) RCP, (b) REP, (c) LP, (d) LEP, and (e) LCP, which are generated by controlling the angle between the transmission axis of the linear polarizer with respect to the horizontal direction. (f) Experimentally measured ellipticities η versus γ. γ is the angle between the transmission axis of a linear polarizer w.r.t. the horizontal direction. The solid curve and discreet triangles represent the simulation and experimental results, respectively. Six symmetrically distributed points marked by A and A′, B and B′, C and C′ on the outer rings are used to extract the field intensity. Standard deviation error bars obtained from the six points are added.

4.5. Summary

In this Chapter, we experimentally demonstrate compact metasurface devices to generate a hybrid hologram, doughnut beams, and ring OAM beams to detect polarization states of light. The polarization parameters such as major axis, ellipticity, and handedness are measured by using our developed metadevices. The subwavelength resolution and ultrathin nature make those technologies very attractive for many research fields, including polarization detection, polarization imaging, optical communications, optical tweezers, and quantum sciences.

CHAPTER 5 – POLARIZATION AND EDGE IMAGING WITH METASURFACES

The last chapter was concentrated on 1D polarization detection with the developed metadevices. In this chapter, 2D polarization detection (also called polarization imaging) is realised with optical metasurfaces by using a Fourier transform setup. Additional functionality, i.e., edge enhancement, is included to implement a homebuilt multifunctional optical microscope for polarization imaging and edge enhancement of biological samples. In this chapter, I have contributed to both simulation and experimental parts.

5.1. Background

To decrease the light scattering from different tissue structures, biological samples used for microscopy imaging are typically very thin. These tissue samples are usually transparent, leading to little contrast under a microscope without image enhancement techniques[150-152]. Distinguishing the edges of transparent biological samples precisely and enhancing the target detection and recognition performance of an imaging system are especially important [52, 153, 154]. Although chemical staining is a very popular approach, these dyes can interact with samples in a way that obscures observation, either by altering or killing the samples. Since living systems use almost exclusively L-amino acids and D-sugars, essentially, most of the biomolecules (peptides, DNA, collagens, etc) are chiral [155], meaning they are sensitive to circularly polarized light. Edge enhancement [156-158] and polarization detection [159-163] are critical to image transparent or low-contrast biological samples. However, currently available systems are limited to performing only a single functionality. In addition, imaging systems that combine multiple functionalities tend to be expensive and bulky because of the substantial footprint of their benchtop-based electronic and optical components, which reduce the portability and bring inconvenience for practical applications [164]. Moreover, such imaging systems are often custom fabricated and not commercially available. This makes them unsuitable for mass production or widespread adoption by biologists. There is a crucial need to develop portable microscopy systems that can simultaneously possess multiple functionalities.

Current edge imaging and circular polarimetric imaging suffer from technical and practical challenges. Phase-contrast microscopy works by recombining and interfering with the directly transmitted and scattered light. Unlike the typical phase contrast technique, the opposite halves of any radial line of the spiral phase element can introduce a phase difference of π between the positive and negative spatial frequencies of an incident light field, leading to a strong isotropic edge contrast enhancement of observed amplitude and phase objects. Since it only extracts important information and records basic geometric features related to the edges of an object, the spiral phase contrast imaging greatly reduces the amount of data to be processed. To date, the primary realization of spiral phase-contrast imaging is accomplished using a liquid crystal-based spatial light modulator [165-167], which suffers from large volume, limited resolution, and high cost. For example, the ultimate resolution of an edge imaging system is mainly determined by the objective lens and the spiral phase plate. Unfortunately, the resolution of the current spiral phase plate (primarily using q-plates, whose pixel size is at the micron scale) is much lower than that of the objective, degrading the performance of the imaging system. On the other hand, most biomolecules have different responses to circular polarizations with left and right-handedness due to their chiral structures. The interaction between a chiral biomolecule and polarised light can be very specific, and cause changes to the polarised light intensity and/or the phase. Thus, polarimetric imaging can not only enhance image resolution but also derive a wealth of intrinsic information about cells and tissues, e.g., morphological, biochemical, and functional properties. Without the need for sample preparation, this approach is non-destructive, enabling real-time, in situ study of biological samples. Despite the apparent information that could be obtained from circular polarisation measurements, implementation of standalone circular polarimetry microscopy in biology is very limited, mainly due to the challenging imaging procedures that involve a repeated exchange of optical components for a sequential recording of different polarisation states [168].

Optical metasurfaces are planar nanostructured interfaces and have recently attracted tremendous interest due to their unprecedented capability in the manipulation of the amplitude, phase and polarization of light at the subwavelength scale [12-14, 23, 26, 38, 39]. The emergent optical metasurface-based flat optics has revolutionized design concepts in photonics, providing a compact platform to develop unusual ultrathin optical devices with multiple functionalities [23, 85, 88]. To circumvent the abovementioned challenges, we propose to develop multifunctional microscopes based on novel ultrathin

optical devices with multiple functionalities, which are impossible with conventional optical elements. The metasurface devices are integrated with the currently available microscopy systems, which are able to simultaneously perform edge imaging, polarimetric imaging and conventional microscope imaging. Specifically, five images with different optical properties are obtained in the same imaging plane. Because the three different imaging mechanisms are integrated into the same imaging system, this does not increase the volume of the microscope due to the compactness and multifunctionality of the optical metasurface device, which is realised based on both polarization and spatial multiplexing methods. We experimentally demonstrate the capability of multifunctional microscopy with various samples. Edge imaging enables fast and reliable detection of a cell. Polarimetric imaging can obtain detailed polarization information, which can be used to resolve microstructure (such as chromatin, nuclei) and their anisotropic information (e.g., orientation, ordering). The information is complementary to that obtained via conventional microscopy imaging, allowing visualization of multiple facets of samples in real-time with subcellular resolution.

5.2. Design and Method

Figure 5.1 illustrates the concept of the multifunctional microscopy system based on metasurfaces. The imaging system is a Fourier transform setup, where the multifunctional metasurface is placed in the Fourier plane. When a light beam shines on an object, five images with different optical properties are generated in the imaging plane. Along the horizontal direction, two intensity images with different circular polarization states are symmetrically distributed with respect to the conventional microscope image in the middle, which arises from the non-converted part of light passing through the metasurface. The two intensity images with opposite circular polarizations can be used to construct a circular polarization image, which contains spatially variant circular polarization response to different handedness in a pixel. Two edge enhanced images with a dark background and different circular polarizations are symmetrically distributed along the vertical direction. The enhanced edge images can be used to distinguish the edges of the sample.

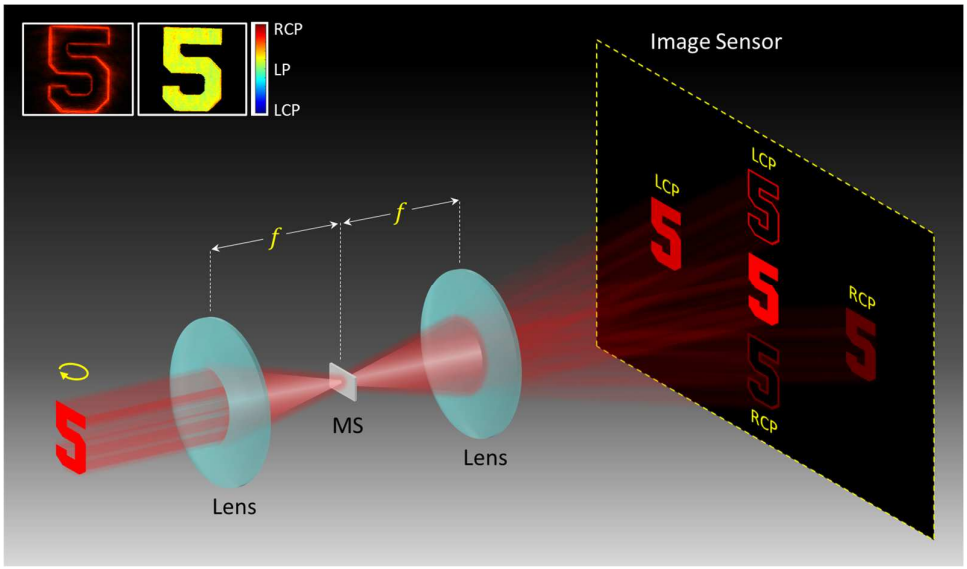

Figure 5.1 Schematic of the metasurface device for multifunctional microscopy. The imaging system is a Fourier transform setup, where the multifunctional metasurface is located in the Fourier plane. When a light beam shines on an object, five images with different optical properties are generated in the imaging plane. Along the horizontal direction, two intensity images with different circular polarizations are symmetrically distributed with respect to the normal microscope image in the middle, which arises from the non-converted part of light passing through the metasurface. The two intensity images with opposite circular polarizations are used to construct a polarization image, which contains spatially variant circular polarization responses to different handedness. Two edge enhanced images with a dark background and different circular polarizations are symmetrically distributed along the vertical direction.

The multifunctional metasurface is designed based on both polarization and spatial multiplexing methods. A phase gradient along the horizontal direction and a spiral phase along the vertical direction are combined together, which is realized with a geometric metasurface. The phase gradient can generate two images with different circular polarizations, while the spiral phase can generate two edge enhanced images with different circular polarizations along the vertical direction. Moreover, the additional phase gradient is added to the spiral phase profile to realize the off-axis design along the vertical direction. The phase distribution of the metasurface is governed by

$$\Phi(x,y) = \arg\left\{e^{i\phi_h} + e^{i(\ell\theta+\phi_v)}\right\} \tag{5.1}$$

where ϕ_h is a phase gradient along the horizontal direction that can generate an off-axis angle Θ_h w.r.t. the optical axis, ϕ_v is a phase gradient along the vertical directions that can provide the off-axis angle Θ_v w.r.t. the optical axis, θ is the azimuthal angle, and the spiral phase has a topological charge ℓ (similar to optical vortex design). The projection geometry of the metasurface is shown in Figure 5.2a. For LCP incident light, the multifunctional metasurface imprints a phase gradient (ϕ_h) along the horizontal direction and flips the handedness of the incident polarization to RCP. An RCP image is located on

the right side. On the other hand, upon the illumination of RCP incident light the metasurface imprints a phase gradient with $-\phi_h$ and again flips the handedness of the polarization to LCP, leading to an LCP image located on the left side. For linearly polarized (LP) incident light, both images appear and are symmetrically distributed with respect to the optical axis as the LP light consists of both LCP and RCP states. Similarly, two symmetrically distributed images with enhanced edges are observed along the vertical direction due to the imparted spiral phase distribution and the off-axis design $(\ell\theta + \phi_v)$. For a plasmonic metasurface consisting of gold nanorods, the majority on the transmission side is the non-converted part, which forms the conventional microscope image in the centre of the imaging plane. The multifunctional metasurface device is integrated with a conventional microscope system and its imaging performance mainly relies on the microscope, but the same imaging system has multiple functionalities, including circular polarization detection, edge enhancement, and functionality of a conventional microscope.

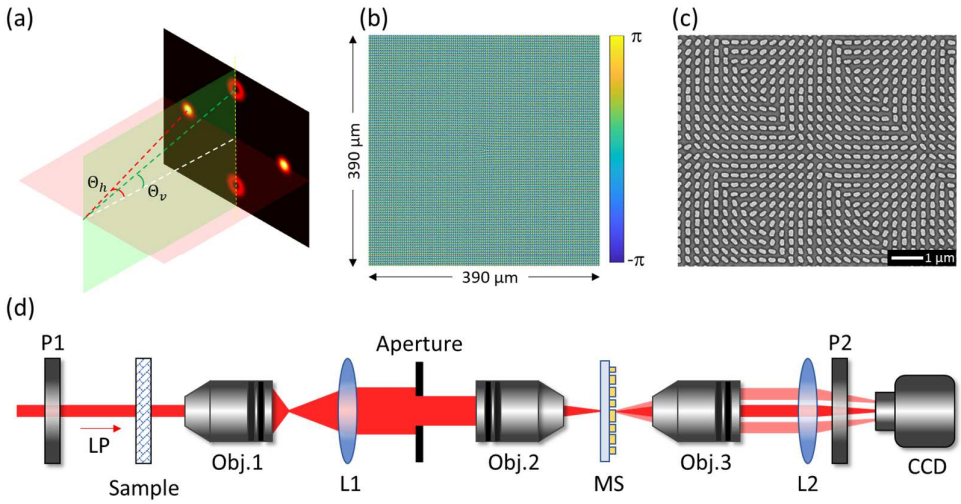

Figure 5.2 Design principle, fabricated metasurface, and experimental setup. (a) Geometric parameters of the phase gradient along the horizontal direction and the off-axis spiral phase profile (topological charge $\ell = 1$) along the vertical direction. Under the illumination of LP light at 600 nm, the half off-axis angles Θ_h and Θ_v are 9.5° and 8.2°, respectively. (b) The calculated phase profile of the designed metasurface. (c) A scanning electron microscope (SEM) image of the fabricated device. (d) The experimental diagram to perform a Fourier transform. P1 and P2: Linear polarizers, Obj.1, Obj.2, and Obj.3: 20× objective lenses (working distance 19 mm), L1 and L2: Convex lenses ($f = 75\,mm$), Aperture: Rectangular aperture (2.5×2.0 mm^2), MS: Metasurface, and CCD: Charge-coupled device.

In the design, the phase gradient ϕ_h is designed to provide the off-axis angle Θ_h of 9.5° along the horizontal direction, which is realized with a phase difference between neighbouring pixels of the sample along the horizontal direction of π/6 at the incident wavelength of 600 nm. For the edge enhancement, the topological charge ℓ is 1, and the

angle Θ_v is 8.2° corresponding to the phase difference π/7 between neighbouring pixels of the sample along the vertical direction to generate the phase gradient ϕ_v. The phase profile of the designed metasurface can be calculated based on Equation 5.1, which is shown in Figure 5.2b. The designed metadevice is realised by using transmissive metasurfaces as described in Section 2.3 and its corresponding SEM image is shown in Figure 5.2c. At this moment, the developed metadevice is ready to characterise.

The diagram of an experimental setup to characterize the fabricated metasurface is shown in Figure 5.2d. A light beam with tuneable wavelengths is generated by a supercontinuum laser source (NKT Photonics SuperK EXTREME). The laser beam is converted to an LP beam by using a linear polarizer (P1). A first objective lens (Obj.1) with a magnification of 20× and a first convex lens (L1) are used to create an image of a sample on a rectangular aperture (2.5×2.0 mm^2). A second objective lens (Obj.2) with a magnification of 20× is used to focus the images of the sample and aperture onto a Fourier plane, where the metasurface (MS) is located. A third 20× objective lens (Obj.3) and a second convex lens (L2) are employed to transform the result from the Fourier plane to an imaging plane that can be captured with a CCD camera. A second linear polarizer (P2) or analyser is used to modulate the intensity of the conventional microscopic image in the centre of the imaging plane. The operating wavelength that we use is 600 nm. The transmission axis of the polariser P1 is kept at 0° w.r.t. the *x*-axis to generate an LP light beam along the horizontal direction.

5.3. Polarization and Edge Imaging

Figure 5.3 shows the experimental results obtained with our multifunctional microscope. If the system is investigated without a sample, the developed metasurface splits the LP incident light into LCP and RCP light beams along the horizontal direction (Figure 5.3a). The circularly polarized light image on the right-hand side is converted from the incident LCP, which can be used to represent the spatial distribution of the LCP component of the sample under inspection. On the other hand, the spatial distribution of the RCP component of the sample is represented on the left-hand side in Figure 5.3a. There are the edge images of the aperture along the vertical direction, representing the edge for the RCP component of the sample and the below one for the LCP component. Due to the LP incidence, the middle image is blocked by the analyser whose transmission axis is along the vertical direction. The rectangular aperture provides a working area of 375×300 μm^2. In our experiment, a negative USAF 1951 resolution test chart is used to characterise the

functionality of the proposed optical microscope. At first, the line pairs of the group 4 element 1 on the test chart are captured as a reference position for calculating the polarization information.

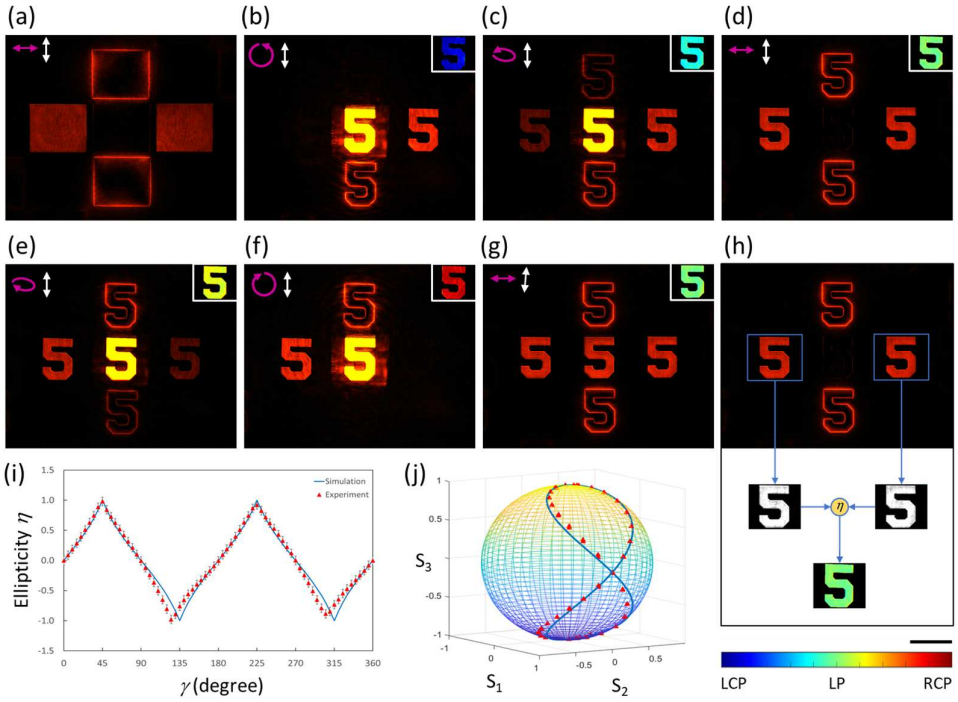

Figure 5.3 Experimental results with different polarization states of the incident light beam. (a) Captured images without a sample. Captured images of the number "5" on the negative USAF 1951 test target at different polarization states, including (b) LCP, (c) LEP, (d) LP, (e) REP, and (f) RCP. The transmission axis of the analyser is along the horizontal direction. (g) The angle between the transmission axis of the analyser and the *x*-axis is 85°. The purple arrows and white double arrows represent the polarization states of the incident light beam and the transmission axes of the analyser, respectively. (h) Captured images on the left and right sides are selected and converted to a grayscale format for calculating the ellipticity η. A black scale bar is 300 μm. A colour bar is used to represent the calculated ellipticity η shown the inset of fig. (b)-(g). (i) Experimentally measured ellipticities η of the number "5" versus γ (the angle between the transmission axis of a polarizer and the fast axis of a QWP). The solid curve and discreet triangles represent the simulation and experimental results, respectively. (j) A Poincaré sphere is used to show the experimentally measured polarization states (red triangles) of the incident light and theoretical data (blue solid curve).

In the diagram of Figure 5.2d, we place an additional QWP between P1 and a sample in order to dynamically change the LP beam to other polarization states (the details can be found in Section 2.6). The number "5" on the test target (206 μm wide and 295 μm high) is used as a sample to investigate the polarization response under different polarization states of an incident beam. The spatial intensities of the number "5" rise and fall according to the ellipticity of various incident polarized light (Figure 5.3b-5.3f), which is realized by changing the fast axis of the QWP. Initially, only the polarization image on the right and the edge at the bottom of the centre point can be observed upon the illumination of

the pure LCP (Figure 5.3b). Gradually, we can find the polarization images on both sides along the horizontal direction and the edge image on the top and at the bottom when the sample is illuminated by LEP light (Figure 5.3c). The intensity of images on the right and at the bottom is higher whilst that on the left and at the top is lower. The intensities of both sides along the horizontal and vertical directions are the same upon the illumination of the LP light since it contains an LCP light beam and an RCP light beam with equal components (Figure 5.3d). The intensity of the images on the left and the top dominates when the incident light is REP (Figure 5.3e). Finally, only the images on the left and the top appear when RCP light is incident on the sample (Figure 5.3f). Furthermore, with the incident LP beam, the intensity of the image in the middle can be tuned based on Malus' law (Figure 5.3g), and the edge of the number "5" is enhanced and clearly shown in those obtained results.

Since the intensity of the deflected images of the number "5" along the horizontal direction is closely related to the polarization states, thus both the helicity and ellipticity of those polarization states can be spatially determined by measuring the light intensities from those two CP images. As illustrated in Figure 5.3h, the captured images of the number '5' on the left and right sides are selected and converted to a grayscale format for calculating the ellipticity η The ellipticity η and helicity of the incident light can be calculated by the intensity ratio $\tau = I_{LCP}/I_{RCP}$, $\eta = \left(1-\sqrt{\tau}\right)/\left(1+\sqrt{\tau}\right)$. $\eta = \pm 1$ and $\eta = 0$ correspond to RCP (LCP) and LP, respectively [16, 117]. The ellipticities versus the incident polarization (a function of γ) are obtained, where γ is the angle of the fast axis of the QWP, while the transmission axis of the P1 is still fixed at 0° w.r.t. the *x*-axis. The calculated ellipticity η based on the experimental results in Figure 5.3b-5.3f are shown in the inset at the top right corners. The measured and simulated results of the ellipticity η within the area of the number "5" for several angles γ are given in Figure 5.3i. Furthermore, the simulated and measured polarization states of the incident light are given on a Poincaré sphere (Figure 5.3j), which shows good agreement between the simulation and the experiment. As described in Section 2.6, the polarization states can be controlled by rotating either P1 or QWP1. The error of rotated angles leads to the shifts between the simulation and experiment. These shifts are also from the misalignment of the metadevice along the vertical and horizontal directions, which has to be improved in the future.

5.4. Practical Application

By obtaining the line profiles across the line pairs from the polarization and edge images of the test target on an LCP side. We notice that the smallest line pairs that our optical system can be observed are in the group 6 element 1 of the test target with a signal-to-noise ratio of more than 20% (Figure 5.4a). This indicates that the smallest size of a specimen can be 15.6 μm. The polarization and edge images at other wavelengths from 500 nm to 700 nm are also observed as the results in Figure 5.4b-5.4e.

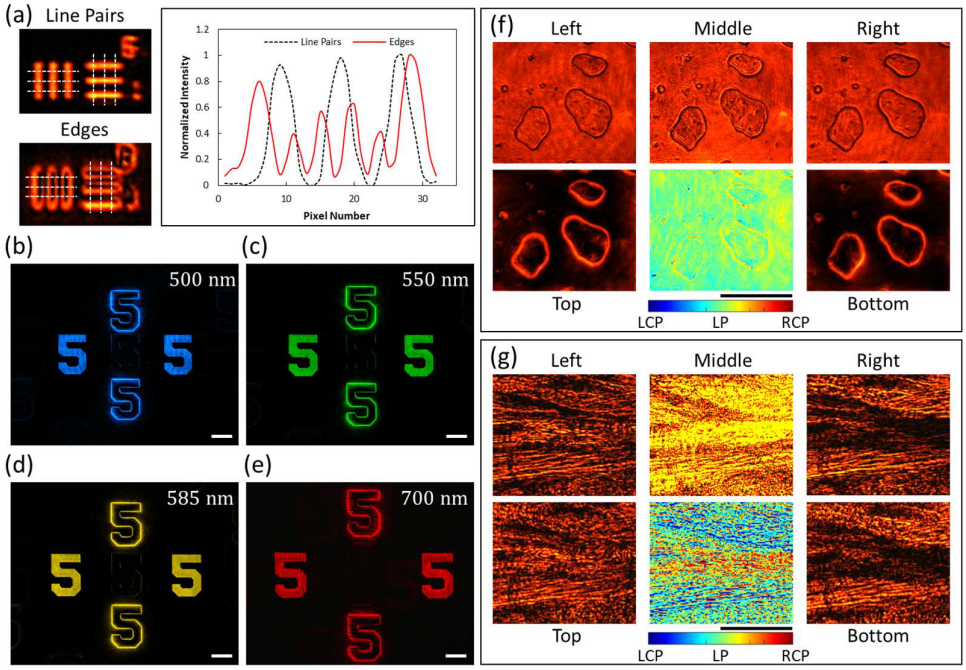

Figure 5.4 Resolution analysis, broadband performance, and imaging performance of the multifunctional microscope. (a) An LCP image and an LCP edge image of the test target on the LCP sides of the group 6 element 1. The averaged intensity profiles are along white dashed lines. The signal-to-noise ratios for line pairs and edges are more than 20%, indicating that the smallest size of a specimen is about 15.6 μm. Images obtained at the wavelengths of (b) 500 nm, (c) 550 nm, (d) 585 nm, and (e) 700 nm. (f) Polarization and edge images of cheek cells at the wavelength of 600 nm from the five positions of the captured image, and the calculated ellipticity η based on the two images with two opposite circular polarizations. Experimental results for the beef tendon at 600 nm are shown in (g), including the images from the five positions of the captured image, and the calculated ellipticity η. Scale bars are 150 μm.

The optical system is used to investigate biological samples. The first sample consists of cheek cells, which are obtained by swabbing and then put on a microscope glass slide. Five images (two LCP images, two RCP images, and one conventional microscope image) are shown in Figure 5.4f. Then, the calculated ellipticity distribution η is shown in the middle of the 2nd-row images in Figure 5.4f, which shows the dominated light polarization state is LP. Although the polarization state of light does not change much after the light passes through cheek cells, the edges of the cells are significantly enhanced.

The second sample is the beef tendon, which is the piece of connective tissue that holds muscle to bone. A thin slice of the beef tendon on a microscope glass slide is prepared. The experimental results are shown in Figure 5.4g, which clearly shows the difference between LCP and RCP images. The calculated ellipticity (ranging from -1 to 1) image is given in the middle of the 2nd-row images in Figure 5.4g, which shows that the tendon sample is very sensitive to the light's polarization due to the orientation of collagen fibres. Due to the size of the collagen fibres in the tendon is smaller than the smallest size (less than 15.6 μm) that can be recognised by the system, the edge enhancement is difficult to observe.

5.5. Large-Area Imaging

In our experiment, the field size is 375×300 μm^2. To investigate large samples, we integrate a xy scanning system with a sample holder in order to acquire multiple images of samples on the *xy*-plane by moving the samples with a motorised stage along both horizontal and vertical directions. First, the whole image of the test target is acquired with a step size of 310 μm along the horizontal direction and 250 μm along the vertical direction. There are 5×4 images in total. The area of each image (310×250 μm^2) is extracted before stitching them together, which can generate a large image. The extracted images before stitching are shown in Figure 5.5a. The images are manually stitched together, and the large image of the sample is given in Figure 5.5b. Similarly, the LCP edge images (Figure 5.5c) are also stitched together to generate a large image as shown in Figure 5.5d. Figure 5.5e and Figure 5.5f show the large LCP image and LCP edge image of cheek cells, which are obtained with 6×5 images. The polarization and edge images are created based on the multiple LCP images on the left and those on the top, respectively. The calculated ellipticity η is shown in Figure 5.5g. Experimental results for the beef tendon are given in Figures 5.5h, 5.5i, and 5.5j. Our system with a scanning approach can remarkably increase the field size of the view.

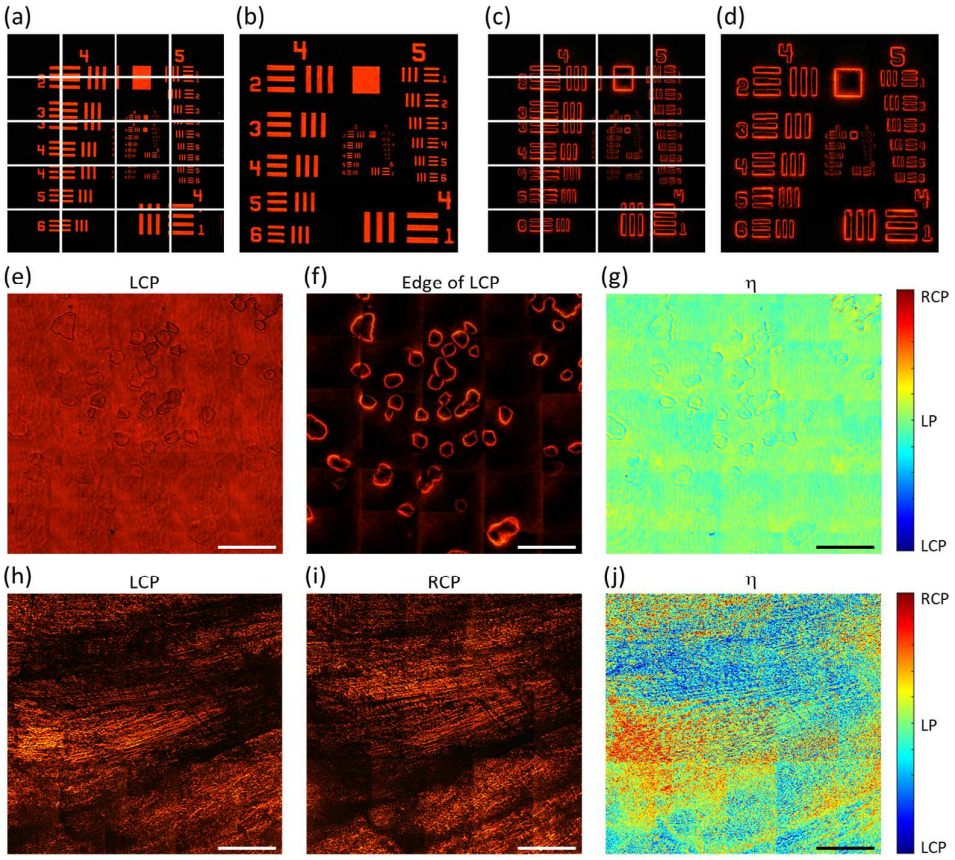

Figure 5.5 Large field size imaging with a scanning system-aided multifunctional microscope. (a) Original LCP image on the left of the imaging plane and (b) a large LCP image of the resolution target based on the stitching of multiple images. (c) Original LCP edge image and (d) a large LCP edge image of the resolution target. To investigate cheek cells, (e) a large LCP image, (f) a large LCP edge image, and (g) a calculated ellipticity η of cheek cells based on the LCP and RCP images on both sides. Experimental results for the beef tendon are given in (h), (i), and (j). Scale bars are 300 μm.

5.6. Summary

We have experimentally demonstrated a multifunctional metasurface device that can enable biologists to visualize the multiple facets of samples in real-time. To verify the design, we used a metasurface with gold nanorods with a low conversion efficiency, which can be dramatically increased by using dielectric metasurfaces [93, 94]. The working area of 375×300 μm^2 corresponds to the image dimension of 220×180 pixels. Due to the limited size of the metasurface, we use an aperture to remove the light components with high spatial frequency, leading to the low resolution of the images, which can be further improved with a large metasurface and a high-resolution camera. The quality of large-area images can be improved by using a high-precision translational stage, a smaller scanning step (less than 310 μm along x and 250 μm along y), and an image stitching algorithm or commercial image processing software.

One major advantage of this technique is that it can readily detect samples with small refractive index differences from the background environment such as biological cells. The technology enables a compact platform for structured light illumination, which has a big impact on biomedical microscopy imaging and crystal dislocation detecting. Our work can bring cutting-edge technology in metasurface and advanced microscopic technology to develop high-resolution edge imaging microscopy, which will offer a new powerful tool for biomedical imaging, diagnosis, and inspection. Unprecedented information and new discoveries are expected, which will attract broad interest from the biology and life science communities. It is our goal to make the technology compatible with common practice in a conventional biology laboratory and easy to use, and thus facilitate its uptake by biologists and life scientists.

CHAPTER 6 – CONCLUSIONS AND OUTLOOK

6.1. Conclusions

In this thesis, the geometric metasurfaces composed of gold nanorods have been utilised to develop unusual ultrathin devices for polarization generation, detection and imaging at a sub-wavelength scale. The developed metadevices have provided novel tools not only to understand the fundamental physics of metasurfaces, but also to tackle the technical challenges in practical applications that are very difficult or impossible to realise with conventional optical devices. Moreover, the ultrathin nature (subwavelength scale) and multifunctionality can meet the continuing trend of miniaturization and integration. The uniqueness of our approaches for 2D/3D polarization profile generation, polarization state detection, and multifunctional microscopy can find applications in many research fields where miniaturized systems are in high demand, including polarization sensing and imaging, optical communications, optical tweezers, quantum sciences, displays, and biomedical research. The main contribution of this thesis is summarised as follows:

1. Various new transmissive and reflective metasurface devices are designed and fabricated. The transmissive metadevices are designed based on 200×80×40-nm^3 gold nanorods sitting on ITO-coated glass substrates. The centre-to-centre distance between the nanorods is 300 nm along both x and y directions. The reflective metadevices are composed of three layers, i.e., a top layer of 200×80×30-nm^3 gold nanorods, a silicon dioxide (SiO_2) spacer layer (85 nm), and a gold ground layer (150 nm). The nanofabrication process is carried on by using the standard electron beam lithography, followed by the electron beam deposition and lift-off process. All the nanorods have the same geometry, but spatially variant orientation angles.

2. Different homebuilt experimental setups are developed to characterise the developed metadevices, which can control the polarization state of the incident light and suppress the non-converted part. A pair of a quarter-wave plate and an analyser is used to generate different polarization states of the incident light beams. By using another pair of a quarter-wave plate and an analyser, the unwanted light from the non-converted part can be suppressed. For the metadevice with the off-axis design, another pair of a quarter-wave plate and an analyser is not necessary. The objective lens is used to visualise and image onto the CCD camera for the small size of the generated patterns by the metadevices. For

the large patterns, which can be seen by the naked eyes, a screen and a digital camera are used to take a photo of the generated patterns.

3. Experimentally demonstrate the metadevices for the generation of predesigned polarization structures in 2D and 3D spaces. The 2D and 3D polarization structures are generated based on a metalens approach. A ring focal curve, an Archimedean spiral focal curve, and seven-segment-based decimal numbers are experimentally demonstrated in 2D space, while a 3-foil knot, a 4-foil knot, and a 5-foil are realized in 3D space. The geometric metasurfaces are designed based on colour and phase multiplexing and polarization rotation, creating various 3D polarization knots. Various 3D polarization knots in the same observation region can be achieved by controlling the incident wavelengths, providing unprecedented polarization control with colour information in 3D space. Furthermore, the C3 30-nm-gold meta-atoms are utilised for the generation of a nonlinear polarization profile in 2D space, which has significant potential for applications in nonlinear optical image encryption, security, and anti-counterfeiting.

4. Experimentally demonstrate the OAM superpositions with the same and different circular polarization states. The design is based on the superposition of multiple circularly polarized OAM beams with different topological charges in a single metadevice. The superpositions of four OAM beams with the same and different circular polarization states have been reported in this thesis. The research finding has opened a new avenue for engineering composite OAM beams with a minimal footprint, which has promising applications ranging from multiple optical traps to quantum science.

5. Experimentally demonstrate polarization detection using different methods, including hybrid holography, light's OAM, and optical ring vortex beams.

5.1. For the hybrid hologram, the design is the integration of an arbitrary polarization profile for image concealment and a computer-generated hybrid hologram. The hybrid hologram can simultaneously reconstruct polarization-sensitive and polarization-insensitive holographic images, while the engineered polarization profile can hide a high-resolution grayscale image. The polarization-sensitive images are used in the polarization measurement.

5.2. For light's OAM, the major axis and ellipticity of the polarized light are measured by the interference pattern of two OAM beams with the same topological charges

and opposite signs, while the handedness is determined by using topological charges with different values.

5.3. For optical ring vortex beams, the metadevice is based on the combination of the functionalities of an axicon, a vortex beam generator, and a deflector onto a single device. The polarization detection is performed with two split ring patterns. The inner ring is used to detect the major axis, while the outer ring is used to calculate the ellipticity of the incident polarization. By comparing the intensities on the outer ring on both sides of the screen, one can determine the handedness of the incident polarization.

Thus, the measured polarization parameters such as major axis, ellipticity, and handedness can be performed by using the developed metadevices. The subwavelength resolution and ultrathin nature make these technologies very attractive for many research fields, including polarization detection, polarization imaging, optical communications, optical tweezers, and quantum sciences.

6. Develop a homebuilt multifunctional optical microscope for polarization imaging and edge enhancement of biological samples. The multifunctional microscope is proposed and developed to image different objects, including biological samples such as cheek cells and beef tendons. For the same sample, five images with different optical properties are obtained on the same imaging plane, which can simultaneously perform edge imaging, polarimetric imaging, and conventional microscope imaging. Benefiting from the ultrathin nature, compactness, and multifunctionality of the optical metasurface devices, the integration does not excessively increase the volume of the optical system. With its promising capabilities and potential for expandability, we believe our microscope will herald an exciting new era in biomedical research.

6.2. Outlook

Currently, metasurfaces can operate different frequencies ranging from ultra-violet light to radio frequencies and have the unprecedented ability to modulate light's amplitude, phase, and polarisation at the sub-wavelength scale. In my opinion, the future metasurface technology will include deep-learning [169], tuneable functionalities [170], and mass production [171], which could upgrade them to be more intelligent for real-life practical applications (Figure 6.1). Especially for the tuneable functionalities, they are highly desirable for many applications, such as holographic displays, optical communication,

and tuneable imaging systems. Currently, the tuneable metasurfaces can be realised by using active materials to tune the functionalities via various mechanism, including thermo-optic effects, free-carrier effects, and phase transitions [172]. The miniaturized optical devices could be integrated into many technology platforms, such as augmented/visual reality, mobile devices, and automotive sensing.

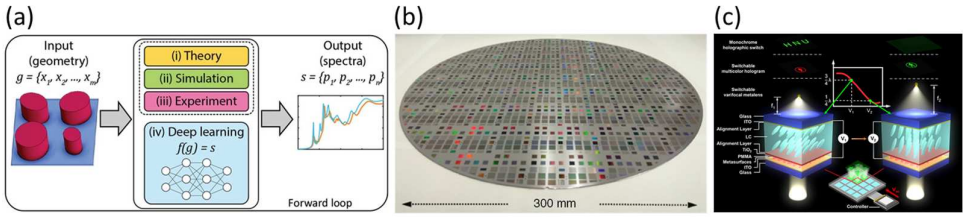

Figure 6.1 Future version of metasurfaces. (a) Deep-learning approaches [169]. (b) Large area metasurfaces and mass production [173]. (c) Tuneable metasurfaces [174].

There are several research topics that I am interested in and would like to extend with optical metasurfaces as follows.

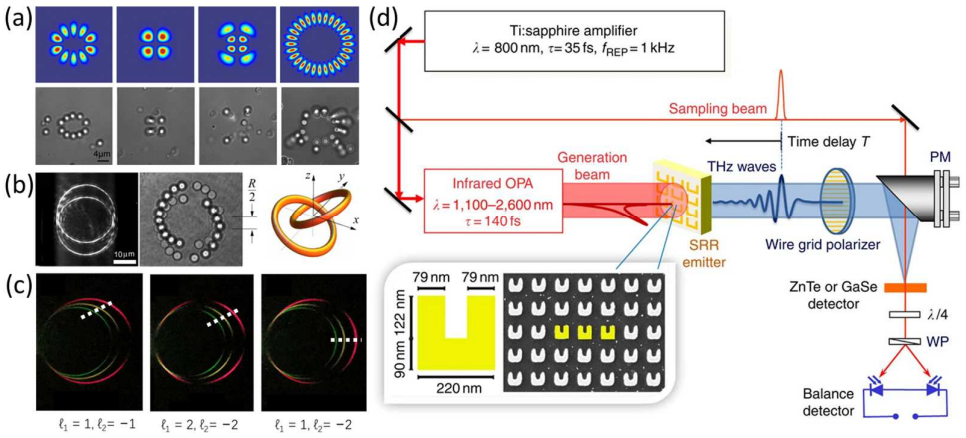

Figure 6.2 Possible applications with optical metadevices presented in this thesis. (a) 2D [175] and (b) 3D [176] particle trapping with structured light generated by spatial light modulators. (c) Spectral measurement with optical ring vortex beams [97]. (d) Generation of THz waves with split-ring resonators [177].

6.2.1. Particle Trapping

Trapping particles with a highly focused light beam has provided a new tool for new and exciting applications in the fields of biophotonics and biomedical research, such as cell interaction studies, cancer research, and cell manipulation. Apart from Gaussian beams, structured light like Bessel beams, Airy beams, and Laguerre–Gaussian beams are also suitable for trapping a particle [178, 179]. For example, the structured light in Figure 6.2a-6.2b generated by spatial light modulators have been used to manipulate particles in 2D

[175] and 3D [176] directions. This could open a new opportunity for us to experimentally demonstrate particle trapping with the structured light beams generated by our optical metasurfaces presented in Chapters 3 and 4, e.g., 2D/3D polarization structures, light's OAM, and optical ring vortex beams as well as our recently novel composite vortex beams [98].

6.2.2. Multispectral Imaging

Dozens of spectral and spatial information about an object can be simultaneously obtained with a multispectral imaging system [180]. Multispectral images provide more details about the spectral information of the object than images captured by traditional colour cameras. Traditional multispectral imagers use either spectrographs or tuneable filters as wavelength selectors when acquiring images of an object. The involvement of more optical elements (e.g., filters) causes the system very bulky, which could be tackled with the ultrathin nature of optical metasurfaces. As expressed in Equation 3.11 and the results in Figure 3.31a, the metadevice can be designed to provide the different information for ten incident wavelengths. This could be a new avenue to implement a compact multispectral imager by using an optical metasurface.

6.2.3. Multifunctional Microscope

In Chapter 5, our multifunctional microscope can split two circular polarization states of light. It is desirable to design for full polarization measurement, including linearly polarized along vertical and horizontal directions, 45° and -45° w.r.t. the x-axis, and two circularly polarized. The metasurface could be designed and fabricated by using a dielectric metasurface that can produce the propagation phase, geometric phase, or the combined phase, which is sensitive to all polarization states. Furthermore, the reflection mode is also on-demand for the investigation of opaque samples that cannot be observed in the transmission mode. Integrating with a fluorescent imaging technique and microfluidic systems could increase the potential impact and robustness of our system to investigate biological samples. Finally, a portable version is expected for scientific users with metasurface devices.

6.2.4. Spectropolarimeter

Traditional spectrometers can be used for separating and measuring the spectral components of the combined electromagnetic (EM) waves, while polarization states can be measured by using polarimeters. A spectropolarimeter is an instrument used to

simultaneously measure the spectral components and polarization states of the EM wave. This traditional measurement system has advantages in measuring speed and accuracy, but its applications are still limited due to the various polarization elements and complicated data processing systems adopted, leading to large volume and high cost. The metasurface approach is different, both polarization states and spectral components could be performed with a single metadevice. The possible method is the use of optical ring vortex beams shown in Figure 4.26 for measuring the ellipticity and handedness of the incident polarization state. Simultaneously, the spectral components can be obtained by using the intensity profile along the white dashed line across a detection plane when the incident light has more than one wavelength as shown in the white dash lines in Figure 6.2c. The ultrathin property of metadevices could be used to develop a compact and low-cost spectropolarimeter for scientific users.

6.2.5. Nonlinear Optics

Unlike X-Ray, Terahertz (THz) radiation is low non-ionising energy, which is not harmful to electronic devices, medicines, and the human body [181]. THz waves can be generated from high order harmonic generations with nonlinear metasurfaces, such as split-ring resonators (SRRs). With the exciting electric fields from 1,100-1,600 nm, the 5^{th} harmonic waves associated with the THz region have arisen by the SRRs ranging from about 0.1–4 THz [177] as illustrated in Figure 6.2d. The SRRs have been developed by using a standard nanofabrication process similar to our procedure, i.e., electron-beam lithography, gold film deposition, and lift-off process. Thus, our research could be further extended for the generation of THz signals. Furthermore, our lens-based metadevices presented in Chapter 3 can also be used to realize THz polarization manipulation, including polarization rotation, 2D and 3D predesigned polarization structures in the future. Simultaneous phase and polarization control could be used to develop vectorial THz holograms and vector vortex beams, which might open the door to develop novel and ultracompact THz devices with unusual functionalities for diverse applications.

6.2.6. Dielectric-based Metasurfaces for Higher Performance Devices

As shown in Figure 2.2, the conversion efficiency of the transmissive metasurfaces is very low, but we can use the reflective metasurfaces with a multilayer in Figure 2.7 to improve the efficiency. However, transmission mode metadevices with high efficiency for are very promising. Dielectric metasurfaces have gained conversion efficiency in the transmission mode for many optical metadevices because the designed unit cell can be

acting as a half-wave plate [14]. Furthermore, there are many choices for dielectric metasurfaces to be designed in order to produce an abrupt phase shift, including the propagation phase, PB phase, and combined phase. Thus, if we could extend our unique research topic like the generation of polarization structures with dielectric metasurfaces, it would be more interesting. For example, we could realise a 3D polarization structure with multiple colours in the same structure. This colour mixing functionalities for the same polarization structures could be realised by using a super pixel consisting of multiple dielectric nanopillars with different feature sizes (each feature size corresponding to a specific wavelength) [182]. A multifunctional microscope for full polarization imaging could be implemented with dielectric metasurfaces for more functionalities and higher performance, which can be useful for scientific users.

REFERENCES

1. W. Cai, and V. M. Shalaev, *Optical metamaterials* (Springer, 2010).

2. T. Ergin, N. Stenger, P. Brenner, J. B. Pendry, and M. Wegener, "Three-Dimensional Invisibility Cloak at Optical Wavelengths," Science **328**, 337-339 (2010).

3. D. B. Burckel, J. R. Wendt, G. A. Ten Eyck, A. R. Ellis, I. Brener, and M. B. Sinclair, "Fabrication of 3D Metamaterial Resonators Using Self-Aligned Membrane Projection Lithography," Adv Mater **22**, 3171-3175 (2010).

4. F. Ling, Z. Zhong, R. Huang, and B. Zhang, "A broadband tunable terahertz negative refractive index metamaterial," Sci Rep **8**, 9843 (2018).

5. I. M. Ehrenberg, S. E. Sarma, and B.-I. Wu, "A three-dimensional self-supporting low loss microwave lens with a negative refractive index," J Appl Phys **112**, 073114 (2012).

6. R. Melik, E. Unal, N. K. Perkgoz, C. Puttlitz, and H. V. Demir, "Metamaterial-based wireless strain sensors," Appl Phys Lett **95**, 011106 (2009).

7. O. Solgaard, *Photonic Microsystems: Micro and Nanotechnology Applied to Optical Devices and Systems* (Springer US, 2009).

8. I. Underwood, S. T. Wu, and D. Armitage, *Introduction to Microdisplays* (Wiley, 2006).

9. S.-Q. Li, X. Xu, R. M. Veetil, V. Valuckas, R. Paniagua-Domínguez, and A. I. Kuznetsov, "Phase-only transmissive spatial light modulator based on tunable dielectric metasurface," Science **364**, 1087-1090 (2019).

10. N. Yu, P. Genevet, M. A. Kats, F. Aieta, J.-P. Tetienne, F. Capasso, and Z. Gaburro, "Light Propagation with Phase Discontinuities: Generalized Laws of Reflection and Refraction," Science **334**, 333 (2011).

11. L. Huang, X. Chen, H. Mühlenbernd, G. Li, B. Bai, Q. Tan, G. Jin, T. Zentgraf, and S. Zhang, "Dispersionless Phase Discontinuities for Controlling Light Propagation," Nano Lett **12**, 5750-5755 (2012).

12. G. Zheng, H. Mühlenbernd, M. Kenney, G. Li, T. Zentgraf, and S. Zhang, "Metasurface holograms reaching 80% efficiency," Nat Nanotechnol **10**, 308-312 (2015).

13. A. Arbabi, Y. Horie, M. Bagheri, and A. Faraon, "Dielectric metasurfaces for complete control of phase and polarization with subwavelength spatial resolution and high transmission," Nat Nanotechnol **10**, 937 (2015).

14. M. Khorasaninejad, W. T. Chen, R. C. Devlin, J. Oh, A. Y. Zhu, and F. Capasso, "Metalenses at visible wavelengths: Diffraction-limited focusing and subwavelength resolution imaging," Science **352**, 1190 (2016).

15. J. P. Balthasar Mueller, N. A. Rubin, R. C. Devlin, B. Groever, and F. Capasso, "Metasurface Polarization Optics: Independent Phase Control of Arbitrary Orthogonal States of Polarization," Phys Rev Lett **118**, 113901 (2017).

16. D. Wen, F. Yue, S. Kumar, Y. Ma, M. Chen, X. Ren, P. E. Kremer, B. D. Gerardot, M. R. Taghizadeh, G. S. Buller, and X. Chen, "Metasurface for characterization of the polarization state of light," Opt Express **23**, 10272-10281 (2015).

17. M. Khorasaninejad, and K. B. Crozier, "Silicon nanofin grating as a miniature chirality-distinguishing beam-splitter," Nat Commun **5**, 5386 (2014).

18. A. Pors, M. G. Nielsen, and S. I. Bozhevolnyi, "Plasmonic metagratings for simultaneous determination of Stokes parameters," Optica **2**, 716-723 (2015).

19. P. C. Wu, J.-W. Chen, C.-W. Yin, Y.-C. Lai, T. L. Chung, C. Y. Liao, B. H. Chen, K.-W. Lee, C.-J. Chuang, C.-M. Wang, and D. P. Tsai, "Visible Metasurfaces for On-Chip Polarimetry," ACS Photonics **5**, 2568-2573 (2018).

20. Z. Li, C. Wan, C. Dai, J. Zhang, G. Zheng, and Z. Li, "Actively Switchable Beam-Steering via Hydrophilic/Hydrophobic-Selective Design of Water-Immersed Metasurface," Adv Opt Mater **9**, 2100297 (2021).

21. J. Tao, Q. You, Z. Li, M. Luo, Z. Liu, Y. Qiu, Y. Yang, Y. Zeng, Z. He, X. Xiao, G. Zheng, and S. Yu, "Mass-Manufactured Beam-Steering Metasurfaces for High-Speed

Full-Duplex Optical Wireless-Broadcasting Communications," Adv Mater **34**, 2106080 (2022).

22. F. Aieta, P. Genevet, M. A. Kats, N. Yu, R. Blanchard, Z. Gaburro, and F. Capasso, "Aberration-Free Ultrathin Flat Lenses and Axicons at Telecom Wavelengths Based on Plasmonic Metasurfaces," Nano Lett **12**, 4932-4936 (2012).

23. X. Chen, L. Huang, H. Mühlenbernd, G. Li, B. Bai, Q. Tan, G. Jin, C.-W. Qiu, S. Zhang, and T. Zentgraf, "Dual-polarity plasmonic metalens for visible light," Nat Commun **3**, 1198 (2012).

24. M. Khorasaninejad, Z. Shi, A. Y. Zhu, W. T. Chen, V. Sanjeev, A. Zaidi, and F. Capasso, "Achromatic Metalens over 60 nm Bandwidth in the Visible and Metalens with Reverse Chromatic Dispersion," Nano Lett **17**, 1819-1824 (2017).

25. S. Wang, P. C. Wu, V.-C. Su, Y.-C. Lai, C. Hung Chu, J.-W. Chen, S.-H. Lu, J. Chen, B. Xu, C.-H. Kuan, T. Li, S. Zhu, and D. P. Tsai, "Broadband achromatic optical metasurface devices," Nat Commun **8**, 187 (2017).

26. S. Wang, P. C. Wu, V.-C. Su, Y.-C. Lai, M.-K. Chen, H. Y. Kuo, B. H. Chen, Y. H. Chen, T.-T. Huang, J.-H. Wang, R.-M. Lin, C.-H. Kuan, T. Li, Z. Wang, S. Zhu, and D. P. Tsai, "A broadband achromatic metalens in the visible," Nat Nanotechnol **13**, 227-232 (2018).

27. W. T. Chen, A. Y. Zhu, V. Sanjeev, M. Khorasaninejad, Z. Shi, E. Lee, and F. Capasso, "A broadband achromatic metalens for focusing and imaging in the visible," Nat Nanotechnol **13**, 220-226 (2018).

28. M. Khorasaninejad, W. T. Chen, A. Y. Zhu, J. Oh, R. C. Devlin, D. Rousso, and F. Capasso, "Multispectral Chiral Imaging with a Metalens," Nano Lett **16**, 4595-4600 (2016).

29. M. Khorasaninejad, W. T. Chen, J. Oh, and F. Capasso, "Super-Dispersive Off-Axis Meta-Lenses for Compact High Resolution Spectroscopy," Nano Lett **16**, 3732-3737 (2016).

30. A. Y. Zhu, W.-T. Chen, M. Khorasaninejad, J. Oh, A. Zaidi, I. Mishra, R. C. Devlin, and F. Capasso, "Ultra-compact visible chiral spectrometer with meta-lenses," APL Photonics **2**, 036103 (2017).

31. Z. Yang, Z. Wang, Y. Wang, X. Feng, M. Zhao, Z. Wan, L. Zhu, J. Liu, Y. Huang, J. Xia, and M. Wegener, "Generalized Hartmann-Shack array of dielectric metalens sub-arrays for polarimetric beam profiling," Nat Commun **9**, 4607 (2018).

32. E. Arbabi, S. M. Kamali, A. Arbabi, and A. Faraon, "Full-Stokes Imaging Polarimetry Using Dielectric Metasurfaces," ACS Photonics **5**, 3132-3140 (2018).

33. G.-Y. Lee, J.-Y. Hong, S. Hwang, S. Moon, H. Kang, S. Jeon, H. Kim, J.-H. Jeong, and B. Lee, "Metasurface eyepiece for augmented reality," Nat Commun **9**, 4562 (2018).

34. Z. Li, P. Lin, Y.-W. Huang, J.-S. Park, W. T. Chen, Z. Shi, C.-W. Qiu, J.-X. Cheng, and F. Capasso, "Meta-optics achieves RGB-achromatic focusing for virtual reality," Sci Adv **7**, eabe4458 (2021).

35. H. Pahlevaninezhad, M. Khorasaninejad, Y.-W. Huang, Z. Shi, L. P. Hariri, D. C. Adams, V. Ding, A. Zhu, C.-W. Qiu, F. Capasso, and M. J. Suter, "Nano-optic endoscope for high-resolution optical coherence tomography in vivo," Nat Photonics **12**, 540-547 (2018).

36. Q. Guo, Z. Shi, Y.-W. Huang, E. Alexander, C.-W. Qiu, F. Capasso, and T. Zickler, "Compact single-shot metalens depth sensors inspired by eyes of jumping spiders," Proc Natl Acad Sci USA **116**, 22959-22965 (2019).

37. L. Huang, S. Zhang, and T. Zentgraf, "Metasurface holography: from fundamentals to applications," Nanophotonics **7**, 1169-1190 (2018).

38. L. Huang, X. Chen, H. Mühlenbernd, H. Zhang, S. Chen, B. Bai, Q. Tan, G. Jin, K.-W. Cheah, C.-W. Qiu, J. Li, T. Zentgraf, and S. Zhang, "Three-dimensional optical holography using a plasmonic metasurface," Nat Commun **4**, 2808 (2013).

39. D. Wen, F. Yue, G. Li, G. Zheng, K. Chan, S. Chen, M. Chen, K. F. Li, P. W. H. Wong, K. W. Cheah, E. Yue Bun Pun, S. Zhang, and X. Chen, "Helicity multiplexed broadband metasurface holograms," Nat Commun **6**, 8241 (2015).

40. B. Wang, F. Dong, Q.-T. Li, D. Yang, C. Sun, J. Chen, Z. Song, L. Xu, W. Chu, Y.-F. Xiao, Q. Gong, and Y. Li, "Visible-Frequency Dielectric Metasurfaces for Multiwavelength Achromatic and Highly Dispersive Holograms," Nano Lett **16**, 5235-5240 (2016).

41. Z.-L. Deng, M. Jin, X. Ye, S. Wang, T. Shi, J. Deng, N. Mao, Y. Cao, B.-O. Guan, A. Alù, G. Li, and X. Li, "Full-Color Complex-Amplitude Vectorial Holograms Based on Multi-Freedom Metasurfaces," Adv Funct Mater **30**, 1910610 (2020).

42. J. Li, P. Yu, S. Zhang, and N. Liu, "Electrically-controlled digital metasurface device for light projection displays," Nat Commun **11**, 3574 (2020).

43. I. Kim, J. Jang, G. Kim, J. Lee, T. Badloe, J. Mun, and J. Rho, "Pixelated bifunctional metasurface-driven dynamic vectorial holographic color prints for photonic security platform," Nat Commun **12**, 3614 (2021).

44. I. Kim, W.-S. Kim, K. Kim, M. A. Ansari, M. Q. Mehmood, T. Badloe, Y. Kim, J. Gwak, H. Lee, Y.-K. Kim, and J. Rho, "Holographic metasurface gas sensors for instantaneous visual alarms," Sci Adv **7**, eabe9943 (2021).

45. B. Xiong, Y. Xu, J. Wang, L. Li, L. Deng, F. Cheng, R.-W. Peng, M. Wang, and Y. Liu, "Realizing Colorful Holographic Mimicry by Metasurfaces," Adv Mater **33**, 2005864 (2021).

46. Y. Bao, L. Wen, Q. Chen, C.-W. Qiu, and B. Li, "Toward the capacity limit of 2D planar Jones matrix with a single-layer metasurface," Sci Adv **7**, eabh0365 (2021).

47. X. Guo, J. Zhong, B. Li, S. Qi, Y. Li, P. Li, D. Wen, S. Liu, B. Wei, and J. Zhao, "Full-Color Holographic Display and Encryption with Full-Polarization Degree of Freedom," Adv Mater **34**, 2103192 (2022).

48. H. Ahmed, H. Kim, Y. Zhang, Y. Intaravanne, J. Jang, J. Rho, S. Chen, and X. Chen, "Optical metasurfaces for generating and manipulating optical vortex beams," Nanophotonics (2022).

49. Y. Yang, W. Wang, P. Moitra, I. I. Kravchenko, D. P. Briggs, and J. Valentine, "Dielectric Meta-Reflectarray for Broadband Linear Polarization Conversion and Optical Vortex Generation," Nano Lett **14**, 1394-1399 (2014).

50. R. C. Devlin, A. Ambrosio, N. A. Rubin, J. P. B. Mueller, and F. Capasso, "Arbitrary spin-to-orbital angular momentum conversion of light," Science **358**, 896-901 (2017).

51. F. Yue, D. Wen, C. Zhang, B. D. Gerardot, W. Wang, S. Zhang, and X. Chen, "Multichannel Polarization-Controllable Superpositions of Orbital Angular Momentum States," Adv Mater **29**, 1603838 (2017).

52. P. Huo, C. Zhang, W. Zhu, M. Liu, S. Zhang, S. Zhang, L. Chen, H. J. Lezec, A. Agrawal, Y. Lu, and T. Xu, "Photonic Spin-Multiplexing Metasurface for Switchable Spiral Phase Contrast Imaging," Nano Lett **20**, 2791-2798 (2020).

53. H. Ren, G. Briere, X. Fang, P. Ni, R. Sawant, S. Héron, S. Chenot, S. Vézian, B. Damilano, V. Brändli, S. A. Maier, and P. Genevet, "Metasurface orbital angular momentum holography," Nat Commun **10**, 2986 (2019).

54. H. Ren, X. Fang, J. Jang, J. Bürger, J. Rho, and S. A. Maier, "Complex-amplitude metasurface-based orbital angular momentum holography in momentum space," Nat Nanotechnol **15**, 948-955 (2020).

55. F. Yue, C. Zhang, X.-F. Zang, D. Wen, B. D. Gerardot, S. Zhang, and X. Chen, "High-resolution grayscale image hidden in a laser beam," Light Sci Appl **7**, 17129-17129 (2018).

56. X. Zang, F. Dong, F. Yue, C. Zhang, L. Xu, Z. Song, M. Chen, P. Y. Chen, G. S. Buller, Y. Zhu, S. Zhuang, W. Chu, S. Zhang, and X. Chen, "Polarization Encoded Color Image Embedded in a Dielectric Metasurface," Adv Mater **30**, 1707499 (2018).

57. J. Deng, L. Deng, Z. Guan, J. Tao, G. Li, Z. Li, Z. Li, S. Yu, and G. Zheng, "Multiplexed Anticounterfeiting Meta-image Displays with Single-Sized Nanostructures," Nano Lett **20**, 1830-1838 (2020).

58. R. Zhao, X. Xiao, G. Geng, X. Li, J. Li, X. Li, Y. Wang, and L. Huang, "Polarization and Holography Recording in Real- and k-Space Based on Dielectric Metasurface," Adv Funct Mater **31**, 2100406 (2021).

59. J. Li, Y. Wang, C. Chen, R. Fu, Z. Zhou, Z. Li, G. Zheng, S. Yu, C.-W. Qiu, and S. Zhang, "From Lingering to Rift: Metasurface Decoupling for Near- and Far-Field Functionalization," Adv Mater **33**, 2007507 (2021).

60. Z.-L. Deng, Q.-A. Tu, Y. Wang, Z.-Q. Wang, T. Shi, Z. Feng, X.-C. Qiao, G. P. Wang, S. Xiao, and X. Li, "Vectorial Compound Metapixels for Arbitrary Nonorthogonal Polarization Steganography," Adv Mater **33**, 2103472 (2021).

61. G. Li, S. Chen, N. Pholchai, B. Reineke, P. W. H. Wong, Edwin Y. B. Pun, K. W. Cheah, T. Zentgraf, and S. Zhang, "Continuous control of the nonlinearity phase for harmonic generations," Nat Mater **14**, 607-612 (2015).

62. G. Li, S. Zhang, and T. Zentgraf, "Nonlinear photonic metasurfaces," Nat Rev Mater **2**, 17010 (2017).

63. M. Tymchenko, J. S. Gomez-Diaz, J. Lee, N. Nookala, M. A. Belkin, and A. Alù, "Gradient Nonlinear Pancharatnam-Berry Metasurfaces," Phys Rev Lett **115**, 207403 (2015).

64. W. Ye, F. Zeuner, X. Li, B. Reineke, S. He, C.-W. Qiu, J. Liu, Y. Wang, S. Zhang, and T. Zentgraf, "Spin and wavelength multiplexed nonlinear metasurface holography," Nat Commun **7**, 11930 (2016).

65. E. Almeida, O. Bitton, and Y. Prior, "Nonlinear metamaterials for holography," Nat Commun **7**, 12533 (2016).

66. C. Schlickriede, N. Waterman, B. Reineke, P. Georgi, G. Li, S. Zhang, and T. Zentgraf, "Imaging through Nonlinear Metalens Using Second Harmonic Generation," Adv Mater **30**, 1703843 (2018).

67. Z. Li, W. Liu, Z. Li, C. Tang, H. Cheng, J. Li, X. Chen, S. Chen, and J. Tian, "Tripling the Capacity of Optical Vortices by Nonlinear Metasurface," Laser Photonics Rev **12**, 1800164 (2018).

68. B. Reineke, B. Sain, R. Zhao, L. Carletti, B. Liu, L. Huang, C. De Angelis, and T. Zentgraf, "Silicon Metasurfaces for Third Harmonic Geometric Phase Manipulation and Multiplexed Holography," Nano Lett **19**, 6585-6591 (2019).

69. S. Pancharatnam, “Generalized theory of interference, and its applications,” P Indian Acad Sci A **44**, 247-262 (1956).

70. M. V. Berry, “The Adiabatic Phase and Pancharatnam's Phase for Polarized Light,” J Mod Optic **34**, 1401-1407 (1987).

71. D. Wen, F. Yue, W. Liu, S. Chen, and X. Chen, “Geometric Metasurfaces for Ultrathin Optical Devices,” Adv Opt Mater **6**, 1800348 (2018).

72. R. Wang, Y. Intaravanne, S. Li, J. Han, S. Chen, J. Liu, S. Zhang, L. Li, and X. Chen, “Metalens for Generating a Customized Vectorial Focal Curve,” Nano Lett **21**, 2081-2087 (2021).

73. Y. Tang, Y. Intaravanne, J. Deng, K. F. Li, X. Chen, and G. Li, “Nonlinear Vectorial Metasurface for Optical Encryption,” Phys Rev Appl **12**, 024028 (2019).

74. N. Gisin, G. Ribordy, W. Tittel, and H. Zbinden, “Quantum cryptography,” Rev Mod Phys **74**, 145-195 (2002).

75. M. Ghali, K. Ohtani, Y. Ohno, and H. Ohno, “Generation and control of polarization-entangled photons from GaAs island quantum dots by an electric field,” Nat Commun **3**, 661 (2012).

76. C. Zhang, F. Dong, Y. Intaravanne, X. Zang, L. Xu, Z. Song, G. Zheng, W. Wang, W. Chu, and X. Chen, “Multichannel Metasurfaces for Anticounterfeiting,” Phys Rev Appl **12**, 034028 (2019).

77. Y. Intaravanne, and X. Chen, “Recent advances in optical metasurfaces for polarization detection and engineered polarization profiles,” Nanophotonics **9**, 1003-1014 (2020).

78. T. Bauer, P. Banzer, E. Karimi, S. Orlov, A. Rubano, L. Marrucci, E. Santamato, R. W. Boyd, and G. Leuchs, “Observation of optical polarization Möbius strips,” Science **347**, 964 (2015).

79. R. Dorn, S. Quabis, and G. Leuchs, “Sharper Focus for a Radially Polarized Light Beam,” Phys Rev Lett **91**, 233901 (2003).

80. C. Peng, Y. Guo, T. Turiv, M. Jiang, Q.-H. Wei, and O. D. Lavrentovich, "Patterning of Lyotropic Chromonic Liquid Crystals by Photoalignment with Photonic Metamasks," Adv Mater **29**, 1606112 (2017).

81. T. Bauer, M. Neugebauer, G. Leuchs, and P. Banzer, "Optical Polarization Möbius Strips and Points of Purely Transverse Spin Density," Phys Rev Lett **117**, 013601 (2016).

82. N. Yu Kuznetsov, K. S. Grigoriev, Y. V. Vladimirova, and V. A. Makarov, "Three-dimensional structure of polarization singularities of a light field near a dielectric spherical nanoparticle," Opt Express **28**, 27293-27299 (2020).

83. H. Larocque, D. Sugic, D. Mortimer, A. J. Taylor, R. Fickler, R. W. Boyd, M. R. Dennis, and E. Karimi, "Reconstructing the topology of optical polarization knots," Nat Phys **14**, 1079-1082 (2018).

84. E. Pisanty, G. J. Machado, V. Vicuña-Hernández, A. Picón, A. Celi, J. P. Torres, and M. Lewenstein, "Knotting fractional-order knots with the polarization state of light," Nat Photonics **13**, 569-574 (2019).

85. D. Wen, S. Chen, F. Yue, K. Chan, M. Chen, M. Ardron, K. F. Li, P. W. H. Wong, K. W. Cheah, E. Y. B. Pun, G. Li, S. Zhang, and X. Chen, "Metasurface Device with Helicity-Dependent Functionality," Adv Opt Mater **4**, 321-327 (2016).

86. Z.-L. Deng, J. Deng, X. Zhuang, S. Wang, K. Li, Y. Wang, Y. Chi, X. Ye, J. Xu, G. P. Wang, R. Zhao, X. Wang, Y. Cao, X. Cheng, G. Li, and X. Li, "Diatomic Metasurface for Vectorial Holography," Nano Lett **18**, 2885-2892 (2018).

87. Z. Zhang, D. Wen, C. Zhang, M. Chen, W. Wang, S. Chen, and X. Chen, "Multifunctional Light Sword Metasurface Lens," ACS Photonics **5**, 1794-1799 (2018).

88. X. Zang, H. Ding, Y. Intaravanne, L. Chen, Y. Peng, J. Xie, Q. Ke, A. V. Balakin, A. P. Shkurinov, X. Chen, Y. Zhu, and S. Zhuang, "A Multi-Foci Metalens with Polarization-Rotated Focal Points," Laser Photonics Rev **13**, 1900182 (2019).

89. Q. Song, A. Baroni, R. Sawant, P. Ni, V. Brandli, S. Chenot, S. Vézian, B. Damilano, P. de Mierry, S. Khadir, P. Ferrand, and P. Genevet, "Ptychography retrieval

of fully polarized holograms from geometric-phase metasurfaces," Nat Commun **11**, 2651 (2020).

90. A. H. Dorrah, N. A. Rubin, A. Zaidi, M. Tamagnone, and F. Capasso, "Metasurface optics for on-demand polarization transformations along the optical path," Nat Photonics **15**, 287-296 (2021).

91. Y. Zhang, W. Liu, J. Gao, and X. Yang, "Generating Focused 3D Perfect Vortex Beams By Plasmonic Metasurfaces," Adv Opt Mater **6**, 1701228 (2018).

92. MathWorks, "Convolutional Neural Network," https://uk.mathworks.com/discovery/convolutional-neural-network-matlab.html.

93. K. Seyedeh Mahsa, A. Ehsan, A. Amir, and F. Andrei, "A review of dielectric optical metasurfaces for wavefront control," Nanophotonics **7**, 1041-1068 (2018).

94. Y. Hu, X. Wang, X. Luo, X. Ou, L. Li, Y. Chen, P. Yang, S. Wang, and H. Duan, "All-dielectric metasurfaces for polarization manipulation: principles and emerging applications," Nanophotonics **9**, 3755-3780 (2020).

95. Y. Intaravanne, J. Han, R. Wang, A. Ma, S. Li, S. Chen, and X. Chen, "Phase Manipulation-Based Polarization Profile Realization and Hybrid Holograms Using Geometric Metasurface," Adv Photonics Res **2**, 2000046 (2021).

96. A. Ma, Y. Intaravanne, J. Han, R. Wang, and X. Chen, "Polarization Detection Using Light's Orbital Angular Momentum," Adv Opt Mater **8**, 2000484 (2020).

97. J. Han, Y. Intaravanne, A. Ma, R. Wang, S. Li, Z. Li, S. Chen, J. Li, and X. Chen, "Optical Metasurfaces for Generation and Superposition of Optical Ring Vortex Beams," Laser Photonics Rev **14**, 2000146 (2020).

98. Y. Ming, Y. Intaravanne, H. Ahmed, M. Kenny, Y.-q. Lu, and X. Chen, "Creating Composite Vortex Beams with a Single Geometric Metasurface," Adv Mater **n/a**, 2109714.

99. R. A. Chipman, "Polarimetry," in *Handbook of Optics. Volume II: Devices, measurements, and properties*, M. Bass, ed. (The McGraw-Hill Companies, Inc., 1995), pp. 22.21-22.37.

100. R. M. A. Azzam, and N. M. Bashara, *Ellipsometry and polarized light* (North-Holland Pub. Co., 1997).

101. A. Kasic, M. Schubert, S. Einfeldt, D. Hommel, and T. E. Tiwald, "Free-carrier and phonon properties of n- and p-type hexagonal GaN films measured by infrared ellipsometry," Phys Rev B **62**, 7365-7377 (2000).

102. G. Vasile, E. Trouve, L. Jong-Sen, and V. Buzuloiu, "Intensity-driven adaptive-neighborhood technique for polarimetric and interferometric SAR parameters estimation," IEEE Trans Geosci Remote Sens **44**, 1609-1621 (2006).

103. X. Wang, J. Lai, and Z. Li, "Polarization studies for backscattering of RBC suspensions based on Mueller matrix decomposition," Opt Express **20**, 20771-20782 (2012).

104. A. Mistlberger, J. M. Liebmann, D. S. Greenfield, M. E. Pons, S.-T. Hoh, H. Ishikawa, and R. Ritch, "Heidelberg retina tomography and optical coherence tomography in normal, ocular-hypertensive, and glaucomatous eyes," Ophthalmology **106**, 2027-2032 (1999).

105. J. K. Gansel, M. Thiel, M. S. Rill, M. Decker, K. Bade, V. Saile, G. von Freymann, S. Linden, and M. Wegener, "Gold Helix Photonic Metamaterial as Broadband Circular Polarizer," Science **325**, 1513 (2009).

106. Y. Ye, X. Li, F. Zhuang, and S.-W. Chang, "Homogeneous circular polarizers using a bilayered chiral metamaterial," Appl Phys Lett **99**, 031111 (2011).

107. Y. Zhao, M. A. Belkin, and A. Alù, "Twisted optical metamaterials for planarized ultrathin broadband circular polarizers," Nat Commun **3**, 870 (2012).

108. M. Decker, M. Ruther, C. E. Kriegler, J. Zhou, C. M. Soukoulis, S. Linden, and M. Wegener, "Strong optical activity from twisted-cross photonic metamaterials," Opt Lett **34**, 2501-2503 (2009).

109. A. V. Rogacheva, V. A. Fedotov, A. S. Schwanecke, and N. I. Zheludev, "Giant Gyrotropy due to Electromagnetic-Field Coupling in a Bilayered Chiral Structure," Phys Rev Lett **97**, 177401 (2006).

110. X. Ni, N. K. Emani, A. V. Kildishev, A. Boltasseva, and V. M. Shalaev, "Broadband Light Bending with Plasmonic Nanoantennas," Science **335**, 427 (2012).

111. S. Sun, Q. He, S. Xiao, Q. Xu, X. Li, and L. Zhou, "Gradient-index meta-surfaces as a bridge linking propagating waves and surface waves," Nat Mater **11**, 426-431 (2012).

112. X. Chen, L. Huang, H. Mühlenbernd, G. Li, B. Bai, Q. Tan, G. Jin, C.-W. Qiu, T. Zentgraf, and S. Zhang, "Reversible Three-Dimensional Focusing of Visible Light with Ultrathin Plasmonic Flat Lens," Adv Opt Mater **1**, 517-521 (2013).

113. L. Huang, X. Chen, B. Bai, Q. Tan, G. Jin, T. Zentgraf, and S. Zhang, "Helicity dependent directional surface plasmon polariton excitation using a metasurface with interfacial phase discontinuity," Light Sci Appl **2**, e70-e70 (2013).

114. X. Chen, Y. Zhang, L. Huang, and S. Zhang, "Ultrathin Metasurface Laser Beam Shaper," Adv Opt Mater **2**, 978-982 (2014).

115. A. Shaltout, J. Liu, A. Kildishev, and V. Shalaev, "Photonic spin Hall effect in gap-plasmon metasurfaces for on-chip chiroptical spectroscopy," Optica **2**, 860-863 (2015).

116. A. Basiri, X. Chen, J. Bai, P. Amrollahi, J. Carpenter, Z. Holman, C. Wang, and Y. Yao, "Nature-inspired chiral metasurfaces for circular polarization detection and full-Stokes polarimetric measurements," Light Sci Appl **8**, 78 (2019).

117. S. Hermon, A. Ma, F. Yue, F. Kubrom, Y. Intaravanne, J. Han, Y. Ma, and X. Chen, "Metasurface hologram for polarization measurement," Opt Lett **44**, 4436-4438 (2019).

118. X. Zhang, S. Yang, W. Yue, Q. Xu, C. Tian, X. Zhang, E. Plum, S. Zhang, J. Han, and W. Zhang, "Direct polarization measurement using a multiplexed Pancharatnam-Berry metahologram," Optica **6**, 1190-1198 (2019).

119. E. Maguid, I. Yulevich, D. Veksler, V. Kleiner, M. L. Brongersma, and E. Hasman, "Photonic spin-controlled multifunctional shared-aperture antenna array," Science **352**, 1202 (2016).

120. J. P. Balthasar Mueller, K. Leosson, and F. Capasso, "Ultracompact metasurface in-line polarimeter," Optica **3**, 42-47 (2016).

121. W. T. Chen, P. Török, M. R. Foreman, C. Y. Liao, W.-Y. Tsai, P. R. Wu, and D. P. Tsai, "Integrated plasmonic metasurfaces for spectropolarimetry," Nanotechnology **27**, 224002 (2016).

122. A. Pors, and S. I. Bozhevolnyi, "Waveguide Metacouplers for In-Plane Polarimetry," Phys Rev Appl **5**, 064015 (2016).

123. F. Ding, A. Pors, Y. Chen, V. A. Zenin, and S. I. Bozhevolnyi, "Beam-Size-Invariant Spectropolarimeters Using Gap-Plasmon Metasurfaces," ACS Photonics **4**, 943-949 (2017).

124. E. Maguid, I. Yulevich, M. Yannai, V. Kleiner, M. L Brongersma, and E. Hasman, "Multifunctional interleaved geometric-phase dielectric metasurfaces," Light Sci Appl **6**, e17027-e17027 (2017).

125. S. Wei, Z. Yang, and M. Zhao, "Design of ultracompact polarimeters based on dielectric metasurfaces," Opt Lett **42**, 1580-1583 (2017).

126. K. Lee, H. Yun, S.-E. Mun, G.-Y. Lee, J. Sung, and B. Lee, "Ultracompact Broadband Plasmonic Polarimeter," Laser Photonics Rev **12**, 1700297 (2018).

127. N. A. Rubin, A. Zaidi, M. Juhl, R. P. Li, J. P. B. Mueller, R. C. Devlin, K. Leósson, and F. Capasso, "Polarization state generation and measurement with a single metasurface," Opt Express **26**, 21455-21478 (2018).

128. N. A. Rubin, G. D'Aversa, P. Chevalier, Z. Shi, W. T. Chen, and F. Capasso, "Matrix Fourier optics enables a compact full-Stokes polarization camera," Science **365**, eaax1839 (2019).

129. R. Gerehberg, and W. Saxton, "A practical algorithm for the determination of phase from image and diffraction plane pictures," Optik **35**, 237-246 (1972).

130. L. Allen, M. W. Beijersbergen, R. J. C. Spreeuw, and J. P. Woerdman, "Orbital angular momentum of light and the transformation of Laguerre-Gaussian laser modes," Phys Rev A **45**, 8185-8189 (1992).

131. P. Chen, S.-J. Ge, W. Duan, B.-Y. Wei, G.-X. Cui, W. Hu, and Y.-Q. Lu, "Digitalized Geometric Phases for Parallel Optical Spin and Orbital Angular Momentum Encoding," ACS Photonics **4**, 1333-1338 (2017).

132. T. Šmidlehner, I. Piantanida, and G. Pescitelli, "Polarization spectroscopy methods in the determination of interactions of small molecules with nucleic acids – tutorial," Beilstein J Org Chem **14**, 84-105 (2018).

133. M. Padgett, and R. Bowman, "Tweezers with a twist," Nat Photonics **5**, 343-348 (2011).

134. L. Torner, J. P. Torres, and S. Carrasco, "Digital spiral imaging," Opt Express **13**, 873-881 (2005).

135. Y. Bao, J. Ni, and C.-W. Qiu, "A Minimalist Single-Layer Metasurface for Arbitrary and Full Control of Vector Vortex Beams," Adv Mater **32**, 1905659 (2020).

136. L. Jin, Y.-W. Huang, Z. Jin, R. C. Devlin, Z. Dong, S. Mei, M. Jiang, W. T. Chen, Z. Wei, H. Liu, J. Teng, A. Danner, X. Li, S. Xiao, S. Zhang, C. Yu, J. K. W. Yang, F. Capasso, and C.-W. Qiu, "Dielectric multi-momentum meta-transformer in the visible," Nat Commun **10**, 4789 (2019).

137. K. Dholakia, N. B. Simpson, M. J. Padgett, and L. Allen, "Second-harmonic generation and the orbital angular momentum of light," Phys Rev A **54**, R3742-R3745 (1996).

138. J. Courtial, K. Dholakia, L. Allen, and M. J. Padgett, "Second-harmonic generation and the conservation of orbital angular momentum with high-order Laguerre-Gaussian modes," Phys Rev A **56**, 4193-4196 (1997).

139. A. Mair, A. Vaziri, G. Weihs, and A. Zeilinger, "Entanglement of the orbital angular momentum states of photons," Nature **412**, 313-316 (2001).

140. S. S. R. Oemrawsingh, X. Ma, D. Voigt, A. Aiello, E. R. Eliel, G. W. 't Hooft, and J. P. Woerdman, "Experimental Demonstration of Fractional Orbital Angular Momentum Entanglement of Two Photons," Phys Rev Lett **95**, 240501 (2005).

141. J. Leach, B. Jack, J. Romero, A. K. Jha, A. M. Yao, S. Franke-Arnold, D. G. Ireland, R. W. Boyd, S. M. Barnett, and M. J. Padgett, "Quantum Correlations in Optical Angle-Orbital Angular Momentum Variables," Science **329**, 662-665 (2010).

142. X. Zang, Y. Zhu, C. Mao, W. Xu, H. Ding, J. Xie, Q. Cheng, L. Chen, Y. Peng, Q. Hu, M. Gu, and S. Zhuang, "Manipulating Terahertz Plasmonic Vortex Based on Geometric and Dynamic Phase," Adv Opt Mater **7**, 1801328 (2019).

143. E. Wang, L. Shi, J. Niu, Y. Hua, H. Li, X. Zhu, C. Xie, and T. Ye, "Multichannel Spatially Nonhomogeneous Focused Vector Vortex Beams for Quantum Experiments," Adv Opt Mater **7**, 1801415 (2019).

144. Y. Liu, Y. Ke, J. Zhou, Y. Liu, H. Luo, S. Wen, and D. Fan, "Generation of perfect vortex and vector beams based on Pancharatnam-Berry phase elements," Sci Rep **7**, 44096 (2017).

145. X. Yi, Y. Liu, X. Ling, X. Zhou, Y. Ke, H. Luo, S. Wen, and D. Fan, "Hybrid-order Poincare' sphere," Phys Rev A **91**, 023801 (2015).

146. F. Yue, D. Wen, J. Xin, B. D. Gerardot, J. Li, and X. Chen, "Vector Vortex Beam Generation with a Single Plasmonic Metasurface," ACS Photonics **3**, 1558-1563 (2016).

147. C. Zhang, F. Yue, D. Wen, M. Chen, Z. Zhang, W. Wang, and X. Chen, "Multichannel Metasurface for Simultaneous Control of Holograms and Twisted Light Beams," ACS Photonics **4**, 1906-1912 (2017).

148. Y. Zhao, J. S. Edgar, G. D. M. Jeffries, D. McGloin, and D. T. Chiu, "Spin-to-Orbital Angular Momentum Conversion in a Strongly Focused Optical Beam," Phys Rev Lett **99**, 073901 (2007).

149. S. Berg-Johansen, F. Töppel, B. Stiller, P. Banzer, M. Ornigotti, E. Giacobino, G. Leuchs, A. Aiello, and C. Marquardt, "Classically entangled optical beams for high-speed kinematic sensing," Optica **2**, 864-868 (2015).

150. F. Zernike, "How I Discovered Phase Contrast," Science **121**, 345-349 (1955).

151. G. Popescu, *Quantitative Phase Imaging of Cells and Tissues* (McGraw-Hill Education, 2011).

152. Y. Park, C. Depeursinge, and G. Popescu, "Quantitative phase imaging in biomedicine," Nat Photonics **12**, 578-589 (2018).

153. F. Zernike, and F. J. M. Stratton, “Diffraction Theory of the Knife-Edge Test and its Improved Form, The Phase-Contrast Method,” Mon Not R Astron Soc **94**, 377-384 (1934).

154. G. Normanski, “Interferometry with Schlieren microscopy,” J Phys Radium **16**, 9-11 (1955).

155. J. Bailey, A. Chrysostomou, J. Hough, and T. Gledhill, “Circular polarization in star-formation regions: Implications for biomolecular homochirality,” Science **281**, 672-674 (1998).

156. A. Silva, F. Monticone, G. Castaldi, V. Galdi, A. Alù, and N. Engheta, “Performing Mathematical Operations with Metamaterials,” Science **343**, 160-163 (2014).

157. J. Zhou, H. Qian, C.-F. Chen, J. Zhao, G. Li, Q. Wu, H. Luo, S. Wen, and Z. Liu, “Optical edge detection based on high-efficiency dielectric metasurface,” Proc Natl Acad Sci USA **116**, 11137-11140 (2019).

158. T. Zhu, Y. Lou, Y. Zhou, J. Zhang, J. Huang, Y. Li, H. Luo, S. Wen, S. Zhu, Q. Gong, M. Qiu, and Z. Ruan, “Generalized Spatial Differentiation from the Spin Hall Effect of Light and Its Application in Image Processing of Edge Detection,” Phys Rev Appl **11**, 034043 (2019).

159. N. Ghosh, and A. Vitkin, “Tissue polarimetry: concepts, challenges, applications, and outlook,” J Biomed Opt **16**, 110801 (2011).

160. Y. Wang, H. He, J. Chang, N. Zeng, S. Liu, M. Li, and H. Ma, “Differentiating characteristic microstructural features of cancerous tissues using Mueller matrix microscope,” Micron **79**, 8-15 (2015).

161. W. Groner, J. W. Winkelman, A. G. Harris, C. Ince, G. J. Bouma, K. Messmer, and R. G. Nadeau, “Orthogonal polarization spectral imaging: A new method for study of the microcirculation,” Nat Med **5**, 1209-1212 (1999).

162. R. Turcotte, J. M. Mattson, J. W. Wu, Y. Zhang, and C. P. Lin, “Molecular Order of Arterial Collagen Using Circular Polarization Second-Harmonic Generation Imaging,” Biophys J **110**, 530-533 (2016).

163. W. Mickols, M. F. Maestre, and I. Tinoco, “Differential polarization microscopy of changes in structure in spermatocyte nuclei,” Nature **328**, 452-454 (1987).

164. J. Senarathna, H. Yu, C. Deng, A. L. Zou, J. B. Issa, D. H. Hadjiabadi, S. Gil, Q. Wang, B. M. Tyler, N. V. Thakor, and A. P. Pathak, “A miniature multi-contrast microscope for functional imaging in freely behaving animals,” Nat Commun **10**, 99 (2019).

165. A. Jesacher, S. Fürhapter, S. Bernet, and M. Ritsch-Marte, “Shadow Effects in Spiral Phase Contrast Microscopy,” Phys Rev Lett **94**, 233902 (2005).

166. G. Situ, G. Pedrini, and W. Osten, “Spiral phase filtering and orientation-selective edge detection/enhancement,” J Opt Soc Am A **26**, 1788-1797 (2009).

167. C. Maurer, A. Jesacher, S. Bernet, and M. Ritsch-Marte, “What spatial light modulators can do for optical microscopy,” Laser Photonics Rev **5**, 81-101 (2011).

168. A. Le Gratiet, M. Dubreuil, S. Rivet, and Y. Le Grand, “Scanning Mueller polarimetric microscopy,” Opt Lett **41**, 4336-4339 (2016).

169. O. Khatib, S. Ren, J. Malof, and W. J. Padilla, “Deep Learning the Electromagnetic Properties of Metamaterials—A Comprehensive Review,” Adv Funct Mater **31**, 2101748 (2021).

170. J. Kim, J. Seong, Y. Yang, S.-W. Moon, T. Badloe, and J. Rho, “Tunable metasurfaces towards versatile metalenses and metaholograms: a review,” Adv photonics **4**, 024001 (2022).

171. N. Li, Z. Xu, Y. Dong, T. Hu, Q. Zhong, Y. H. Fu, S. Zhu, and N. Singh, “Large-area metasurface on CMOS-compatible fabrication platform: driving flat optics from lab to fab,” Nanophotonics **9**, 3071-3087 (2020).

172. T. Cui, B. Bai, and H.-B. Sun, “Tunable Metasurfaces Based on Active Materials,” Adv Funct Mater **29**, 1806692 (2019).

173. Y. Dong, Z. Xu, N. Li, J. Tong, Y. H. Fu, Y. Zhou, T. Hu, Q. Zhong, V. Bliznetsov, S. Zhu, Q. Lin, D. H. Zhang, Y. Gu, and N. Singh, “Si metasurface half-wave plates demonstrated on a 12-inch CMOS platform,” Nanophotonics **9**, 149-157 (2020).

174. Y. Hu, X. Ou, T. Zeng, J. Lai, J. Zhang, X. Li, X. Luo, L. Li, F. Fan, and H. Duan, "Electrically Tunable Multifunctional Polarization-Dependent Metasurfaces Integrated with Liquid Crystals in the Visible Region," Nano Lett **21**, 4554-4562 (2021).

175. M. Woerdemann, C. Alpmann, and C. Denz, "Optical assembly of microparticles into highly ordered structures using Ince–Gaussian beams," Appl Phys Lett **98**, 111101 (2011).

176. E. R. Shanblatt, and D. G. Grier, "Extended and knotted optical traps in three dimensions," Opt Express **19**, 5833-5838 (2011).

177. L. Luo, I. Chatzakis, J. Wang, F. B. P. Niesler, M. Wegener, T. Koschny, and C. M. Soukoulis, "Broadband terahertz generation from metamaterials," Nat Commun **5**, 3055 (2014).

178. K. Dholakia, and T. Čižmár, "Shaping the future of manipulation," Nat Photonics **5**, 335-342 (2011).

179. Y. Yang, Y. Ren, M. Chen, Y. Arita, and C. Rosales-Guzmán, "Optical trapping with structured light: a review," Adv photonics **3**, 034001 (2021).

180. G. ElMasry, and D.-W. Sun, "CHAPTER 1 - Principles of Hyperspectral Imaging Technology," in *Hyperspectral Imaging for Food Quality Analysis and Control*, D.-W. Sun, ed. (Academic Press, 2010), pp. 3-43.

181. K. Ahi, and M. Anwar, *Advanced terahertz techniques for quality control and counterfeit detection* (SPIE, 2016).

182. Y. Bao, Y. Yu, H. Xu, C. Guo, J. Li, S. Sun, Z.-K. Zhou, C.-W. Qiu, and X.-H. Wang, "Full-colour nanoprint-hologram synchronous metasurface with arbitrary hue-saturation-brightness control," Light Sci Appl **8**, 95 (2019).